

Optical manipulation of plasmonic nanoparticles: Applications in surface chemistry and nano-optics

Présentée le 24 février 2023

Faculté des sciences et techniques de l'ingénieur
Laboratoire de nanophotonique et métrologie
Programme doctoral en photonique

pour l'obtention du grade de Docteur ès Sciences

par

Jeonghyeon KIM

Acceptée sur proposition du jury

Prof. Y. Bellouard, président du jury
Prof. O. Martin, directeur de thèse
Prof. Q.-H. Park, rapporteur
Prof. V. Sandoghdar, rapporteur
Prof. G. Tagliabue, rapporteuse

Acknowledgements

It was my curiosity to discover a new world that made me leave Korea and move to Switzerland. In the six years I have been here in Lausanne, I have grown a lot intellectually and mentally and also been surrounded by wonderful people. Simply put, this thesis would not have been possible without their help.

First and foremost, I want to thank Olivier for welcoming me to the NAM team and supervising me for the past six years. He was the navigator of my thesis, keeping me on track for this long journey. Discussions with him always shed light on the way I needed to take.

I would also like to thank Profs. Q-han Park, Vahid Sandoghdar, and Giulia Tagliabue for taking the time to read my thesis and Prof. Yves Bellouard for serving as president of my defense. During my thesis examination, they all thoroughly evaluated my work and were deeply engaged in the discussion. I am especially grateful to Prof. Q-han Park for his guidance on Chapter 5 and discussions on Chapter 6.

Toralf and Christian, the senior scientists in our laboratory, deserve my gratitude. Toralf was the most helpful in constructing the optical setup for this thesis. He taught me a lot about the practical aspects of designing and building an optical system. Christian, my officemate and coffee buddy, not only provided me with deep insights into the solutions to the problems I encountered in this thesis, but our numerous conversations also soothed and motivated me.

I would also like to thank all of the past and present members of our amazing NAM team. All of our interactions inside and outside of the lab nourished my studies. Being a part of such an interdisciplinary and international group has broadened my horizons. Debdatta, Marco, Siarhei, Mintae, and Hsiang-chu, in particular; you were the people with whom I spent the majority of my time in the lab, looked for when I had problems, and shared concerns. Special thanks to Karim for developing the SIE user interface tool, which I greatly enjoyed. Thank you, Cathy, Beatrice, and David for your essential assistance in the administration and technical support.

Apart from my studies, my time in Switzerland was full of beautiful memories with dear friends. All of my dearest friends I met in Switzerland, including Dong Cheon and Min Kyeong, Wonjong and Sol, Songi, Seongmin and Minkyung, Oh-hyeon, Jisoo, and Jihyun, Dan and Claudia, Pengbo, are truly priceless. My long and precious Korean relationships, including Jihyeon and Josh, Jihye, Yura, and Miso, also provided great support. I had a lovely time

Acknowledgements

playing golf thanks to Jean-Sebastian and Majda, and it helped me forget about the stress of my studies.

Lastly, I want to express my gratitude to my family. The trust and support from my families in Korea were invaluable. Semin, my life partner, always gave me unconditional support and intellectual inspiration. I cannot imagine my life without you, hence this thesis.

Lausanne, 13 January 2023

Jenna

Abstract

Optical tweezers are devices that can manipulate nano- and microparticles using a laser. The principle of optical tweezers is to apply a force to an object using the momentum of light. This force is very small, but it is sufficient to move things in the microscopic world. Consequently, optical tweezers can grab, move, and even assemble objects on a much smaller scale, just like human hands.

Optical tweezers have revolutionized the way scientists experiment with small particles in many fields of science, and their utility as a tool for understanding nanoscale processes is continuously expanding. In this dissertation, we discuss the new application possibilities of optical tweezers in two distinct disciplines: surface sciences and nano-optics.

We first employ optical tweezers in surface science by trapping gold nanoparticles at an interface and observing their motion. Due to their strong scattering and absorption, gold nanoparticles are a superb optical probe and a nanoscale heater that can be remotely controlled by light. They can provide heat to the molecules adsorbing on the surrounding surfaces and stimulate further interactions. We compare these findings to those obtained using non-thermal dielectric probes and find that heat-induced effects are indeed present in our experiments. This study demonstrates that gold nanoparticles are highly effective probes that can apply heat locally and examine the resulting interaction in real time. Thermal phenomena exist in many scientific disciplines; hence, the optically trapped gold nanoparticles can serve as a valuable tool for investigating these phenomena at the nanoscale.

We then assemble gold nanoparticles into a complex structure using optical tweezers. Individually, gold nanoparticles possess exceptional optical properties. However, when two or more of them are arranged adjacently, their properties become even more intriguing due to the strong interaction of the near fields, which is one of the most vital areas of nano-optics. Optical tweezers offer a unique method for organizing these particles in a controlled manner, producing a strong near-field coupling. We examine this coupling behavior by numerically simulating and experimentally realizing optical assemblies. This concept of tweezer-organized assemblies can create exciting opportunities for constructing three-dimensional nanoscale architectures beyond the current technologies that have evolved from conventional semiconductor device fabrication processes. Moreover, optical tweezers enable the flexible combination of structures derived from distinct methods, such as colloidal particles and lithographically defined nanostructures.

Keywords: Optical tweezers, gold nanoparticles, nano-optics, plasmonics, surface chemistry, colloids, optical force, laser, radiation pressure, coupled oscillators, near-field coupling, absorption, scattering, optical heating, surfactants, single-particle tracking, self-assembly, mean squared displacement, electrostatic interaction, hydrophobic interaction.

Résumé

Les pincettes optiques permettent de manipuler des objets de dimensions nano- et microscopiques avec un laser, en appliquant une force par le transfert de la quantité de mouvement de la lumière. Bien que cette force soit très petite, elle est suffisante pour bouger des objets dans le microcosme. Ainsi, une pincette optique peut attraper, déplacer et même assembler des objets à l'échelle microscopique, comme le fait la main humaine dans le monde macroscopique.

Les pincettes optiques ont révolutionné la façon d'expérimenter avec de petites particules dans différents domaines de la science et leur utilité pour comprendre des phénomènes nanoscopiques ne cesse de croître. Dans cette thèse, nous en décrivons des applications innovantes dans deux disciplines : la science des surfaces et la nano-optique.

En science des surfaces, nous commençons par piéger des nanoparticules d'or à une interface et observons leurs trajectoires. Grâce à une forte absorption et diffusion de la lumière, ces nanoparticules d'or se révèlent d'excellentes sondes optiques et des sources de chaleur nanoscopiques qui peuvent être contrôlées à distance. Elles permettent de chauffer localement les molécules adsorbées sur les surfaces environnantes et de stimuler d'autres interactions physico-chimiques. En comparant ces résultats avec ceux obtenus avec des sondes diélectriques pour lesquelles les effets thermiques sont négligeables, nous mettons en évidence des effets induits par la chaleur dans nos expériences avec des nanoparticules d'or. Ces expériences ont aussi démontré que les nanoparticules d'or sont des sondes particulièrement efficaces qui peuvent chauffer localement et dont il est possible de contrôler l'interaction avec l'environnement en temps réel. Comme les phénomènes thermiques existent dans de nombreuses disciplines scientifiques, les nanoparticules d'or piégées par la lumière étudiées dans cette thèse, ont certainement un très grand potentiel pour étudier ces phénomènes à l'échelle nanoscopique.

Nous avons aussi utilisé des pincettes optiques pour assembler des nanoparticules d'or afin de former des structures plus complexes. Alors qu'individuellement une nanoparticule d'or possède déjà d'intéressantes propriétés optiques, ces propriétés sont décuplées lorsque plusieurs particules sont combinées en une structure plus large. Ainsi, les pincettes optiques offrent une méthode unique pour organiser de la matière en utilisant l'exaltation du champ proche optique produit par chaque particule. Nous avons étudié ce couplage optique à l'aide de simulations numériques et d'expériences réalisées avec des ensembles de nanoparticules. L'idée d'assembler et d'organiser des nanostructures à l'aide de la lumière ouvre des perspec-

tives totalement nouvelles pour construire des architectures tri-dimensionnelles à l'échelle nanométrique. Ces perspectives vont au-delà des nanotechnologies conventionnelles issues de la fabrication des semiconducteurs. Qui plus est, les pincettes optiques permettent aussi de combiner ensemble des éléments qui ont été fabriqués par différentes méthodes, comme la lithographie colloïdale ou la lithographie par faisceau d'électrons.

Mots-clés : Pincette optique, nanoparticules d'or, nano-optique, plasmonique, chimie des surfaces, colloïdes, forces optique, laser, pression de radiation, oscillateurs couplés, champ proche optique, absorption et diffusion de la lumière, effets thermiques, surfactants, poursuite d'une particule unique, auto-assemblage, déplacement, interaction électrostatique, interaction hydrophobique.

Contents

| | |
|--|------------|
| Acknowledgements | i |
| Abstract (English/Français) | iii |
| List of figures | xi |
| List of tables | xv |
| 1 Introduction | 1 |
| 1.1 Optical manipulation | 5 |
| 1.2 Plasmonic nanoparticles | 6 |
| 1.3 Thesis objectives and organization | 8 |
| 2 Experimental and numerical methods | 11 |
| 2.1 Overview | 11 |
| 2.2 Experimental methods | 12 |
| 2.2.1 Sample preparation | 12 |
| 2.2.2 Trapping setup | 12 |
| 2.2.3 Imaging setup | 13 |
| 2.2.4 Characterization of colloidal properties | 14 |
| 2.3 Nanofabrication | 17 |
| 2.4 Numerical simulation | 19 |
| 2.4.1 Surface integral equation (SIE) method | 19 |
| 2.5 Optical heating simulation using COMSOL | 26 |
| 3 The role of interfacial layers in trapped particle motion | 29 |
| 3.1 Introduction | 29 |
| 3.2 Materials and methods | 30 |
| 3.3 Results and discussion | 31 |
| 3.3.1 Mean squared displacement (MSD) | 31 |
| 3.3.2 Statistical distribution of MSD | 33 |
| 3.3.3 Surfactant adsorption | 35 |
| 3.3.4 Effect of adsorbed surfactants at different concentration ranges | 37 |
| 3.3.5 Comparison with non-thermal probes | 42 |
| 3.4 Conclusion | 45 |
| | vii |

| | | |
|----------|--|------------|
| 4 | Probing molecular interactions with trapped nanoparticle motion analysis | 47 |
| 4.1 | Introduction | 47 |
| 4.2 | Materials and methods | 48 |
| 4.2.1 | Materials and experiments | 48 |
| 4.2.2 | Preparation of glass surface | 48 |
| 4.3 | Results and discussion | 49 |
| 4.3.1 | Surfactant adsorption at water–glass interface | 49 |
| 4.3.2 | Time-varying trajectory in an optical trap | 52 |
| 4.3.3 | Surfactant bilayers on particle surfaces | 56 |
| 4.3.4 | Effects of bilayer coverages on long-term interactions | 56 |
| 4.3.5 | MSD analysis of a time-varying trajectory | 59 |
| 4.4 | Conclusion | 62 |
| 5 | Optical forces on a plasmonic particle in a plasmonic trap | 63 |
| 5.1 | Introduction | 63 |
| 5.2 | Results and discussion | 64 |
| 5.2.1 | Plasmonic dipole antenna | 64 |
| 5.2.2 | Methods for calculating optical forces | 65 |
| 5.2.3 | Comparison between Maxwell’s stress tensor (MST) and dipole approximation (DA) methods | 67 |
| 5.2.4 | Wavelength and particle size dependence of the optical force | 70 |
| 5.3 | Conclusion | 77 |
| 6 | Plasmonic assemblies realized by optical manipulation | 79 |
| 6.1 | Introduction | 79 |
| 6.2 | Materials and methods | 81 |
| 6.2.1 | Gold colloids | 81 |
| 6.2.2 | Fabrication of nanoantennas | 81 |
| 6.2.3 | Trapping experiments | 82 |
| 6.2.4 | Spectral measurements | 82 |
| 6.3 | Results and discussion | 82 |
| 6.3.1 | Trapping nanoparticles within a nanoflower | 82 |
| 6.3.2 | Experimental results | 89 |
| 6.3.3 | Coupled oscillator model | 93 |
| 6.3.4 | Analysis of experimental results using the coupled oscillator model | 113 |
| 6.3.5 | Possible mechanisms for particle immobilization | 119 |
| 6.4 | Conclusion | 120 |
| 7 | Conclusions and outlook | 123 |
| 7.1 | Summary | 123 |
| 7.2 | Limitations | 124 |
| 7.3 | Future research | 126 |

CONTENTS

| | |
|---|------------|
| A Interaction force between admicelles and trapped particles | 129 |
| Bibliography | 148 |
| Curriculum Vitae | 149 |

List of Figures

| | | |
|------|--|----|
| 1.1 | A work from T. Newman to meet a longstanding challenge from Richard Feynman. | 2 |
| 1.2 | Tweezer-assembled nanostructures. | 4 |
| 1.3 | A schematic illustration of an optical tweezer. | 5 |
| 1.4 | Near-field amplitude enhancements of a single nanorod and dipole nanoantennas. | 7 |
| 2.1 | Overview of the optical set-up | 13 |
| 2.2 | Zeta potential for a particle in a dispersion medium. | 15 |
| 2.3 | Effect of colloid concentration on zeta potential. | 16 |
| 2.4 | Example plasmonic nanoantennas fabricated by e-beam lithography process. | 19 |
| 2.5 | Simulation mesh examples. | 20 |
| 2.6 | Points on a sphere for evaluating far-field electric and magnetic fields. | 22 |
| 2.7 | Polarization charge distribution of a gold sphere as an example. | 25 |
| 2.8 | Example geometry and mesh for optical heating simulation. | 27 |
| 2.9 | Fluid flow caused by natural convection. | 27 |
| 2.10 | Temperature distribution around the particle. | 28 |
| 3.1 | Locating a particle from an optical image. | 31 |
| 3.2 | Absorbance spectra for 150 nm gold colloids and 210 nm polystyrene (PS) beads. | 32 |
| 3.3 | Particle trajectory in an optical trap and its mean squared displacement (MSD). | 33 |
| 3.4 | Statistical distribution of MSDs for different surfactant concentrations. | 34 |
| 3.5 | Sizes distribution for gold and PS colloids and Mie absorption cross-section for gold nanoparticles. | 34 |
| 3.6 | Critical micelle concentration (CMC) and colloid characteristics (hydrodynamic size and zeta potential). | 36 |
| 3.7 | Cross-sectional temperature distribution around the particle. | 38 |
| 3.8 | Hydrodynamic drags estimated from MSD data fitting. | 38 |
| 3.9 | Interaction force between a gold nanoparticle and an admicelle based on the DLVO theory. | 40 |
| 3.10 | Cartoon showing plausible morphologies of adsorbed surfactant cations at the interfaces. | 42 |
| 3.11 | Polystyrene (PS) beads as a non-thermal probe. | 44 |
| 4.1 | Schematic diagram showing probable morphologies of adsorbed surfactant molecules on bare and activated glass surfaces. | 50 |

| | | |
|------|---|-----|
| 4.2 | Contact angles on activated glass surfaces. | 51 |
| 4.3 | Time-varying motion of particles in harmonic optical traps. | 53 |
| 4.4 | Four more example trajectories showing different patterns. | 54 |
| 4.5 | Effects of surfactant morphologies on particle motion as a function of concentration. | 57 |
| 4.6 | Time-averaged mean squared displacement (MSD) of segmented trajectories. . | 61 |
| 5.1 | Gold dipole antenna design and response. | 65 |
| 5.2 | Optical force vectors for a 20 nm gold nanoparticle as a function of its position along the x -axis. | 68 |
| 5.3 | Force as a function of wavelength or particle's z position | 69 |
| 5.4 | Optical forces acting on particles with different sizes. | 69 |
| 5.5 | Size and wavelength dependence of the optical force using the MST approach. . | 71 |
| 5.6 | The relation between resonance spectra and optical force for the coupled particle-trap system. | 72 |
| 5.7 | Near-field distributions and surface polarization charges. | 75 |
| 5.8 | Origin of the repulsive force. | 76 |
| 6.1 | Introduction to nanoflower trapping. | 80 |
| 6.2 | Computed optical force along the z -axis while varying the particle's height or its diameter. | 83 |
| 6.3 | Polarization charges on the surfaces of the coupled system (100 nm and 140 nm in diameter) while changing the particle-flower distance. | 84 |
| 6.4 | Polarization charges on the nanoflower surfaces without a particle. | 85 |
| 6.5 | Near-field intensity distributions for the two particles while changing their vertical location along the z -axis. | 86 |
| 6.6 | Optical force exerted on a 100 nm nanoparticle located 5 nm above the nanoflower. . | 87 |
| 6.7 | Optical force exerted on a 140 nm nanoparticle located 5 nm above the nanoflower. . | 88 |
| 6.8 | Three nanoflower configurations with increasing pocket sizes. | 90 |
| 6.9 | Three example spectra from individual nanoflowers with the F2 design. | 90 |
| 6.10 | Example spectrum with no spectral splitting after particle trapping. | 91 |
| 6.11 | Spectral variation of the coupled system while increasing the particle size. . . . | 92 |
| 6.12 | Three exemplary spectra from individual nanoflowers with the F3 design. . . . | 92 |
| 6.13 | Single particle response modeled with a forced harmonic oscillator with damping. . | 95 |
| 6.14 | Fano interference in optical systems. | 96 |
| 6.15 | Nanoflower response modeled with two coupled oscillators. | 97 |
| 6.16 | Polarization charge distributions far from and in the middle of the Fano resonance. . | 100 |
| 6.17 | Two-coupled oscillator model fitted to the nanoflower spectral measurements. . . | 101 |
| 6.18 | Coupled oscillator model for nanoflower-nanoparticle coupled system. | 103 |
| 6.19 | Simulation fitting while changing the particle's height. | 105 |
| 6.20 | Fitting parameter values as a function of the particle height. | 106 |
| 6.21 | Examples of polarization charge distributions at five different wavelengths. . . | 107 |
| 6.22 | Phase difference between horizontal and diagonal petals with varying z_{offset} . . | 110 |

LIST OF FIGURES

| | |
|---|-----|
| 6.23 Simulation fitting while changing the particle's diameter. | 111 |
| 6.24 Spectral responses of a particle with a varying diameter and parameters for the single oscillator model to represent these responses | 111 |
| 6.25 Fitting parameter values as a function of the particle diameter | 113 |
| 6.26 Estimated parameters based on realistically limited data for varying z_{offset} | 115 |
| 6.27 Comparison of simulation responses, previous comprehensive fitting, and fitting with only the total response when $z_{\text{offset}} = 0$ | 116 |
| 6.28 Estimated parameters based on limited data for varying particle diameters. . . | 117 |
| 6.29 Three-coupled oscillator model applied to measured spectra. | 118 |
| 6.30 Temperature distribution around the nanoflower with a 100 nm trapped particle. | 120 |
| 7.1 Scanning electron microscope images of nanostructures defined by electron- beam lithography and lift-off process. | 126 |

List of Tables

| | | |
|-----|---|-----|
| 2.1 | Process flow for nanoantenna fabrication using e-beam lithography. | 18 |
| 6.1 | Constraints and settings used in nanoflower simulation fitting. | 99 |
| 6.2 | Constraints and settings used in nanoflower measurement fitting. | 102 |
| 6.3 | Fitting constraints for coupled system (varying the particle's z_{offset}). | 108 |
| 6.4 | Fitting constraints for coupled system (varying particle diameter). | 112 |
| 6.5 | Fitting constraints and settings for measured data. | 114 |
| A.1 | Measured electrophoretic mobility and double layer potential | 131 |

1 Introduction

“There’s Plenty of Room at the Bottom.”

— Richard Feynman’s 1959 lecture

Sixty-three years ago, Richard Feynman gave a lecture with the title above [1]. He talked about the prospect of manipulating and controlling objects on the atomic scale. And many of the things he imagined in this talk became a reality. In particular, he proposed two challenges at the end of his lecture, one of which was to build a tiny ($1/64$ -inch cubed) rotating motor, which, to Feynman’s surprise, was claimed in the next year (but perhaps not that surprising to Swiss watchmakers). The other was to reduce one page of a book by $1/25,000$ times in such a manner that an electron microscope can read it. This second challenge was accomplished 26 years later, in 1985, by a graduate student using electron-beam lithography (Figure 1.1).

Science and technology have advanced, and we are now living in a world of nanotechnology. Nanotechnology is a broad concept that encompasses sciences, engineering, and technologies carried out at the nanoscale, which corresponds to between 1 and 100 nanometers. It is commonly stated that the age of nanotechnology was not born until the early 1980s, when the scanning tunneling microscope (STM) made it possible to routinely image and manipulate individual atoms and their bonds [3–5]. The development of STM earned its inventors the Nobel Prize in Physics in 1986, and after a few years, manipulation of individual atoms and molecules was successfully demonstrated [6–8] just as Feynman had foreseen.

During this infancy of nanotechnology, a completely new way of manipulating matter was also invented. Arthur Ashkin at Bell Laboratories was interested in how the momentum of photons could be used to move matter and published his first paper on radiation pressure and optical trapping in 1970 [9]. This paper was cited as one of the foremost in atomic physics over the past century [10]. Later, in 1986, he succeeded in trapping dielectric particles of various sizes, from tens of nanometers to a few microns, using the famous single-beam optical trap [11]. His colleague, Steven Chu, also succeeded in trapping atoms using a laser light [12], which earned him the 1997 physics Nobel Prize. (Interestingly, in 2018, while this thesis was being

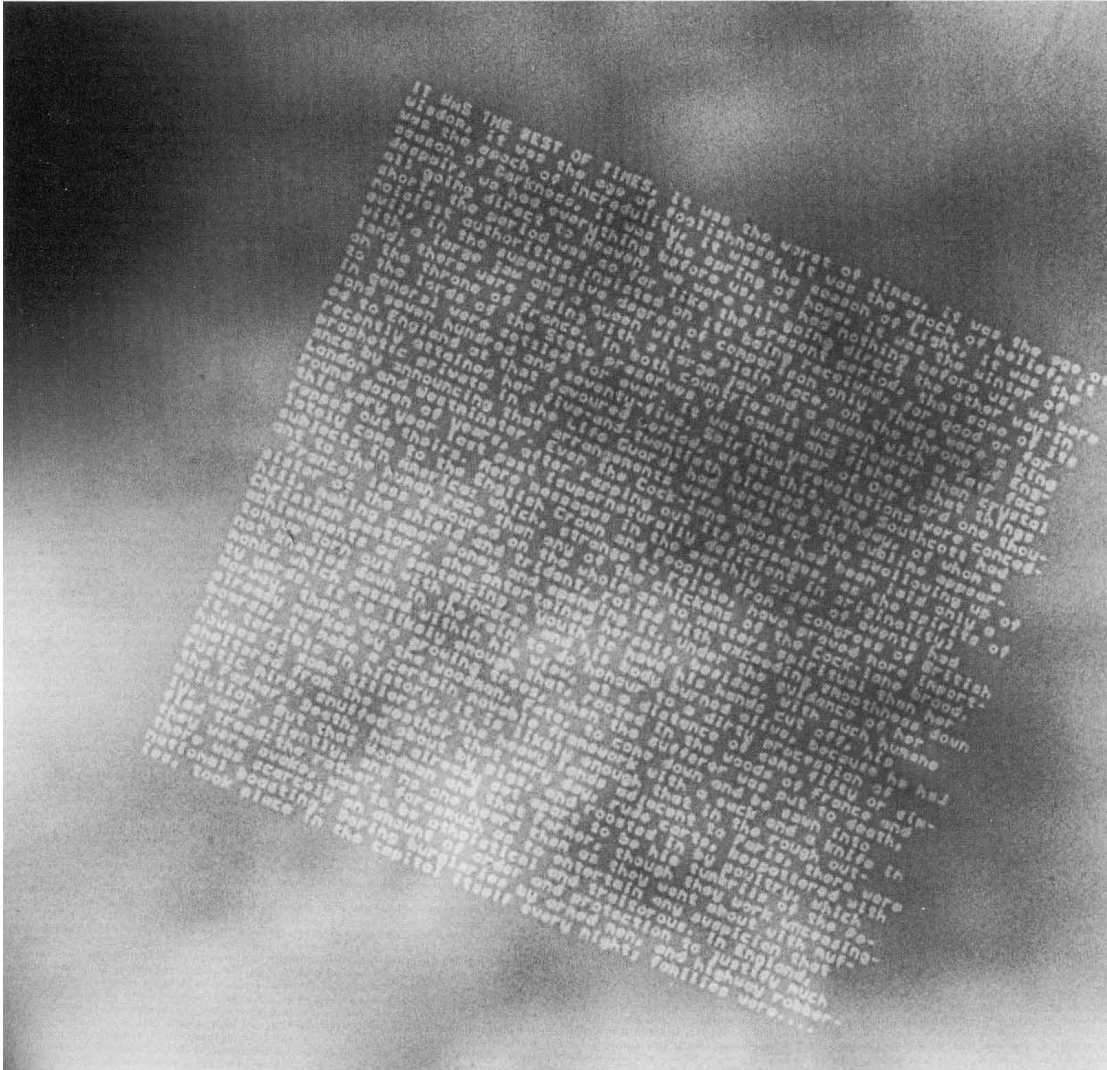


Figure 1.1 – A longstanding Richard Feynman’s challenge to “take the information on the page of a book and put it on an area of $1/25,000$ smaller” [1], which was accomplished 26 years later in 1985 by a graduate student, Tom Newman, using electron-beam lithography. Reprinted with permission from Ref. [2].

undertaken, Ashkin became the oldest recipient of the Nobel prize at the age of 96 for the invention of optical tweezers and their application to biological systems.)

Ever since their invention, optical tweezers have become a useful tool in laboratories. They have been successfully applied to various fields [13–15], notably in biology, to manipulate soft matter such as viruses, living cells, and sub-cellular components [16–18] thanks to their capability to manipulate things in a non-invasive manner. Researchers have also used this technique to measure some of the smallest forces in living matter, produced by motor proteins [19, 20], as well as the elastic properties of DNA molecules [21]. Apart from biological applications, they have provided an ideal test bench to study fundamental physics in colloid and interface sciences [22], ranging from hydrodynamics [23, 24] to thermodynamics [25–27].

In this thesis, we present the application of optical tweezers in two under-explored fields: surface chemistry and nano-optics.

Surface chemistry is the study of chemical phenomena that occur at the interface of two phases. Can we study nanoscale chemical interactions at an interface using an optical tweezer? If we could trap and track a single nanoparticle close to an interface, its trajectory would reveal rich information about what happens at the interface. This tracing analysis is known as single-particle tracking (SPT) and is widely used in life sciences to quantify the dynamics of molecules and proteins in living cells [28–34]. Tracking the movement of an optically trapped particle as opposed to the random diffusion of a free particle has already become a major branch in biophysics [35, 36] due to the wide usage of both the optical tweezer and the SPT in single-molecule research. They are also being implemented together in physics, e.g. in microrheology [37] and hydrodynamics [23, 24]. The major advantage of using an optical tweezer in SPT is that we apply an additional force to the particle (which can be easily modeled as a restoring force and directly inserted into the equation of motion) and obtain a mean to precisely position the particle at the region of interest. However, the combination of these two techniques has not yet emerged in surface sciences, although the SPT alone has been extensively used to study diffusion [38, 39], mass transport [40], catalytic reactions [41], and many other processes [42]. In the first half of the thesis, we demonstrate the viability of optical tweezers in surface chemistry. Especially, optical tweezers enable precise positioning and holding of a particle at an interface, allowing us to observe long-term and real-time interactions that are obscured by conventional ensemble analysis.

Nano-optics, on the other hand, is the study of light–matter interactions on the nanometer scale [43, 44]. Specifically, we are interested in complex phenomena involving metallic nanoparticles that exhibit strong resonant characteristics when illuminated with visible light, also known as localized surface plasmon resonances [45]. These resonances result in intense and confined near-fields around metallic nanostructures, which can be coupled to each other and produce unique optical effects such as spectral shifts [46], Fano resonances [47–49], chi-

rality [50–53], and second-harmonic generation [54]. In the second half of the thesis, we employ optical tweezers to arrange a metallic nanoparticle in a controlled manner to elicit this intriguing coupling effect.

The idea of using optical tweezers for fabricating and assembling nanostructures emerged some time after the invention of optical tweezers [13]. One of the first applications was in microfluidics to create a linear assembly of colloidal microspheres to use as a flap valve in a microfluidic channel (Figure 1.2a), which was not only assembled but also actuated with an optical tweezer [55]. Two-dimensional and three-dimensional free-form assemblies were also subsequently demonstrated using holographic optical tweezers (Figure 1.2b and c) [56, 57]. Recently, assembling plasmonic nanoparticles has been in the limelight due to the unique optical properties of such assemblies. After the first successful demonstration of direct deposition of colloidal metallic nanoparticles on substrates using optical tweezers [58, 59], this technique called optical printing showed possibilities to assemble gold and silver nanoparticles into hetero-dimers [60] or combine a gold nanoparticle into a photonic crystal nanocavity [61]. To our knowledge, however, no attempt has yet been made to combine a colloidal nanoparticle with a complex nanostructure in order to grant new functionalities. In this second section of the thesis, we aim to demonstrate near-field modulation by introducing a new element into a composite optical system using an optical tweezer and to comprehensively study the optical coupling effect resulting therefrom.

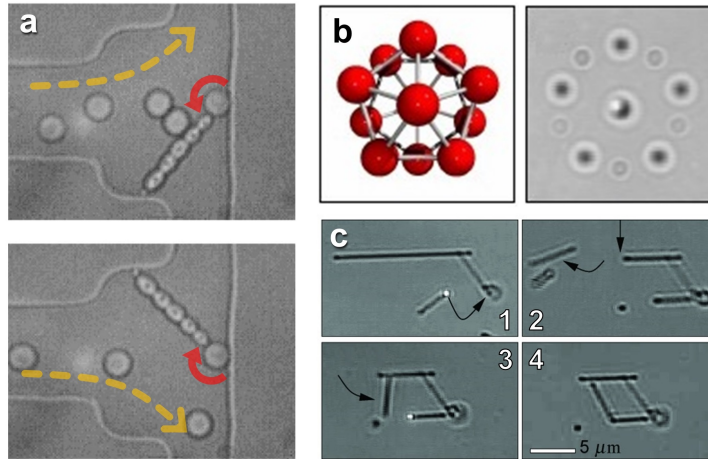


Figure 1.2 – Tweezer-assembled nanostructures. **a**, A colloidal linear structure implemented in a microfluidic channel as a flap valve. The valve can be flipped with an optical tweezer to control the direction of flows, either upward (top) or downward (bottom). Adapted from Ref. [55] with permission. Copyright 2002 American Institute of Physics. **b**, A three-dimensional icosahedron of silica microspheres organized by holographic optical tweezers and fixed by the UV polymerization process. Adapted and reproduced with permission from Ref. [56]. Copyright 2005 Optical Publishing Group. **c**, Assembly of rhombus constructed from semiconductor nanowires using holographic optical traps and a pulsed optical scalpel (Step 1–4). Reproduced with permission from Ref. [57] Copyright 2005 Optica Publishing Group.

Before going into the objectives and organization of the thesis, we would like to first provide in the following subsections a brief description of optical tweezers and plasmonic nanoparticles, which are the two most important components of this thesis.

1.1 Optical manipulation

An optical tweezer uses forces exerted by a highly focused laser beam to trap small objects. To create a tight focal spot, a Gaussian laser beam is typically combined with a high numerical aperture objective lens [62], although alternative methods such as an optical fiber [63] or even computer-generated holograms [64] can also be used. Regardless of the method used to generate the focusing effect, the intensity gradient of the beam draws small objects toward the intensity maximum, whereas the radiation pressure of the beam pushes them along the propagation direction. In cases where the gradient force dominates over the radiation pressure, such as in a tightly focused beam [11], a particle can be trapped near the focal point, as illustrated in Figure 1.3 [13].

The theoretical background of optical tweezers was provided in the early 1970s [65], although its sophisticated aspect is still in development [66–72]. In general, the optical force, which

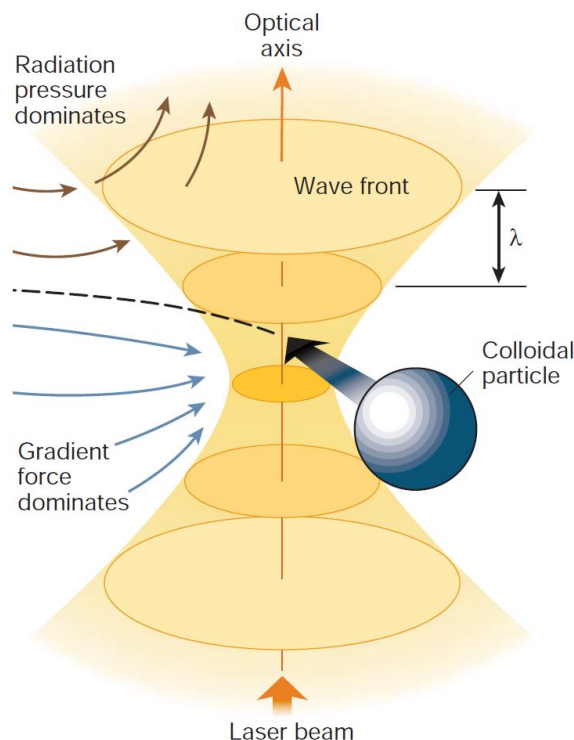


Figure 1.3 – A schematic illustration of an optical tweezer. A colloidal particle can be trapped in three dimensions near the focal point where the gradient force dominates over the radiation pressure. Reprinted with permission from Ref. [13]. Copyright 2003 Springer Nature.

is the force exerted by an optical tweezer, can be explained in different ways depending on the size of particles. For objects much larger than the wavelength of the trapping laser, the optical force can be understood by simply using ray optics [11, 73]. In cases where the particle size is much smaller than the wavelength of the trapping laser (with a particle size $< 1/10$ of the wavelength, the conditions satisfying Rayleigh scattering [74]), the particle can be approximated as a point dipole, and the analytical expression for the optical force can be derived from the Lorentz force law: $\mathbf{F} = q\mathbf{E} + q\mathbf{v} \times \mathbf{B}$, where q is the point charge and \mathbf{v} is its velocity vector. But in most experiments, as in this thesis, the particles are in the order of a few tens of nanometers to a few micrometers, where both the ray optics and the dipole approximation do not give an accurate description of the optical force. In this case, the force can be computed numerically using Maxwell's stress tensor. We also use this approach to study the optical force acting on a plasmonic particle in complex near-fields of a plasmonic antenna in Chapter 5.

Here we briefly state the analytical expression for optical forces when the dipole approximation is valid (Ref. [43] provides a more thorough derivation of optical forces):

$$\langle \mathbf{F} \rangle = \alpha' \nabla \langle |\mathbf{E}|^2 \rangle + \omega \alpha'' \langle \mathbf{E} \times \mathbf{B} \rangle, \quad (1.1)$$

where $\alpha = \alpha' + i\alpha''$ is the complex polarizability of a dipolar particle, ω is the angular frequency of a harmonic electromagnetic field, and $\langle \dots \rangle$ denotes a cycle average. The first term on the right-hand side of Equation 1.1 is the so-called the gradient force, which is proportional to the intensity gradient of the electric fields. This gradient force drives the particle toward the intensity maximum. For a tightly focused beam, the intensity gradient is present in all dimensions and thus creates a three-dimensional optical trap at the focal point.

The second term in Equation 1.1 represents the radiation pressure (momentum transfer) of the trapping beam. It is commonly referred to as the scattering force and, as the expression implies, it is proportional to the average momentum of the electromagnetic field. The scattering force pushes the particle along the propagation direction, causing the final trapping position of a particle in a three-dimensional optical trap to be slightly off the focal point further along the optical axis, where the scattering and gradient forces are balanced. For a highly scattering and lossy metallic particle, the scattering force can dominate and push the particle away from the trap.

1.2 Plasmonic nanoparticles

Plasmonic nanoparticles—most often gold and silver nanoparticles—are discrete metallic particles with distinct resonant properties. Their optical resonances arise from collective oscillations of free electrons in metal nanostructures. The natural frequencies of these oscillations are typically within the visible and near-infrared spectrum and are defined by their material, size, and shape. In other words, when these nanoparticles are illuminated with visible light, they exhibit unique colors depending on their resonance frequencies. On resonance, they

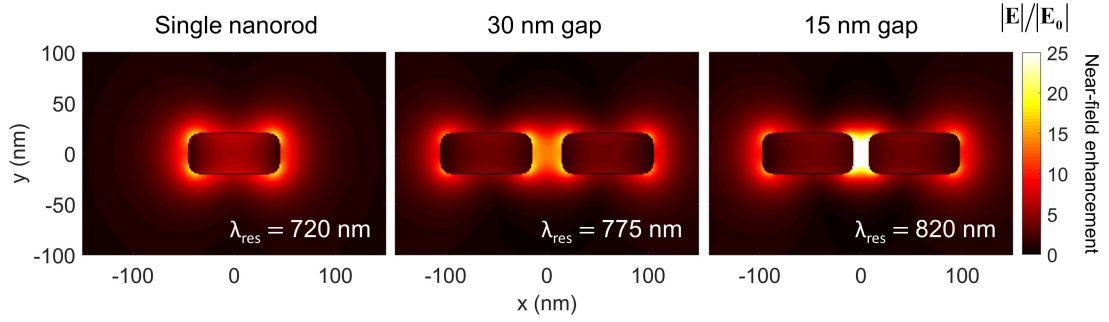


Figure 1.4 – Near-field amplitude enhancement distribution of a single nanorod and dipole nanoantennas. The dipole antennas with double nanorods produce stronger near-fields at their feed gaps than at each end of the single nanorod. When the gap is decreased from 30 nm to 15 nm, the near-field enhancement increases even further due to stronger field confinement at the gap.

can efficiently couple to incident light and give rise to strongly enhanced and confined near-fields [75, 76]. Furthermore, these resonances can be easily tuned by changing their size and shape without changing the chemical composition of materials, which makes them highly appealing in diverse applications [77], ranging from photovoltaics [78, 79] to chemical and biological sensing [80–82].

When we combine such nanoparticles into a composite structure, we can squeeze much more light into a smaller space [83]. Figure 1.4 depicts a simple calculation of near-field amplitude distributions around single and double nanorods. (Since the incident electric field has an amplitude of one, the amplitude distribution can be read directly as an enhancement distribution.) Compared to the electric field of the single nanorod, the electric field of the double nanorods is more concentrated and amplified in the gap, and the field enhancement factor increases substantially as the gap size is reduced by half. The resonant wavelength also shifts due to the coupled oscillation of adjacent electrons separated by the gap; this near-field coupling and the field enhancement in the coupled region are intimately associated [84, 85].

In fact, this double nanorod structure is analogous to dipole antennas in radio and telecommunications [86, 87], and the field confinement in the gap can be used to overcome the diffraction limit of light. For example, Grigorenko *et al.* [88] successfully demonstrated the use of this strong confinement in gold dipole nanoantennas to improve the stiffness of an optical tweezer. Ref. [89] provides a good overview of these techniques called “plasmonic tweezers”. We also study theoretically the near-fields of dipole nanoantennas and the resulting optical forces in Chapter 5, but laying great emphasis on the strong optical interaction between the particle and the nanoantenna.

On the other hand, as one of the consequences of these resonant properties, plasmonic nanoparticles are an efficient nanoscale heater. Once the incident light excites the collective oscillations (plasmons) of the free electron gas, they lose energy by the emission of photons (radiative decay) and collisions with atoms and electrons themselves, which eventually convert

to heat (non-radiative decay) [90]. In the plasmonics community, these thermal effects were considered adverse for quite a long time, but recently, researchers started to exploit them as a nanoscale heat source [91], finding diverse applications in cancer therapy [92–94], photo-thermal chemistry [95–97], and solar light harvesting [98, 99], to name a few.

In this thesis, gold nanoparticles serve two purposes: In the surface chemistry section, gold nanoparticles act as an optical and thermal probe. Gold nanoparticles can be observed under an optical microscope and used as a nanoscale optical probe due to their large scattering cross-sections [100]. We also delve into the unavoidable local heating around the nanoparticles and the heat-induced effects on their surroundings. In the nano-optics section, they serve as building blocks for optically-assembled composite metal nanostructures. As illustrated in Figure 1.4, they can closely interact with adjacent nanostructures once brought close to one another, which can induce a significant change in optical response as an ensemble. This capability to be assembled into a complex optical system has the potential to open up new avenues for designing and arranging plasmonic nanostructures.

1.3 Thesis objectives and organization

This thesis started as a part of an ambitious project entitled “Building tomorrow’s nanofactory”. The primary idea of this project was to bring the concept of assembly line in modern manufacturing industry down to the nanoscale world. What was required in building such a nanofactory was to “develop a process to take a few nanostructures and perform the basic operations required to assemble them into a more complex system” [101]. The role of an optical tweezer was to act as *hands* in the microscopic world.

Specifically, the overarching aim of this thesis was to create an assembly using colloidal nanoparticles and lithographically fabricated nanoantennas. This was an intriguing concept in that it attempted to combine two objects that were created in completely opposite manners: the colloidal particles were chemically synthesized using a bottom-up approach involving nucleation and crystal growth, whereas the nanoantennas were lithographically fabricated using a top-down approach involving selective removal of materials from thin films. Optical tweezers served as a link between these two opposing approaches. Furthermore, by carefully considering the antenna design and arrangement with colloidal particles, we had the potential to tailor the final system to have desired functionalities. We were particularly interested in building an assembly of plasmonic nanostructures due to their strong interaction via near-field coupling.

Based on this motivation, gold nanoantennas and gold nanoparticles were chosen as building blocks. In comparison to other plasmonic materials, gold exhibits excellent stability [102], which was crucial in our study because the nanostructures had to be immersed in an aqueous solution to incorporate colloidal nanoparticles in experiments. For instance, silver nanostructures would quickly deteriorate in such an environment [103, 104]. The large scattering cross-section of gold nanoparticles was both advantageous and disadvantageous from differ-

ent perspectives. From an imaging point of view, they were extremely bright under a dark-field optical microscope, making them excellent imaging probes. In terms of optical trapping, however, it was challenging to trap them in three dimensions due to the large scattering force. We circumvented this issue by trapping the particles close to the surface of substrates so that the vertical movements were suppressed by the scattering force from above and the repulsion with the substrate from below. Because we had to bring the particles close to the antenna on the surface of the substrate, this strategy was also preferable for building an assembly with a nanoantenna.

By trapping these gold nanoparticles directly on the substrate, we made an interesting discovery. In practice, in addition to gold nanoparticles and water, surfactants were added to the colloidal solution to prevent particle aggregation. While observing the motions of trapped particles near the glass substrate, we discovered that their movements varied with the concentration of the surfactant. In other words, the movement of gold nanoparticles was influenced not only by temperature, particle size, and optical trapping potential, but also by interactions with molecules in their surroundings, particularly those adsorbed on solid–liquid interfaces. This discovery prompted us to investigate the use of optically trapped gold nanoparticles to study molecular interactions at interfaces, in addition to our original goal of building a plasmonic assembly.

This thesis is organized as follows. We start by introducing the experimental and numerical methods employed in this thesis in Chapter 2, which covers the trapping and imaging setup built for optical manipulation, the nanofabrication process, and the surface integral equation (SIE) method for numerical calculation, which is the legacy of the Nanophotonics and Metrology Laboratory. We also briefly discuss multiphysics simulation for calculating the temperature of optically trapped particles at the end.

We then proceed with the chapters for the application of optically trapped gold nanoparticles in surface chemistry (Chapter 3 and 4). In both chapters, we study the motions of gold nanoparticles trapped at the water–glass interface of a fluidic chamber in the presence of surfactant molecules. In Chapter 3, we statistically analyze the trapped particles' motions, especially while varying the surface coverages of surfactant assemblies by changing the surfactant concentration. This chapter focuses on the effect of surfactants on optical trapping, particularly those adsorbing on particle and glass surfaces.

In Chapter 4, we examine the same problem from an opposing perspective. We utilize the understanding of particle motion in Chapter 3 to investigate the interactions among surfactant molecules at the narrow gap between the particle and the glass substrate. We extend this study by modifying surfactant morphologies on glass surfaces (from micellar aggregates to bilayer structures) and testing a hypothesis that the morphology of surfactant self-assemblies can influence the particle–surface interactions. This chapter aims to prove the possibility of optically trapped gold nanoparticles as a nanoscale optical probe for interface science.

The following two chapters, Chapter 5 and Chapter 6, deal with the application of optical

tweezers in nano-optics. In Chapter 5, we first investigate the optical forces experienced by a gold nanoparticle near a gold dipole antenna. In particular, we examine the effect of the particle's presence in the near-field of the dipole antenna and the consequent changes in the optical force. While Chapter 5 is concerned with a theoretical investigation of the optical force, Chapter 6 is about the experimental demonstration of plasmonic assemblies realized by an optical tweezer, which is the ultimate objective of this thesis. We attempt to interpret the experimental results with a coupled oscillator model and provide a comprehensive analysis based on this model.

Each chapter from Chapter 3 to 6 comes with an introduction and a conclusion. In Chapter 7, we conclude this thesis with a summary of each topic and a discussion of future research.

2 Experimental and numerical methods

2.1 Overview

This chapter provides an overview of the experimental and numerical methods employed in this thesis. In particular, we discuss the strategies frequently employed throughout the thesis. Methods specific to each study will be presented separately in the Method section of the corresponding chapter.

In Section 2.2 and 2.3, we discuss experimental methods. We start by describing the essential sample preparation steps (Section 2.2.1), followed by the optical setup for trapping and imaging (Section 2.2.2 and Section 2.2.3). In Section 2.2.4, we address the characterization of colloidal particles, including zeta potentials and hydrodynamic size measurements. Next, we introduce a fabrication process for plasmonic nanoantennas in Section 2.3. We provide a brief description of the process flow associated with electron-beam lithography.

In Section 2.4 and 2.5, we discuss numerical simulation methods, including a surface integral equation (SIE) method and optical heating simulation using COMSOL Multiphysics. The SIE method is introduced as the primary simulation tool used in this thesis. In SIE simulation, surface currents defined on the boundaries of scatterers are initially calculated. Then, using the SIE surface currents, we derive secondary quantities such as optical cross-sections, near-field distributions, and dipole moments. The steps for computing these secondary quantities are provided in Section 2.4.1.

Finally, in Section 2.5, we present the simulation method for electromagnetic heating using COMSOL Multiphysics. We simulated the temperature distribution of the studied systems in order to estimate the temperature of optically trapped particles, nanoantennas, and surrounding media (including glass and water). In this section, we briefly introduce how to calculate optical heating using COMSOL, which combines an electromagnetic simulation with a heat transfer simulation.

2.2 Experimental methods

Colloidal nanoparticles suspended in water are the target systems for optical manipulation in this thesis. Once trapped, a single particle can act like an optical probe for investigating its surroundings, or more interactively, it can induce a strong coupling with a lithographically fabricated nanostructure. Three major steps are commonly involved in both experiments: sample preparation, optical manipulation, and observation. In addition, the colloidal characteristics are characterized to assure the dispersity of the solution.

2.2.1 Sample preparation

Sample preparation includes a dilution of colloidal solution and the formation of a fluidic chamber. We purchased commercially available nanoparticle solutions (e.g. gold colloids from Sigma-Aldrich), which usually have high particle concentrations. To ensure the trapping of a single particle, the particle solutions were diluted until they appeared scarce under an optical microscope. Due to the different particle concentrations for the various products, the dilution factor varied. To prevent particle aggregation, surfactants (cetyltrimethylammonium chloride, CTAC) were added during dilution. The effects of surfactants will be examined in detail in Chapter 3.

The nanoparticle suspensions were first separated from the buffer solution by centrifugation. The appropriate centrifugal force depended on the particle's size and composition and was therefore adjusted accordingly for optimal separation. For gold nanoparticles with a diameter of 150 nm, for instance, a volume of 1 mL was centrifuged at 200 g for 30 minutes (Fisherbrand GT2R Centrifuge). After carefully removing the supernatant, the residue was re-dispersed in a surfactant solution using a vortex mixer. At this stage, the particle concentration was adjusted by diluting the particle-surfactant mixture with a particle-free surfactant solution of the same concentration.

A fluid chamber was constructed using a pair of borosilicate glass coverslips (145 μm in thickness) and a double-sided adhesive spacer (120 μm in thickness, Grace Bio-Labs SecureSealTM imaging spacer). We slightly overfilled the chamber with the dilute particle-surfactant mixture to minimize the air bubbles trapped inside the chamber. To prevent the liquids from evaporating, all trapping experiments were conducted within the fluid chamber. All glass coverslips were sonicated in acetone and isopropyl alcohol baths for 30 minutes each before use.

2.2.2 Trapping setup

Figure 2.1 shows the schematic of the optical trapping and imaging system used in this study. We used a He-Ne laser as a trapping laser. The laser beam propagated from the top to the bottom of a sample. A dry objective lens (60 \times , 0.85 NA) was used to focus the trapping laser on the sample surface. The laser power was regulated before entering the trapping objective

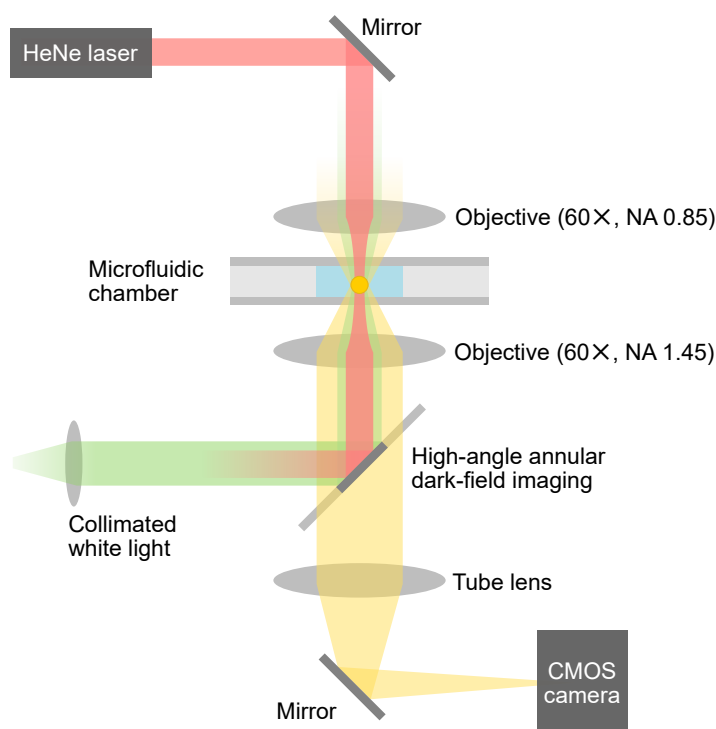


Figure 2.1 – Overview of the optical set-up (not to scale).

using a laser-line variable beamsplitter (VA5-633, Thorlabs). The trapping objective lens was mounted on a piezoelectric stage for precise adjustment of the focal point (i.e., the trap position).

Contrary to a typical optical trapping setup, the laser beam was not expanded and therefore did not entirely fill the entrance pupil of the trapping objective lens. The resulting loosely-focused laser beam produced a strong radiation pressure and a weak lateral trap. As a result, the strong radiation pressure brought the particle close to the bottom surface of a fluid chamber, providing vertical confinement. Simultaneously, the moderate optical restoring force restricted the diffusion of the particle in a confined area in lateral directions. The particle's vertical position was determined by the balance between the radiation pressure of the laser beam and the electrostatic repulsion with the glass substrate. For each measurement, we pushed the particle toward the glass surface until it was most stably trapped laterally. This indicated that the beam waist was located at the point where the radiation pressure and electrostatic repulsion were balanced.

2.2.3 Imaging setup

The imaging system is essentially a reflected dark-field microscope (Figure 2.1). The imaging setup was built on a commercial optical microscope (IX71, Olympus) with a 60x, 1.45 NA, oil-immersion objective (PLAPON 60xO TIRFM, Olympus). The samples were illuminated

from below through the objective (the green-colored beam in Figure 2.1). The backward scattered light from the specimen (the yellow-colored beam in Figure 2.1) was collected by the same objective lens and transmitted through a dark-field filter. The dark-field filter is a transparent plate with a small elliptical silvered mirror in the center, tilted at 45 degrees to the optical path. The projection of this elliptical mirror onto the transverse plane is a circular light stop, which blocks the direct reflection of the light source and the trapping laser, and transmits only the high-angle part of the scattering to form a dark-field image. The sample stage incorporated a three-dimensional piezoelectric translation for the high precision control of the sample position.

The advantage of this dark-field microscope is that it eliminates the light from the background and thus provides high signal-to-noise ratios in the final images, especially for plasmonic nanoparticles. Imaging and video recording were performed with a CMOS camera (CM3-U3-50S5C-CS, FLIR). The imaging channel was additionally connected with a spectrograph (Andor Technology's Shamrock 303i) to examine the spectra of trapped particles or nanostructures.

2.2.4 Characterization of colloidal properties

The characteristics of colloidal particles, including their hydrodynamic sizes and zeta (ζ) potentials, were measured using Zetasizer Nano ZS from Malvern Panalytical. Zetasizer has two major techniques: dynamic light scattering and laser doppler velocimetry. Dynamic light scattering (DLS) measures the Brownian motion of colloidal suspensions and relates this to the size of the particles. Laser doppler velocimetry (LDV) measures the velocity of charged particles when an electric field is applied and relates this to the zeta potential of the particles. Both techniques require a laser beam and detect a fluctuating intensity signal caused by the scattering of particles.

Zeta (ζ) potentials

Zeta (ζ) potential is the electrical potential at the slipping plane of a particle suspended in a medium (Figure 2.2). A slipping plane is the plane near a dispersed particle that separates the bulk fluid from the fluid that remains attached to the particle surface. Since this attached layer moves together with the particle in an electric field, the electric potential at this plane is a readily measurable quantity and an important indicator of colloidal stability.

For performing ζ potential measurements, a disposable folded capillary cell (DTS 1060 from Malvern Panalytical) was used to contain the particle solution. When an electric field was applied across the capillary cell, the Zetasizer measured the velocity of charged particles attracted toward the electrode of opposite charge. The velocity of a particle in an electric field is commonly referred to as its electrophoretic mobility. Then the apparent ζ potentials can be

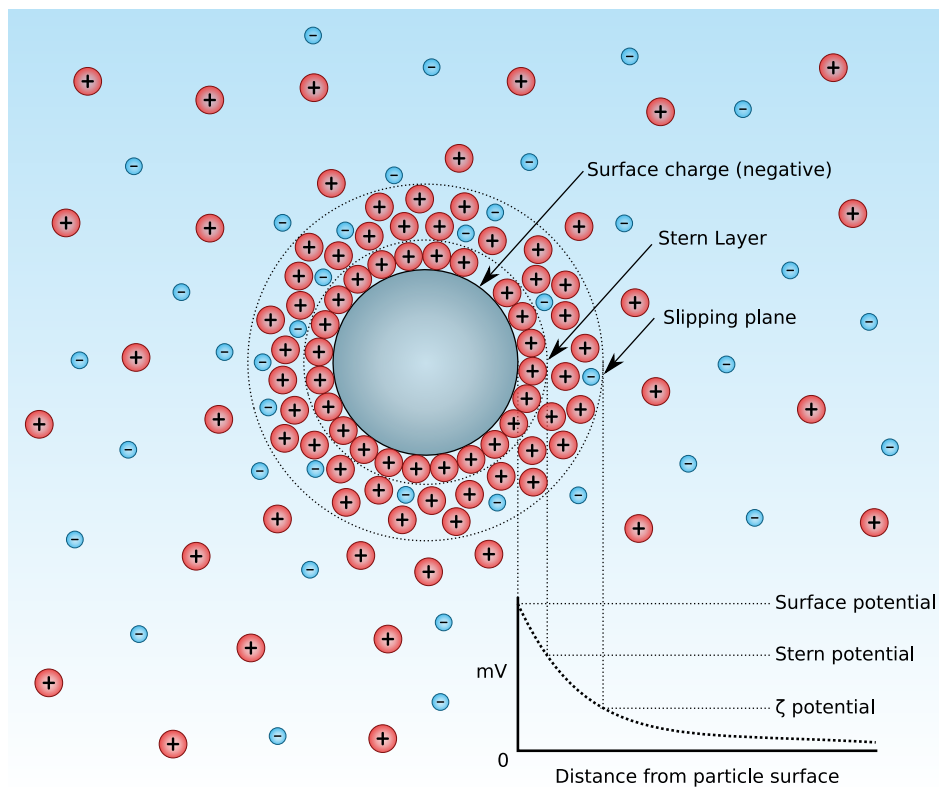


Figure 2.2 – Diagram showing the ionic concentration and potential difference as a function of distance from the charged surface of a particle suspended in a dispersion medium. Reprinted from Wikimedia Commons, 2012. Distributed under a CC-BY-SA-3.0 license.*

* URL: https://commons.wikimedia.org/wiki/File:Diagram_of_zeta_potential_and_slipping_planeV2.svg

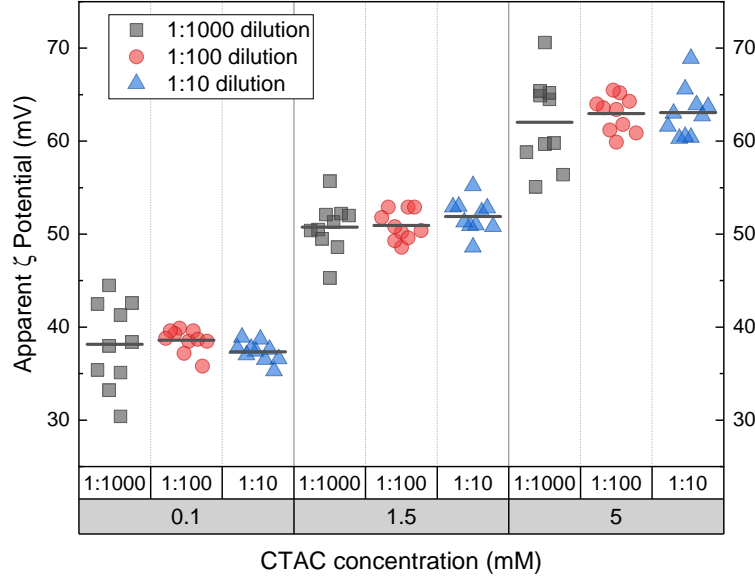


Figure 2.3 – Effect of colloid concentration on its zeta potential. The original colloid stock concentration is diluted 10 to 1000 times to observe the changes in its zeta potential. Three surfactant (CTAC) concentrations (0.1, 1.5, and 5 mM) are examined. Solid horizontal bars indicate the average values for 10 measurements for each condition. The lowest particle concentration is subject to a large variance due to a low signal-to-noise ratio.

inferred from the measured electrophoretic mobility using Henry's equation [105]:

$$\frac{U}{E} = \frac{2\epsilon\zeta F(\kappa a)}{3\eta}, \quad (2.1)$$

where U/E is the electrophoretic mobility ($\text{m}^2\text{s}^{-1}\text{V}^{-1}$), ζ is the zeta potential (V), ϵ is the solvent dielectric permittivity ($\text{kg m V}^{-2}\text{s}^{-2}$), η is the viscosity ($\text{kg m}^{-1}\text{s}^{-1}$), and $F(\kappa a)$ is Henry's function (dimensionless). For nanoparticles in aqueous media, the value of $F(\kappa a)$ is often approximated as 1.5 (also known as the Smoluchowski approximation). We used this value for our ζ calculation.

The particle concentration was also adjusted for optimal ζ measurements. Figure 2.3 shows the effect of gold colloid concentration on the ζ measurements. The average ζ potentials remain independent of dilution factors, but the lowest particle concentration is subject to large variance due to a low signal-to-noise ratio. Therefore, we increased the particle concentration compared to that for trapping in order to have reliable ζ measurements.

Hydrodynamic size distribution

The primary quantity that DLS measures is the intensity fluctuation of a laser beam scattered by the particles. When correlating scattering intensity fluctuation data with size distributions,

the Zetasizer generates three different types of distributions: intensity, volume, and number distributions. The intensity distribution is the fundamental distribution directly obtained from DLS. This distribution can be converted to a volume distribution using Mie theory, and further to a number distribution. We used the basic intensity distribution for our size analysis since the other secondary distributions are likely to be influenced by the noise of the data.

2.3 Nanofabrication

Plasmonic nanoantennas typically have nanometer-scale dimensions. We fabricated plasmonic nanostructures using electron-beam (e-beam) lithography, which we then used to examine intimate interactions with colloidal gold nanoparticles (Chapter 6). The procedure included substrate preparation, e-beam lithography, evaporation of metal layers, and a lift-off process.


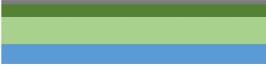




The substrate had to be cleaned and dehydrated as the initial step in the procedure. As a substrate, we chose a glass wafer that was 150 μm -thick. This substrate thickness was necessary due to the short working distance of our high NA imaging objective. First, a 7-minute oxygen plasma treatment at 500 W was applied to the substrate (Tepla GigaBatch), which made the glass surface clean, dry, and hydrophilic (hence better adhesion with the resist). The wafer was then heated on a hot plate at 180°C for 5 minutes for complete dehydration.

E-beam lithography was the next step. A PMMA/PMMA bilayer served as our e-beam resist. PMMA (poly(methyl methacrylate)) is a positive e-beam resist consisting of long polymer chains. When exposed to an electron beam, the long polymer chains break down and become soluble to the developer. The two standard molecular weights of PMMA employed in this study were 495K and 950K. The lower molecular weight PMMA degrades more quickly than the higher molecular weight PMMA under the same exposure, resulting in a larger opening after development. We created an undercut profile using this PMMA/PMMA bilayer, which aided in the lift-off process. For the purpose of preventing charge buildup on the dielectric surface during e-beam exposure, a thin Cr layer was placed on top of the bilayer. The prepared wafer was then exposed to a high-energy electron beam with an optimized dose and beam current (typically between 700–1000 $\mu\text{C}/\text{cm}^2$ for the dose and 100–300 pA for the beam current). Within a few hours after exposure, the wafer had to be developed for 1 minute into (MiBK):(isopropanol(IPA)) 1:3 developer and rinsed with IPA for another minute.

Dehydration was a crucial step prior to the metal evaporation process. Before metal deposition, the wafer must be entirely dried since water molecules on the surface could disrupt the growth of the film by diffusing through the metal grains. For this, we kept our wafers in a dry nitrogen chamber for a few days.

We used gold as a material for plasmonic nanoantennas to exploit its plasmonic properties and stability. A thin (roughly 2 nm) Cr was first evaporated on the wafer to form an adhesion layer and then followed by the evaporation of a 40 nm-thick gold. The metal layer's thickness

Table 2.1 – Process flow for nanoantenna fabrication using e-beam lithography.

| Steps | Cross-sections | Descriptions |
|-------|---|---|
| 1 |  | Substrate preparation - 150 μm -thick glass substrate - Oxygen plasma treated - Dehydrated |
| 2 |  | Resists coating - Bilayer e-beam resists (PMMA/PMMA) - Conducting layer (Cr) deposited on the top |
| 3 |  | E-beam exposure - High resolution down to 20 nm or less - Positive resists |
| 4 |  | Resists development - Cr-layer etched - Developed in PMMA developer solution - Descum process included - Dried for several days (dehydration) |
| 5 |  | Evaporation of metal layers - Adhesion layer (Cr) 2 nm - Gold layer 40 nm |
| 6 |  | Lift-off process - Acetone bath - Rinsing and drying |

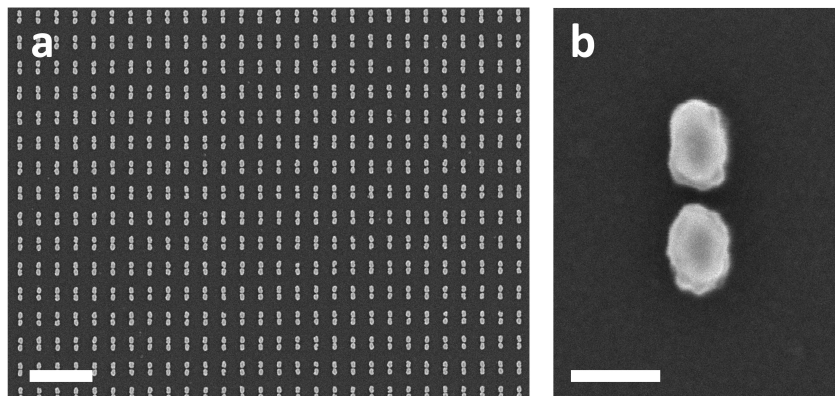


Figure 2.4 – Scanning electron microscope (SEM) images of example plasmonic nanoantennas fabricated by the e-beam lithography process. **a**, A dense dipole antenna array. Scale bar, 1 μm . **b**, A single dipole antenna. The gap size is roughly 15 nm. Scale bar, 100 nm.

determined the nanostructure's height.

After the evaporation step, the resist layer was lifted off while being immersed in an acetone bath for a few days; the lift-off took place very slowly through the edge of the wafer. The wafer was next cleaned with fresh acetone and IPA, dried, and diced for use in studies for trapping. The comprehensive process flow is shown in Table 2.1. The cross-sections of the chip are depicted (dimensions not to scale) with brief descriptions.

Figure 2.4 illustrates examples of nanoantennas fabricated using the e-beam lithography process. The resolution of the procedure ranged from 5 to 10 nm. The dense array in Figure 2.4a was made for imaging purposes and was not used in trapping experiments. The nanoantennas used in experiments were spaced at least 4 microns apart to allow spectral measurements of single nanostructures.

2.4 Numerical simulation

In addition to particle-trapping experiments, the numerical simulation of plasmonic nanostructures is one of the major components of the thesis. Some of the key calculations include scattering cross-sections, near-field distributions, optical forces, polarization charges, and temperature distributions. This information gives valuable insights into the behaviors of a trapped particle near an optical antenna and how they interact with each other.

2.4.1 Surface integral equation (SIE) method

We used the surface integral equation (SIE) method for our electromagnetic simulation. It solves Maxwell's equations in the integral form in the frequency domain. One of the advantages

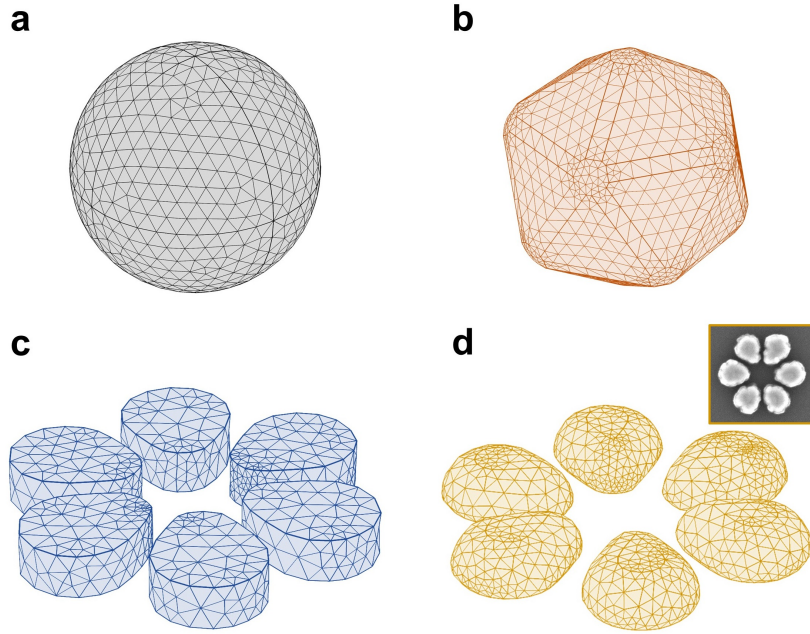


Figure 2.5 – Simulation mesh examples. **a**, Mesh for a perfect sphere. This mesh can represent a nanoparticle used for trapping experiments. **b**, Mesh for a gold nanoparticle having a quasi-spherical shape. Considering the crystal growth of gold colloids, a truncated icosahedron can represent more realistic shapes. **c**, Example nanoantenna structure. **d**, More realistic mesh for the same structure. Smoothing the sharp edges can better depict lithographically fabricated structures (inset: a scanning electron microscope image for a fabricated nanoantenna).

of SIE is that it requires a discrete mesh only on the boundaries of scatterers. This reduces computational costs while allowing realistic representation of surfaces. We followed the formulation of SIE and its treatment in Ref. [106]. Following is an overview and the brief description of its basic implementations.

Three basic steps are involved in the SIE simulation process:

1. Generating a simulation mesh
2. Computing surface currents on the mesh
3. Post-processing the surface currents

A simulation mesh refers to a discrete triangular mesh defined on simulation geometries. Some example meshes generated by commercial software, COMSOL Multiphysics, are shown in Figure 2.5. Depending on accuracy requirements, one can choose ideal shapes as a prototype (Figures 2.5a and c) or more realistic shapes (Figures 2.5b and d). The size of the mesh elements can also be adjusted with a trade-off between the calculation accuracy and the computational costs. However, the mesh should be fine enough to resolve all expected field dynamics [107].

The next step is setting a simulation condition and solving Maxwell's equations numerically. The input quantities are incident fields and material parameters for each geometrical domain. The output quantities are the surface electric and magnetic currents defined on the simulation mesh. The basic idea is to use a popular technique called the method of moments (MoM) [108]. Details on the calculation process can be found in Ref. [106].

The final process is post-processing the surface currents to obtain meaningful physical values. The surface currents determined in the previous step are not actual physical currents. Instead, they have the equivalent effect to the scattering of an object defined by the same mesh. The following subsections briefly show how to compute the secondary quantities from the surface currents.

Electric (E) and magnetic (H) fields

Electromagnetic fields can be the most fundamental quantities we can seek from the surface currents. Once the surface currents are computed, the electric (**E**) and magnetic (**H**) fields at any position can be found using the following surface integral equations [106]:

$$\mathbf{E}_i(\mathbf{r}) = \mathbf{E}_i^{\text{inc}}(\mathbf{r}) - i\omega\mu_i \int_{\partial\Omega_i} dS' \bar{\mathbf{G}}_i(\mathbf{r}, \mathbf{r}') \cdot \mathbf{J}_i(\mathbf{r}') - \int_{\partial\Omega_i} dS' [\nabla' \times \bar{\mathbf{G}}_i(\mathbf{r}, \mathbf{r}')] \cdot \mathbf{M}_i(\mathbf{r}'), \quad (2.2a)$$

$$\mathbf{H}_i(\mathbf{r}) = \mathbf{H}_i^{\text{inc}}(\mathbf{r}) - i\omega\epsilon_i \int_{\partial\Omega_i} dS' \bar{\mathbf{G}}_i(\mathbf{r}, \mathbf{r}') \cdot \mathbf{M}_i(\mathbf{r}') + \int_{\partial\Omega_i} dS' [\nabla' \times \bar{\mathbf{G}}_i(\mathbf{r}, \mathbf{r}')] \cdot \mathbf{J}_i(\mathbf{r}'), \quad (2.2b)$$

where

- i denotes the domain (Ω) index, assuming i number of domains ($\Omega_1, \Omega_2, \dots, \Omega_i$),
- the subscript 'inc' denotes the incident field,
- μ is the magnetic permeability, and ϵ is the electric permittivity,
- $\bar{\mathbf{G}}$ is the dyadic Green's function,
- \mathbf{J} and \mathbf{M} are the surface electric and magnetic currents.

Optical cross sections

For scattering cross-section, we first suppose an imaginary sphere for integration, whose radius is much larger than the scatterer (e.g. 50 microns) such that we can compute far-field values on this sphere. Figure 2.6 shows a set of dense points generated on this sphere. The **E** and **H** fields are evaluated on these points, and the scattered electric (\mathbf{E}_{scat}) and magnetic (\mathbf{H}_{scat}) fields are computed based on the following simple relations: $\mathbf{E}_{\text{scat}} = \mathbf{E} - \mathbf{E}_{\text{inc}}$ and $\mathbf{H}_{\text{scat}} = \mathbf{H} - \mathbf{H}_{\text{inc}}$. Finally, the scattering cross section is calculated based on its definition:

$$\frac{\text{Total scattered power integrated over the sphere}}{\text{Incident power per unit area}}, \text{ which is an area.}$$

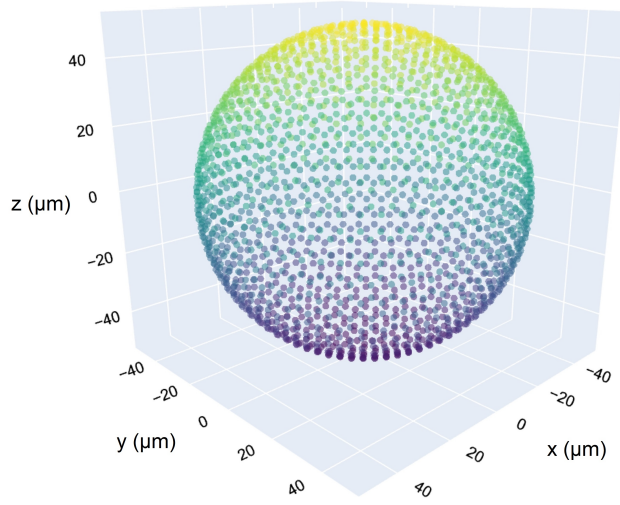


Figure 2.6 – Points on a sphere for evaluating far-field electric and magnetic fields. The sphere radius is 50 microns, which is much larger than the dimension of the nanostructures in this study (typically 100 – 300 nm) and the wavelength of light (400 – 900 nm).

The scattered and incident power can be obtained from the time-averaged Poynting vector:

$$\mathbf{S}_k = \frac{1}{2} \mathbf{E}_k \times \mathbf{H}_k^*, \quad (2.3)$$

where $k = \text{scat or inc}$, and $*$ denotes the complex conjugate.

Likewise, the extinction cross-section can be calculated by dividing the total extinction power by the incident power per unit area. The corresponding extinction Poynting vector is defined as:

$$\mathbf{S}_{\text{ext}} = \frac{1}{2} \text{Re} \{ \mathbf{E}_{\text{inc}} \times \mathbf{H}_{\text{scat}}^* + \mathbf{E}_{\text{scat}} \times \mathbf{H}_{\text{inc}}^* \}. \quad (2.4)$$

Near-field distributions

Near fields can also be calculated using surface currents as described in Equations 2.2a and 2.2b. In particular, thanks to the implementation of a singularity subtraction technique [106], the SIE simulation tool used in this study enhances near-field accuracy by performing singular integrals analytically. Similar to the far-field evaluation, a two-dimensional point grid of interest is first defined near the simulated structure(s), and the field values are calculated on these points using Equations 2.2a and 2.2b. A fine simulation mesh is required to accurately represent field variations, especially in regions where the fields change rapidly, such as sharp corners and narrow gaps. For instance, in the case of a dipole nanoantenna with a narrow gap, the maximum side length of a triangular mesh was defined to be 1/5 of the gap distance.

Optical forces

An optical force on a nanoparticle can be calculated in two ways: The first approach is to find it analytically based on the assumption that the particle can be approximated as a dipole. This approach will be discussed in detail in Chapter 5. The second approach is a numerical method using Maxwell's stress tensor. This subsection describes the numerical method used in this thesis, which uses surface currents obtained from the SIE calculation.

We start with a traction vector \mathbf{T} , which is the internal force vector on a cross-section divided by the area of the cross-section:

$$\mathbf{T} = \frac{\mathbf{F}_{\text{internal}}}{\text{area}}.$$

Based on its definition, if we integrate the traction vector over a surface enclosing a nanoparticle, we obtain the net force acting on the particle:

$$\mathbf{F} = \oint_S \mathbf{T} ds, \quad (2.5)$$

where S is an arbitrary surface enclosing the particle, and ds is an infinitesimal surface element. The traction vector \mathbf{T} can be expressed as a dot product of a stress tensor σ and a normal vector \mathbf{n} :

$$\mathbf{T} = \sigma \cdot \mathbf{n}, \quad (2.6a)$$

$$\text{or in tensor notation: } T_i = \sigma_{ij} n_j. \quad (2.6b)$$

The stress tensor of an electromagnetic field can be defined as follows:

$$\sigma_{ij} = \varepsilon_0 E_i E_j + \mu_0 H_i H_j - \frac{1}{2}(\varepsilon_0 E^2 + \mu_0 H^2) \delta_{ij}, \quad (2.7)$$

which is called Maxwell's stress tensor. The Kronecker's delta δ_{ij} at the end of the equation is defined as:

$$\delta_{ij} = \begin{cases} 0 & \text{if } i \neq j, \\ 1 & \text{if } i = j. \end{cases} \quad (2.8)$$

Following Equation 2.5, a time-averaged optical force $\langle \mathbf{F} \rangle$ can be obtained from a time-averaged stress tensor $\langle \sigma \rangle$:

$$\langle \mathbf{F} \rangle = \oint_S \langle \mathbf{T} \rangle ds = \oint_S \langle \sigma \cdot \mathbf{n} \rangle ds = \oint_S \langle \sigma \rangle \cdot \mathbf{n} ds, \quad (2.9a)$$

$$\langle \sigma_{ij} \rangle = \frac{1}{2} \text{Re} \left[\varepsilon_0 E_i E_j^* + \mu_0 H_i H_j^* - \frac{1}{2}(\varepsilon_0 E E^* + \mu_0 H H^*) \delta_{ij} \right], \quad (2.9b)$$

assuming that the field has harmonic time dependence ($e^{-i\omega t}$).

Calculating an optical force using Equations 2.9a and 2.9b is a common and straightforward approach. This approach includes the steps below:

1. Generating a point grid on a sphere enclosing the particle of interest,
2. Evaluating \mathbf{E} and \mathbf{H} fields on these points,
3. Calculating time-averaged stress tensors using the \mathbf{E} and \mathbf{H} fields in Step 2,
4. Integrating the stress tensors over the sphere.

However, if we can calculate stress tensors directly from the surface currents, we can eliminate Steps 1–3 and significantly reduce computational costs and errors arising from these steps [109]. In this case, the arbitrary surface for stress tensor integration becomes the simulation mesh itself, which defines the particle geometry. To this end, we need to evaluate the electric and magnetic fields on the surface mesh that can be directly plugged into Equation 2.9b. The \mathbf{E} and \mathbf{H} fields parallel and perpendicular to the simulation mesh can be directly expressed from the surface electric and magnetic currents (\mathbf{J} and \mathbf{M}):

- Parallel:

$$\mathbf{E}_{\parallel} = \hat{\mathbf{n}} \times \mathbf{M}, \quad (2.10a)$$

$$\mathbf{H}_{\parallel} = \mathbf{J} \times \hat{\mathbf{n}}. \quad (2.10b)$$

- Perpendicular:

$$\mathbf{E}_{\perp} = -\frac{i}{\omega \epsilon_0 \epsilon_r} (\nabla \cdot \mathbf{J}) \hat{\mathbf{n}}, \quad (2.11a)$$

$$\mathbf{H}_{\perp} = -\frac{i}{\omega \mu_0 \mu_r} (\nabla \cdot \mathbf{M}) \hat{\mathbf{n}}. \quad (2.11b)$$

The total surface fields are the sum of the parallel and perpendicular fields: $\mathbf{E} = \mathbf{E}_{\parallel} + \mathbf{E}_{\perp}$ and $\mathbf{H} = \mathbf{H}_{\parallel} + \mathbf{H}_{\perp}$.

By plugging in the total surface fields to Equation 2.9b, we get the time-averaged Maxwell's stress tensor directly in terms of the surface currents \mathbf{J} and \mathbf{M} on the particle mesh:

$$\begin{aligned} \langle \sigma_{ij} \rangle = \frac{1}{2} \left[\frac{(\nabla \cdot \mathbf{M})(\nabla \cdot \mathbf{M}^*)}{\omega^2 \mu_0} + \frac{(\nabla \cdot \mathbf{J})(\nabla \cdot \mathbf{J}^*)}{\omega^2 \epsilon_0} - (\epsilon_0 \mathbf{M} \cdot \mathbf{M}^* + \mu_0 \mathbf{J} \cdot \mathbf{J}^*) \right] \hat{\mathbf{n}} \\ + \frac{i}{\omega} [(\mathbf{J} \times \hat{\mathbf{n}})(\nabla \cdot \mathbf{M}^*) + (\hat{\mathbf{n}} \times \mathbf{M})(\nabla \cdot \mathbf{J}^*)] \end{aligned} \quad (2.12)$$

Finally, the total force acting on the particle is

$$\mathbf{F} = \sum_T \int_T \langle \sigma_{ij} \rangle n_j dS_T, \quad (2.13)$$

where T are the triangles on the particle surface. We use Equations 2.12 and 2.13 for calculating the numerical force directly from surface currents.

Polarization charges

When we shine light on a metallic nanostructure, the light induces a polarization of the electron cloud in the nanostructure. The electron cloud oscillates with the electric field like a harmonic oscillator driven by an external force. At a particular point in time, one can visualize such polarization charges as a charge density distribution [110]. For a simple structure like a sphere, one can find that the negative charges (the electrons) are pushed toward one side of the structure, leaving the positive charges (the nuclei) on the other side along the direction of the electric field. Such an example is shown in Figure 2.7b.

The density distribution of polarization charges can give insights into how electrons interact with an external field. For instance, Figure 2.7b indicates that the field induces a dipole-like charge distribution. However, polarization charges can become much more intricate for composite structures. Therefore, the visualization of polarization charges also provides additional information on the interactions between the elements of a composite nanostructure through near-field coupling.

We calculate polarization charges from surface currents. More precisely, we visualize the distribution of surface charge density on the boundaries, which is equivalent to that of volume charge density. Once the electric fields inside and outside of an interface are known, the surface charge density can be expressed in terms of the discontinuity in the normal component of the electric fields using Gauss's law:

$$\sigma_p = \epsilon_0(\mathbf{E}_{\text{out}} - \mathbf{E}_{\text{in}}) \cdot \hat{\mathbf{n}}. \quad (2.14)$$

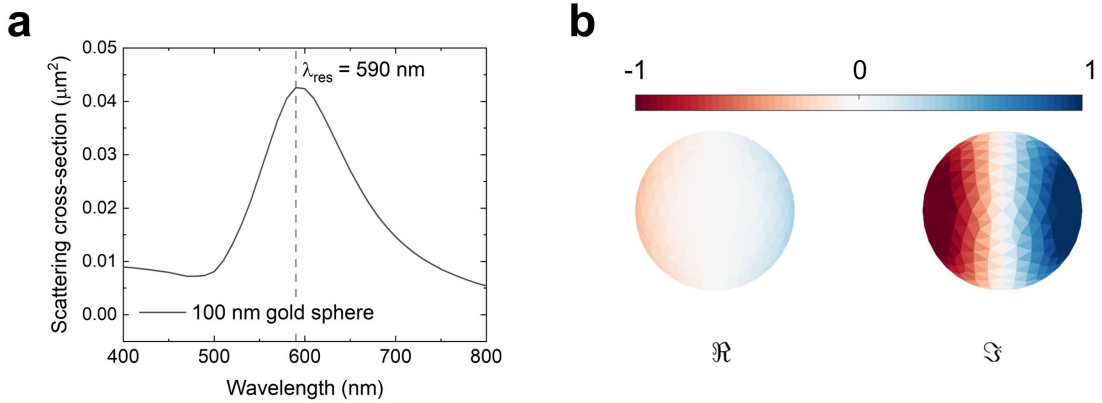


Figure 2.7 – Optical response of a 100 nm gold sphere (a) and its polarization charge distribution at the resonant wavelength (b). The light is polarized in the horizontal direction. A polarization charge is a complex number, thus the magnitudes of the real and imaginary parts are shown separately. At the resonant wavelength (590 nm as shown in a), the phase lags behind the external driving field by $\pi/2$ (not shown), resulting that the imaginary part contains most of the polarization response.

Since the normal component of the electric field can be directly obtained from the surface current using Equation 2.11b, the surface charge density σ_p can be expressed with the surface current \mathbf{J} :

$$\sigma_p = -\frac{i}{\omega} \left(\frac{1}{\varepsilon_{r,\text{out}}} - \frac{1}{\varepsilon_{r,\text{in}}} \right) \nabla \cdot \mathbf{J}. \quad (2.15)$$

We use Equation 2.15 for visualizing surface polarization charge. The calculated charge density is a complex number, containing the phase delay with respect to the excitation field. Thus, we visualize polarization charges using both real and imaginary parts. For a simple dipole mode, the phase shift varies from 0 (low frequency) to π (high frequency). At resonance, the phase shift becomes $\pi/2$ for a single harmonic oscillator. The resulting polarization response therefore moves back and forth between the real and imaginary parts while sweeping the incident frequency.

Dipole moments

A dipole moment is a measure of the separation of positive and negative charges within a system. The polarization charges we discussed in the previous subsection can therefore be quantified by the dipole moment. Multipole moments can also be required to describe more complex charge distributions, but we focus on the dipole moment in this thesis, which is sufficient for the nanoparticles at hand.

The basic definition of the dipole moment of two charges ($+q$ and $-q$) is

$$p = qd, \quad (2.16)$$

where d is the separation distance. For a charge distribution over a surface, the dipole moment can be expressed as a surface integral of charge density multiplied by the position vector \mathbf{r}' :

$$\mathbf{p} = \varepsilon_{bg} \oint \mathbf{r}' \sigma_p(\mathbf{r}') dS', \quad (2.17)$$

where ε_{bg} is the relative permittivity of the background medium and multiplied to the integral part in order to consider the charge screening of the dielectric background. Using the charge density σ_p in Equation 2.15, we can calculate the dipole moment using the surface currents.

2.5 Optical heating simulation using COMSOL

We simulated the electromagnetic heating of a nanoparticle using COMSOL Multiphysics 5.3 to estimate the temperature of the nanoparticle and its surroundings. We investigated two coupled phenomena: the electromagnetic response to external light and the heat transfer from a lossy particle to the surrounding medium.

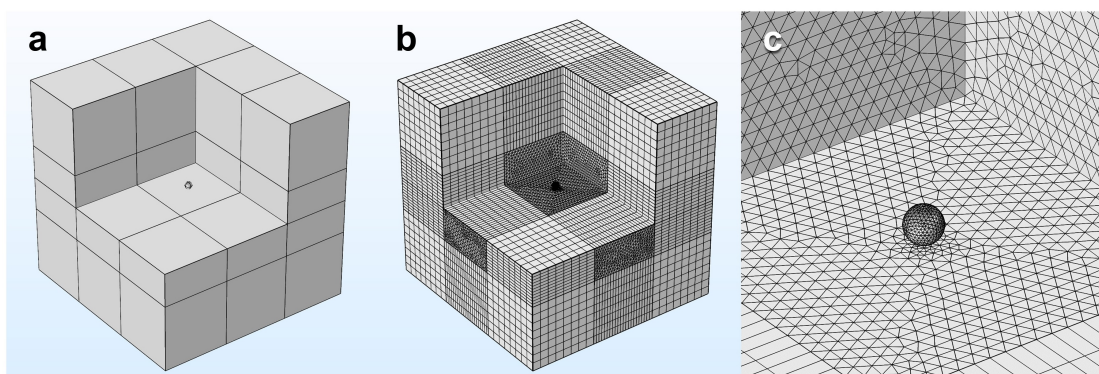


Figure 2.8 – Example geometry and mesh for optical heating simulation. **a**, Geometry including a particle, a substrate, and a superstrate. The outermost layer is the perfectly matched layer. A few domains are hidden in the illustration to reveal the particle geometry. **b**, Mesh for the geometry shown in **a**. **c**, Magnified view of the particle and its surrounding meshes.

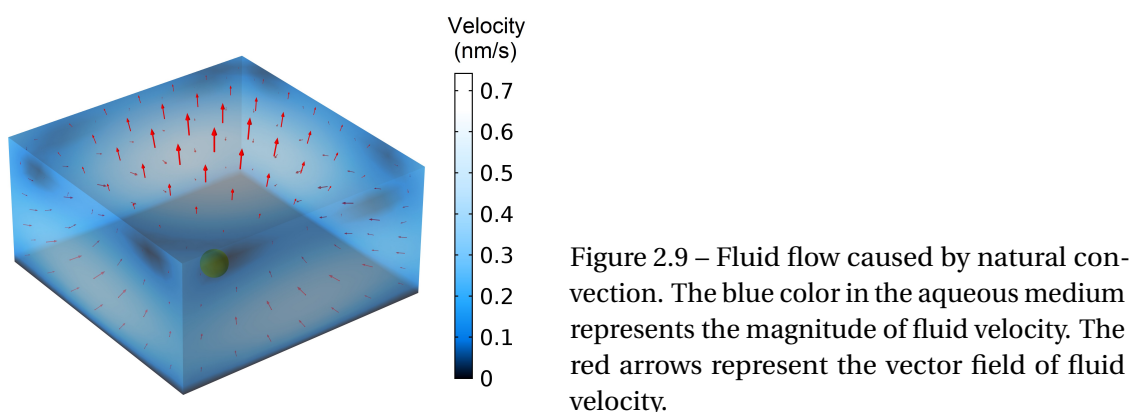


Figure 2.9 – Fluid flow caused by natural convection. The blue color in the aqueous medium represents the magnitude of fluid velocity. The red arrows represent the vector field of fluid velocity.

For the electromagnetic simulation, we used a wave optics module. The geometries for the aqueous medium and glass substrate were truncated by a cube with an edge length of $1.5\ \mu\text{m}$. We included a perfectly matched layer to represent an infinite region, whose thickness was set to be $1.5\ \mu\text{m}$. Figure 2.8 illustrates an example geometry and mesh of a $150\ \text{nm}$ particle located $10\ \text{nm}$ above the glass substrate. The losses obtained from the electromagnetic simulation were used as heat source in the subsequent heat transfer study.

For the heat transfer simulation, we used a heat transfer module and a laminar flow module. We modeled open boundaries by applying heat flux boundary conditions with heat transfer coefficients estimated from each material's thermal conductivity. The enhanced heat flux at the fluid boundaries due to convection was compensated using equivalent thermal conductivity for convection. In addition, we modeled the fluid flow for natural convection by coupling the heat transfer module with the laminar flow module. Figure 2.9 illustrates the natural convection of water around the nanoparticle shown in Figure 2.8.

Figure 2.10 shows the temperature distribution for the $150\ \text{nm}$ particle used as an example. A

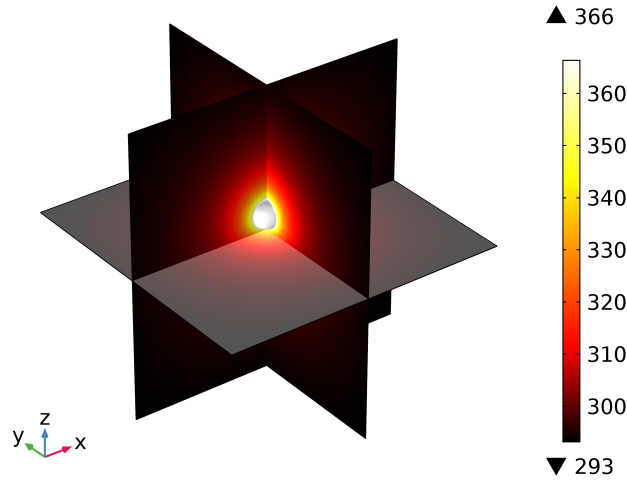


Figure 2.10 – Temperature distribution on the $x = 0$, $y = 0$, and $z = 0$ slices. The initial temperature was room temperature (293 K), and the maximum temperature on the particle surface was 366 K with a 73 K rise.

linearly polarized plane wave with a wavelength of 632.8 nm was normally incident from the top. The incident power intensity was estimated to be $6 \text{ mW}/\mu\text{m}^2$ based on the experimental conditions. The refractive index of gold was taken from the literature [111]. The refractive indices of water and glass were 1.33 and 1.5, respectively. The maximum temperature at the particle surface was calculated to be 366 K with a 73 K rise from the initial room temperature at the given power intensity. The water temperature near the particle was approximately 340 K.

The simulated time range was from 0 to 1 s in order to account for slow heat diffusion if it exists. We used a time step of 0.01 ms for the time range from 0 to 1 ms and 0.01 s for the rest of the time range. Temperature equilibrium was reached at 0.01 ms, which corresponds to the first time step. Water and glass have high thermal conductivity and can act as heat sinks, which may explain the rapid heat transfer. As the temporal resolution in this study is defined by the imaging framerate and is approximately 3 ms, we anticipate that thermal equilibrium has been reached while measuring particle motion.

3 The role of interfacial layers in trapped particle motion

A part of this chapter has been published in a peer-reviewed journal [112]:

Surfactants control optical trapping near a glass wall

Jeonghyeon Kim and Olivier J. F. Martin

Journal of Physical Chemistry C, 2022, 126, 1, 378–386

<https://doi.org/10.1021/acs.jpcc.1c08975>

3.1 Introduction

Among a variety of soft materials that constitute the environment of a colloidal particle in an aqueous medium, ionic surfactants play a fundamental role in colloidal suspensions. They develop charged layers on surfaces and prevent aggregation by providing electrostatic repulsion [113, 114]. Consequently, trapping experiments with colloidal nanoparticles inherently involve the effects of surfactants. In particular, these effects can have a substantial impact under nanoscale confinement, where the surface area to volume ratio increases significantly.

Despite their ubiquitous role in optical trapping, the many-sided effects of surfactants have not yet received significant consideration in trap characterization. It is only recently that surfactants have drawn researchers' attention, particularly, to their thermo-electric [115, 116] or thermophilic/thermophobic influences [117] on plasmonic optical traps. These studies reported the role of surfactants in optical trapping, but they also limited their discussions to surfactants in the bulk medium [115, 117]; the effects of surfactants on surfaces still remain elusive.

In this section, we describe the primary effect of surfactants on the optical traps, particularly at the vicinity of surfaces. For this, we analyze the motion of an optically trapped particle near a glass wall using video microscopy [118–120]. The effect of surfactants adsorbed on particle and glass surfaces can be indirectly characterized by analyzing the recorded particle motion.

In particular, due to the inherent inhomogeneity of glass and gold surfaces, we look into the statistical behaviors of analyzed particle motions while varying the surfactant conditions.

We construct the simplest possible environment, consisting of a surfactant solution at various concentrations and a glass chamber to contain fluids. We study cetyltrimethylammonium chloride (CTAC) as an example of cationic surfactant and a gold nanoparticle as an optical probe. The gold nanoparticles have unique optical properties, such as large scattering and absorption cross sections, making them outstanding imaging tracers [45, 121] and nanoscale thermal probes [90, 91, 122]. Along with the classical video analysis [118], we examine the zeta potentials of the gold nanoparticles as well as their hydrodynamic sizes, which change as a consequence of the surfactant structures adsorbed on the surfaces.

Based on these information, we propose a plausible model to explain the influence of the surfactants, particularly those at the interfaces, on the trapped particles' behaviors. We also hypothesize that the optical heating of the particles by the trapping laser can perturb the surfactant assemblies, which can act back on the particle's motion. Controlled experiments with polystyrene beads as a non-thermal probe are performed to support this interpretation.

3.2 Materials and methods

Materials

Cetyltrimethylammonium chloride (CTAC) was obtained from Sigma-Aldrich in solution (25 wt. % in H₂O). The CTAC solution was diluted with distilled water to reach desired concentrations. Gold nanoparticles with 150 nm diameter, stabilized suspension in citrate buffer, were purchased from Sigma-Aldrich. Polystyrene (PS) beads (210 nm diameter), which have carboxyl (-COOH) coatings and contain fluorophores (Flash Red, absorption maximum at 660 nm, emission at 690 nm), were purchased from Bangs Laboratories, Inc. The nanoparticle suspensions were prepared as described in the Methods section (Section 2.2.1).

Imaging and trapping

The gold nanoparticles and fluorescent polystyrene beads were trapped and imaged using the optical setup described in Section 2.2.2 and 2.2.3. An additional short pass filter with a 600 nm cut-off wavelength was included in the imaging path to cut the laser light scattered by the particles. The power of the He-Ne laser was controlled to be 10 mW before the entrance pupil of the trapping objective.

Particle tracking

The movement of a trapped particle parallel to the glass surface was recorded by a CMOS camera (CM3-U3-50S5C-CS, FLIR) at the framerate of 346 frames per second. Each measure-

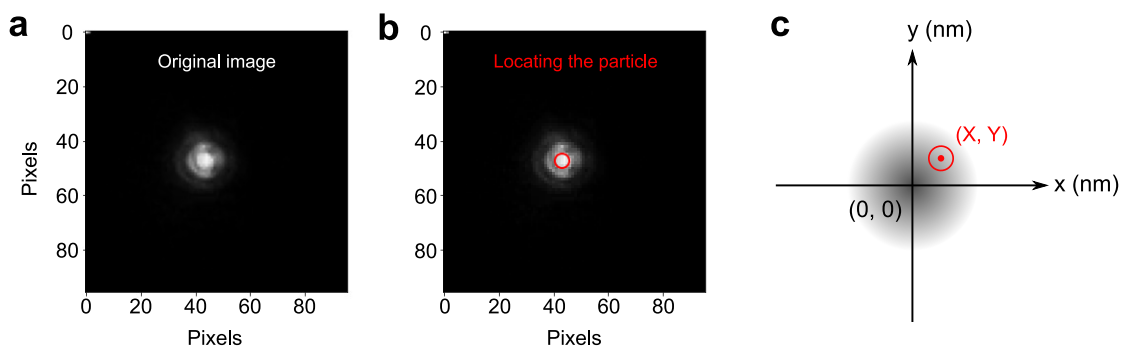


Figure 3.1 – Locating a particle from an optical image. (a) Example image of a trapped particle from a time-series image recording. (b) Particle position determined by a particle-tracing algorithm [118, 123] (the red circle). (c) Once the particle position (X, Y) is determined as in (b), the absolute position in the unit of pixels is converted to the relative position in the unit of nanometers (nm) with respect to the laser spot center (the origin). The laser spot center is assumed as the center of the position distributions.

ment recorded a sub-region of the CMOS sensor in size of 96×96 pixels. Figure 3.1a shows an example image from a recording.

The position of a particle was determined using a Python package, Trackpy [123], which uses the feature-finding and linking algorithms developed by Crocker & Grier [118]. Figure 3.1b shows the particle position determined by this algorithm for the example shown in Figure 3.1a. The position coordinates were originally in pixels. We determined the laser spot center as the center of the position distributions for each recording. Then the particle position was converted to the relative position to the laser spot center in the unit of nanometers (Figure 3.1c).

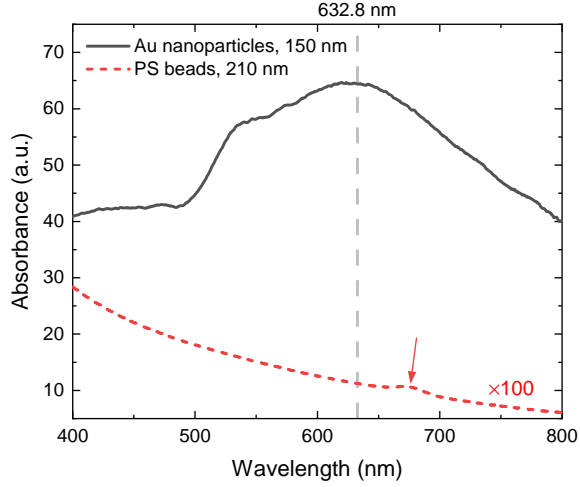
All trajectories for trapped particles were collected for at least 20 seconds (10 seconds for PS beads due to relatively weak axial trapping stiffness), which corresponds to ~ 7000 frames. The temporal and spatial resolutions of a trajectory were respectively determined by the camera frame rate ($1/346 \approx 3$ ms) and the camera pixel size divided by the image magnification ($3450/60 = 57.5$ nm/pixel). We provide an open access dataset for the particle recordings and the corresponding trajectories and MSD analysis in Ref. [124].

3.3 Results and discussion

3.3.1 Mean squared displacement (MSD)

We examined an optically trapped particle's statistical behavior as a function of CTAC concentration by analyzing its mean squared displacement (MSD). The MSD is a measure of the distance traveled by a random walker over a time interval τ (also called a time lag). It is the most common measure of the spatial extent of a random motion, and it can be thought of as

Figure 3.2 – UV-vis absorbance spectra for 150 nm gold colloids and 210 nm polystyrene (PS) beads used in this study. The absorbance magnitude for each spectrum was adjusted according to the corresponding particle concentration. The spectrum for PS beads was multiplied by 100 times afterward for legibility. The maximum absorbance peak for gold colloids is close to the trapping laser wavelength of 632.8 nm (He-Ne laser). The PS beads have a small fluorescence emission peak of around 690 nm (red arrow).



an area explored by the particle for a given time. Mathematically, the MSD at a time lag τ is defined as:

$$\text{MSD}(\tau) \equiv \langle [x(t + \tau) - x(t)]^2 \rangle, \quad (3.1)$$

where the angled bracket $\langle \dots \rangle$ denotes time average, and $x(t)$ is the position of the particle as a function of time t , *i.e.*, the particle trajectory.

The optically trapped particle is modeled as a damped harmonic oscillator in a heat bath [125]. To keep a constant temperature, we fixed the size and material of the particles (gold and 150 nm in diameter) and the incident laser power (10 mW before the trapping objective). These three parameters determine the amount of optical heating by the laser [126, 127]. Figure 3.2 shows the measured absorbance spectrum of the 150 nm gold colloid; this particular colloid was carefully chosen to have its highest absorbance at the trapping laser's wavelength so that it not only acts as an optical probe but also serves as a localized heat source.

Based on the constant temperature assumption, we can describe the motion of a damped harmonic oscillator in one dimension with the Langevin equation [128]:

$$m\ddot{x}(t) + \gamma\dot{x}(t) + \kappa x(t) = F_{\text{therm}}(t), \quad (3.2)$$

where m is its inertial mass, γ is its friction (drag) coefficient, κ is the spring constant of the optical trap, and F_{therm} is the random thermal force acting on the trapped particle. On the timescales longer than a few microseconds, the inertial term, $m\ddot{x}(t)$, becomes negligible in aqueous media due to the low Reynolds number [129]. The reduced Langevin equation without the inertial term can be solved for MSD [125], which is

$$\text{MSD}(\tau) = \frac{2k_B T}{\kappa} (1 - e^{-\tau\kappa/\gamma}), \quad (3.3)$$

where k_B is the Boltzmann constant and T the temperature.

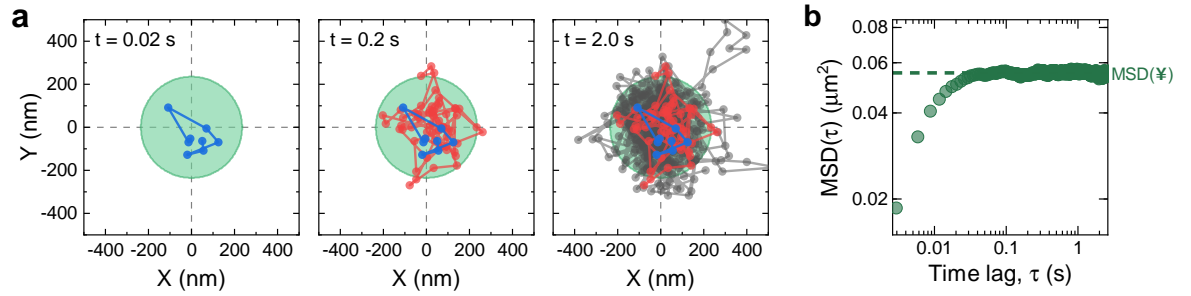


Figure 3.3 – Particle trajectory in an optical trap and its mean squared displacement (MSD). **a**, Example trajectories of a trapped particle at three different timescales (0.1 mM CTAC). The green circle has an area same as the $\text{MSD}(\tau \rightarrow \infty)$, which indicates the area over which the particle is confined over a long time scale. **b**, Double-logarithmic plot of the MSD calculated from the trajectory shown in **a**. The value of $\text{MSD}(\tau \rightarrow \infty)$ is indicated as the dashed horizontal line.

Figure 3.3a shows an example of three successive trajectories for an optically trapped gold nanoparticle at different timescales. It visualizes the temporal evolution of the two-dimensional position fluctuations, $(X(t), Y(t))$, at increasing time intervals (0.02, 0.2, and 2.0 seconds). Figure 3.3b shows the MSD calculated from this trajectory. When the time lag τ becomes long enough, typically longer than 0.1 seconds in our experiments, the MSD reaches a plateau; we call it $\text{MSD}(\tau \rightarrow \infty)$ or simply $\text{MSD}(\infty)$, which is closely related to the area in which the particle's motion is confined by the restoring optical force. This area is shown as a green circle in Figure 3.3a. Equation 3.3 tells us that among the three variables that determine the $\text{MSD}(\tau)$, only the temperature T and the trapping stiffness κ decide the value of $\text{MSD}(\tau \rightarrow \infty)$, not the friction coefficient γ ; the value of γ affects the slope of the linear dependence on τ at short time scales (Figure 3.3b).

3.3.2 Statistical distribution of MSD

We have analyzed at least 30 trajectories for each concentration to obtain a distribution of $\text{MSD}(\tau \rightarrow \infty)$. An example distribution at 0.1 mM CTAC is plotted as a histogram in Figure 3.4a, which consists of 66 measurements. Interestingly, it reveals that the dataset has a skewed distribution rather than a symmetric one. One possible explanation for this is the particle size distribution, which is well-known to follow the log-normal distribution. Figure 3.5a shows the measured size distribution of the colloids used in this study, which is also well approximated with a log-normal. The relationship between the size distribution and that of $\text{MSD}(\infty)$ can be inferred from Equation 3.3, where $\text{MSD}(\tau)$ converges to $\frac{2k_B T}{\kappa}$ with $\tau \rightarrow \infty$. Since the trapping laser power was fixed for all the measurements, the stiffness κ can be assumed constant. Only the temperature T may vary with the size variance, as does the absorption by the particle. Figure 3.5b shows the Mie calculation for the absorption cross-section with increasing particle size; a larger particle tends to have a larger absorption cross-section, raise the temperature T , and therefore have a greater value for $\text{MSD}(\infty)$.

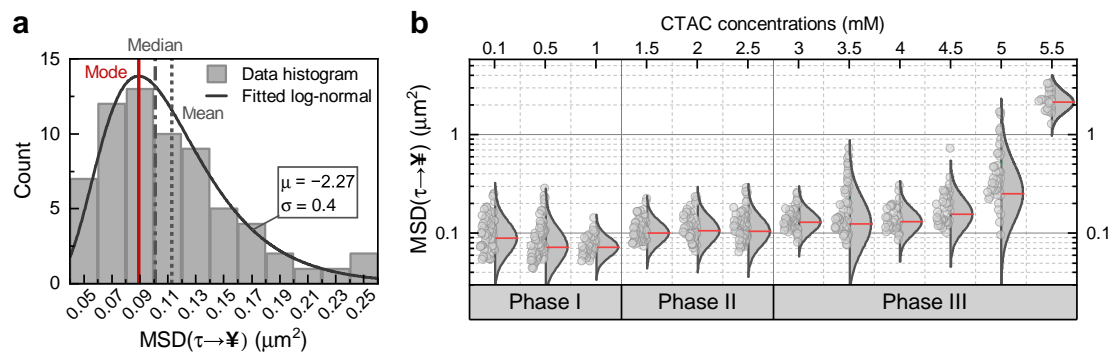


Figure 3.4 – Statistical distribution of MSDs for different surfactant concentrations. **a**, A typical example MSD($\tau \rightarrow \infty$) histogram for a total of 66 measurements at 0.1 mM CTAC. A log-normal distribution is fitted to the histogram to approximate the skewed data distribution and calculate the statistical population's mode. **b**, Semi-logarithmic plot summarizing all the MSD(∞) as a function of bulk CTAC concentration. For each concentration, at least 30 trajectories are analyzed for the log-normal distribution fit. The red solid bars represent the mode values of each distribution.

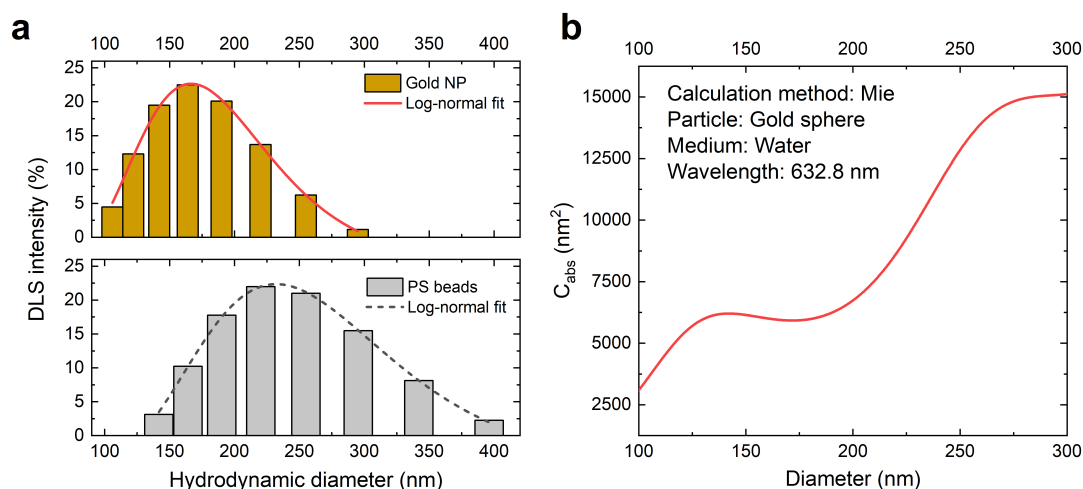


Figure 3.5 – Sizes distribution for gold and PS colloids and Mie absorption cross-section for gold nanoparticles. **a**, Hydrodynamic size distribution measured by dynamic light scattering (DLS) and its log-normal fit for gold (upper) and PS (lower) colloids. **b**, Absorption cross-section calculated from Mie theory for gold nanoparticles. The program MiePlot (<http://www.philiplaven.com/mieplot.htm>) was used for calculations. The particle is assumed as a gold sphere and the medium as water. The wavelength is set to be the wavelength of the trapping laser, 632.8 nm.

Such an asymmetric distribution appears for all the examined CTAC concentrations. We made a total of 651 measurements, *i.e.*, 55 measurements on average for each concentration. We fitted each dataset with a log-normal to observe the underlying trends for varying surfactant concentrations. The mode of the dataset was also calculated from the log-normal fit as a statistical representative value (*e.g.* the red solid vertical line in Figure 3.4a). Figure 3.4b summarizes the results as a function of CTAC concentration. For each concentration, the data points are drawn on the left half and the log-normal fit on the right half with the mode highlighted as the red horizontal bar. These mode values reveal that the different amount of surfactants can strengthen or weaken the optical trap. We grouped the results into three categories (Phase I, II, and III) based on the trends discovered by the mode values. We will elaborate on each category and a plausible role of the surfactant in Section 3.3.4. Before going into the details, we will first describe the surfactant adsorption behaviors at the solid-aqueous interfaces in our system.

3.3.3 Surfactant adsorption

CTAC surfactants adsorb on the glass and gold nanoparticle surfaces [130–132]. On the glass surface, they form centrosymmetric aggregates, termed admicelles, which resemble micelles in the bulk solution [133, 134]. The formation of admicelles appears early in the adsorption process, at concentrations below the bulk critical micellar concentration (CMC) [133, 134]. Tyrode *et al.* [134] performed a detailed study on the adsorption of cetyltrimethylammonium bromide (CTAB, the corresponding bromide salt of CTAC) on silica, and we refer to this paper for a detailed description of the adsorption process.

On the other hand, CTA^+ molecules form a bilayer structure on the gold surfaces [130]. A recent study by Li *et al.* [135] proposed an insightful mechanism for the assembly structure of CTA^+ molecules on citrate-capped gold colloids, which varies not only with CTAB concentration but also with the ratio of CTAB molecules to gold nanoparticles.

We adapted these two studies by Tyrode *et al.* [134] and Li *et al.* [135] to understand how the CTA^+ molecules adsorb and form assemblies on the different interfaces in our trapping system. (Although they studied CTAB instead of CTAC, both surfactants have cetyltrimethylammonium cations (CTA^+) in common, and we assume that the effect of the halide counterions (Br^- or Cl^-) is not significant in this study where we consider the low concentration range at which both of CTAB and CTAC form similar aggregates [136].) We will determine the CMC, the particles' zeta (ζ) potentials, and their hydrodynamic sizes, with which we provide plausible surfactant structures at the interfaces as a function of concentration.

Critical micelle concentration (CMC)

We first measured the conductivity of the gold colloid-surfactant solution as a function of CTAC concentration to determine the CMC in bulk. The CMC was determined as 1.4 mM by finding

the intersection of two straight lines that were fitted into the conductivity/concentration data above and below the CMC [137, 138] (Figure 3.6a). This value of 1.4 mM is higher than the values reported in the literature (1.0 to 1.1 mM) [132, 139] possibly due to two factors: First, the bulk solution is a mixture of surfactants, gold nanoparticles, and water; the surfactants adsorb on the particles' surfaces, which effectively reduces the bulk concentration and thus shift the apparent CMC to a slightly higher value. The second factor is related to the solution preparation step. We prepared the colloid and surfactant mixture by centrifuging the gold colloids, carefully removing the supernatant, and re-dispersing the residue in the target CTAC solution. Since we cannot completely remove the supernatant, about 5 % of the original buffer remains in the residue and dilutes the surfactant concentration. For these reasons, we found a slightly higher value for the CMC of the colloid-surfactant mixture, which will be used as the value for CMC throughout the discussion.

Figure 3.6b and c show the hydrodynamic size and ζ potential of the gold colloids, which change as a function of CTAC concentration. When combined, these different measurements give valuable information about the surfactant structures on the particles' surfaces.

Adsorption behaviors below CMC

According to the study by Li *et al.* [135], the CTA^+ cations form assembly structures on colloidal surfaces in the following order: incomplete monolayer \rightarrow complete monolayer \rightarrow imperfect bilayer \rightarrow perfect bilayer \rightarrow (perfect bilayer + micelles). The hydrodynamic size (171 nm) and ζ potential (39 mV) at the lowest CTAC concentration in Figure 3.6b and c imply that the surfactant molecules form at least imperfect bilayer structures on gold nanoparticle surfaces, whose charge was originally negative due to the citrate ions and became positive with the adsorption of the positively charged CTA^+ cations. If the particles had not reached the imperfect bilayer state, remaining either in the state of the incomplete monolayer or complete

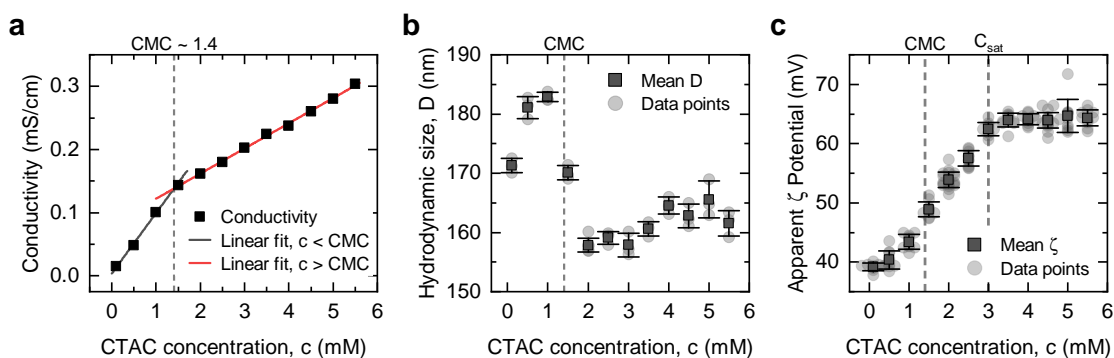


Figure 3.6 – Critical micelle concentration (CMC) and colloid characteristics. **a**, Conductivity of the bulk nanoparticle-surfactant solution and its piecewise linear fit to determine the CMC. **b**, Hydrodynamic size and **c**, zeta (ζ) potential of the colloidal gold nanoparticles as a function of CTAC concentration.

monolayer (*i.e.*, the hydrocarbon tail groups of the CTA⁺ molecules exposed to the bulk solution), they would have aggregated due to the hydrophobic effect among particles [135]. Since the size distribution shows a unimodal distribution with an average size of 171 nm (Figure 3.5a), it indicates no aggregate, and the CTA⁺ cations must form at least an imperfect bilayer assembly. These imperfect bilayers develop into perfect bilayers with increasing CTAC concentration, supported by the growing hydrodynamic size and ζ potential up to the CMC.

The glass-water interface also experiences a drastic change from the lowest concentration up to the CMC [134]. In this region, the surface coverage with admicelles rapidly increases and reaches its maximum above the CMC [134]. This type of adsorption behavior has been reported in the literature for various surfactant-substrate combinations [133, 134, 140] and also extensively reviewed by Atkin *et al.* [132]. Therefore, we assume that this general adsorption model also works for our glass-CTAC solution system.

3.3.4 Effect of adsorbed surfactants at different concentration ranges

Combining the observation for the gold nanoparticles and the assumption for the glass-solution interface in the concentration range below the CMC, we can expect increasing electrostatic repulsion between the particle and the surface with the gradual adsorption of CTA⁺ molecules on both surfaces. This repulsive force can elevate the equilibrium position of the particle above the surface and thus can decrease the hydrodynamic drag [141] following Faxén's law [142]. Such a change in particles' position can be one of the reasons for the changes in particle motion inside the optical trap.

Equilibrium position of a trapped particle

To test this idea of the particle's vertical position and its hydrodynamic drag, we calculated the drag coefficient γ by fitting the measured MSDs with Equation 3.3. By introducing Einstein's relation $D = k_B T / \gamma$ and substituting $\gamma / \kappa = \tau_c$, Equation 3.3 becomes

$$\text{MSD}(\tau) = D\tau_c(1 - e^{-\tau/\tau_c}). \quad (3.3a)$$

We have estimated these two variables, D and τ_c , by fitting the MSD curves from measured data with 3.3a. From the values of D and τ_c , we can infer the drag coefficient $\gamma = \frac{k_B T}{D}$ and the stiffness $\kappa = \frac{k_B T}{D\tau_c}$ if the temperature T is known.

Since we do not know the exact temperature of the particle, we estimated the temperature from a simulation as described in Section 2.5. The maximum temperature at the particle surface was estimated as 366 K with an estimated 73 K rise from the initial room temperature at the given power intensity of 6 mW/ μm^2 (Figure 3.7). Although the actual temperatures for different particles may vary (since different sizes have different absorption cross-sections as shown in Figure 3.5b), we assumed a constant temperature of 366 K to see the trend of the drag coefficient as a function of CTAC concentration.

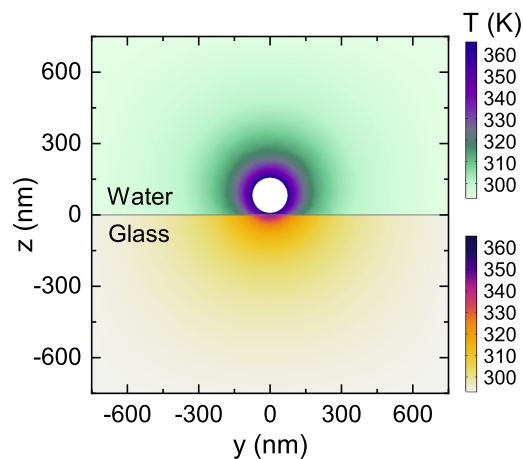


Figure 3.7 – Cross-sectional temperature distribution around the particle.

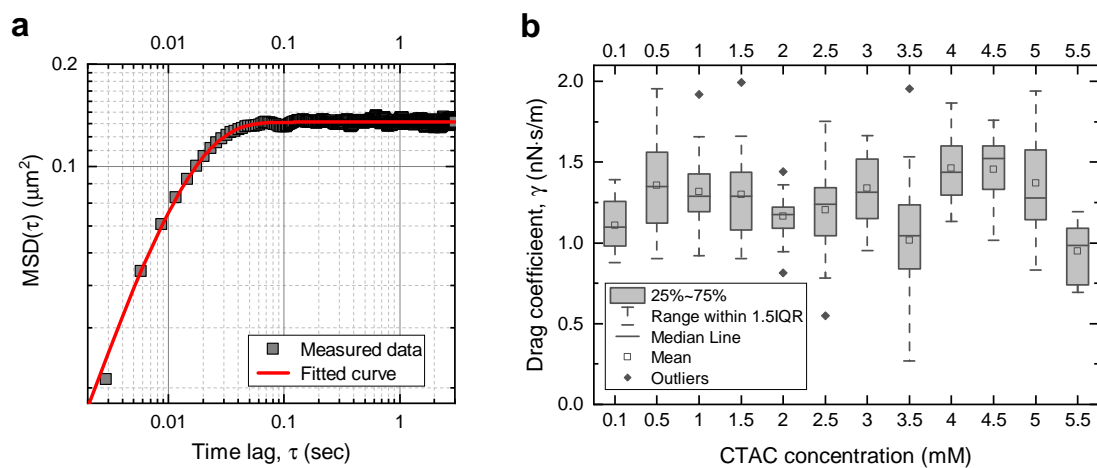


Figure 3.8 – Hydrodynamic drags estimated from MSD data fitting. **a**, An example MSD data fitted with the solution of MSD (Equation 3) in the least-squares sense. The trapping stiffness κ and the drag coefficient γ were estimated with the assumption of a constant temperature T (366 K). **b**, Box chart of drag coefficients γ as a function of CTAC concentration. datasets showing poor curve fitting were excluded in the chart.

Figure 3.8 summarizes the results. An example fitted curve to a dataset is displayed in Figure 3.8a. The values for D and τ_c were estimated in the least-squares sense. We also found that not all datasets agree with the solution for the Langevin equation; about half ($46 \pm 15\%$) of the datasets deviates from Equation 3.3a, showing poor function fitting. We guess that additional forces acting on the particle motion, such as thermophoretic forces, which are not considered in the original Langevin equation, could be a possible reason for the deviation. We excluded the poorly fitted results and analyzed those showing good theoretical matches in Figure 3.8b.

Figure 3.8b clearly illustrates that the drag coefficients remain at similar levels, independent of CTAC concentration. They do not show any close correlation with the ζ potentials of the particles, nor with the surface coverage of the glass substrate. This result is counter-intuitive as we expect that the particle's vertical position is determined by the balance between the radiation pressure of the laser beam and the electrostatic repulsion between the two charged surfaces, and the surface charge (and thus the repulsion potential) increases with concentration. A possible scenario is that the surfactant molecules adsorbed at the contact area migrate outside of this region due to the electrostatic repulsion. This explains why the particle height is not determined by the overall concentration. Therefore, we can assume that the particle's axial position remains similar across the whole concentration range used in this study.

Phase I: Low concentration range below CMC

With this understanding, we construct a model for the lowest concentration range below the CMC to interpret the trapped particles' behaviors in Phase I (Figure 3.4b). In Phase I, the mode of the $\text{MSD}(\infty)$ distribution decreases, and the distribution itself is narrowing. Since $\text{MSD}(\tau \rightarrow \infty) = \frac{2k_B T}{\kappa}$ from Equation 3.3, the decrease in $\text{MSD}(\infty)$ implies an increase in the trapping stiffness κ under the assumption of a constant average temperature. Based on the idea that the particle surface has an incomplete bilayer and the glass surface has yet to be fully covered below the CMC, we can hypothesize that these molecules are partly mobile, and they can rearrange themselves when the particle sits on the glass wall. This rearrangement then forms an additional lateral trapping potential, and the particle's $\text{MSD}(\infty)$ decreases as a consequence. This decreasing trend for the $\text{MSD}(\infty)$ can be understood by the fact that denser admicelles result in a deeper and narrower potential well.

Two driving forces can be proposed for the mobility and rearrangement: 1) the electrostatic repulsion between the particle and the surface admicelles; and 2) the increased temperature around the particle by laser heating [91, 143]. In general, admicelles are mobile, and they can migrate over the surface without leaving the surface completely, which requires much less energy than desorption [144]. Around the optically trapped and heated nanoparticle, there is sufficient energy for the admicelles to diffuse over the surface since the local temperature of an optically trapped gold nanoparticle can easily reach up to 100 °C even at moderate laser powers [126, 127]. The electrostatic repulsion can drive the micelles away from where the particle rests.

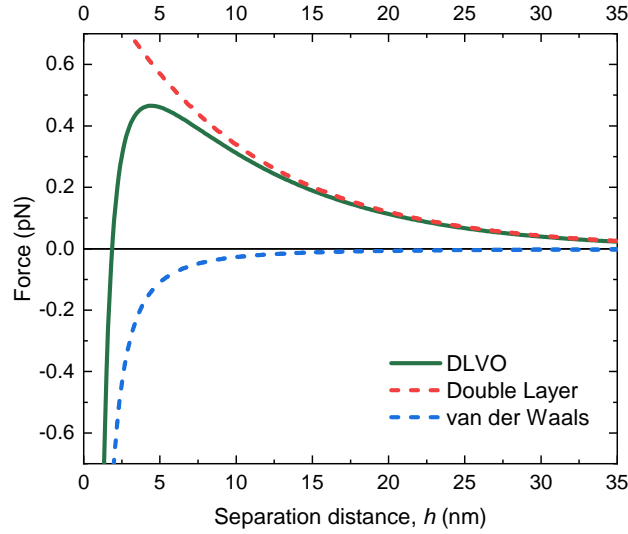


Figure 3.9 – Interaction force between the gold nanoparticle and the admicelle on the glass wall as a function of separation distance.

Once being settled around the trapped particle, these micelles can form an additional trapping potential [145], as we hypothesized based on the observed decreasing trend in $\text{MSD}(\infty)$ in Phase I. First, we estimated the magnitude of the interaction force between the particle and the micelle with the DLVO theory (Figure 3.9 and Appendix A for more details). The maximum magnitude of the repulsive force was ~ 0.46 pN, and it decreased exponentially with separation distance, h . For instance, at $h = 30$ nm, the force is repulsive and has a magnitude of 0.04 pN; a fraction of this force (i.e., a projection onto the lateral surface) contributes to the particle trapping.

On the other hand, the optical force induced by the trapping laser also falls into similar magnitudes. The trapping stiffness of the optical trap at 0.1 mM CTAC (where the effects from admicelles are assumed to be minimal) is calculated as 1.13×10^{-7} N/m, using Equation 3.3 with an estimated temperature of 366 K (Section 2.5 for more details). At around 170 nm displacement from the trap center, same as the radius of the $\text{MSD}(\infty)$ shown in Figure 3.4a, the force is estimated as 0.02 pN towards to trap center. The similarities in force magnitudes between optical tweezer and admicelle/particle interaction imply that the electrostatic interaction between the admicelle and the particle is significant enough to influence the optical trap and thus the particle motion.

Phase II: Intermediate concentration range above CMC

In the next phase of the $\text{MSD}(\infty)$, Phase II in Figure 3.4b, the distribution and its mode show a step-like increase above the CMC and then stagnate up to 2.5 mM. This transition should also be related to the change in the surfactant structure. Returning to Figure 3.6b, we find

an abrupt decrease in the hydrodynamic size at 1.5 mM. Such an abrupt change indicates the involvement of a new species, which has a higher electrical charge than that of a single CTA⁺ molecule and thus more efficiently screens the particle's surface charge, making the electrical double layer thinner: the advent of micelles. The plummeting hydrodynamic size and the steeper rise in the ζ potential in Figure 3.6b and c substantiate together the existence of micelles in the particles' outer layers. Therefore, we estimate that the bilayer on the particle surface is almost complete at the end of Phase I, and the micelles in the bulk start to become associated with the particle at the beginning of Phase II.

These micelles at the particle-liquid interface apparently do not affect the $\text{MSD}(\infty)$ as its distribution stagnates throughout the three concentrations in Phase II. A plausible explanation is that these micelles are mobile around the particle and rearrange themselves, similar to the previous assumption in Phase I. The step-like increase in the $\text{MSD}(\infty)$ can be explained by the fully occupied glass-liquid interface above the CMC. The admicelles are now closely packed and have lost their mobility. The previously mentioned effect of additional trapping potential created by the re-arranged admicelles will disappear, which will raise the $\text{MSD}(\infty)$ values.

Phase III: High concentration range above surface saturation concentration

The final concentration region, Phase III in Figure 3.4b, features another step-like increase and exponential growth of $\text{MSD}(\infty)$. The second jump between 2.5 and 3 mM can be attributed to the complete saturation of the particle surface with micelles, similar to the first jump associated with the full coverage of the glass substrate. The plateau of the ζ potentials in Figure 3.6c supports the saturated adsorption on the particle surface. Since both the glass and particle surfaces are fully saturated at this stage, the adsorbed structures on the interfaces remain the same. The only variation with the increased concentration is the number of micelles in the bulk solution. The exponential growth in the $\text{MSD}(\infty)$ in Phase III indicates that the bulk micelles disturb stable trapping, and video investigations also show impeded particle movements.

A recent study by Jiang *et al.* [117] provides a convincing explanation of this phenomenon. They studied the role of surfactants in plasmonic trapping and described that the surfactants in bulk could alter a trapped object's thermal response, making it thermophilic or thermophobic depending on the type of surfactants. Another study by Lin *et al.* [115] also reported a similar effect based on a non-uniform surfactant distribution in bulk upon a temperature gradient. In particular, they discovered that CTAC makes gold nanoparticles thermophilic driven by a surfactant-induced thermo-electric field, which enhanced the trapping stiffness of their thermo-plasmonic trap 2 – 3 orders of magnitude higher than that of optical tweezers [115]. However, in our system, the heat source is the trapped particle itself, whose position constantly fluctuates, and so does the concomitant temperature gradient. Therefore, even if the CTAC makes the gold nanoparticle thermophilic, the self-induced thermo-electric field can disturb the optical trap.

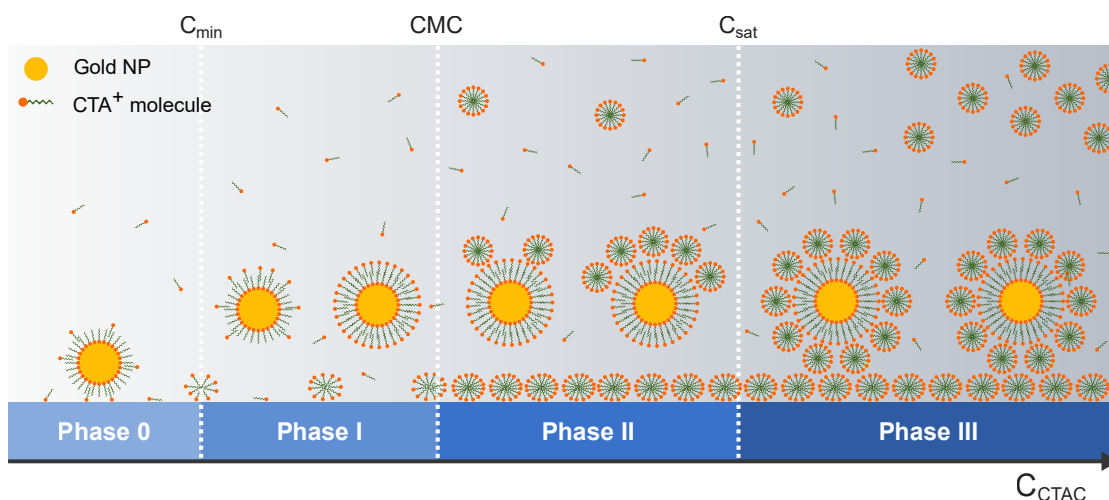


Figure 3.10 – Cartoon showing plausible morphologies of adsorbed surfactant cations, CTA^+ , at the glass-water interface and the gold nanoparticles' surfaces at varying CTAC concentrations from low (left) to high (right). Adapted from Li *et al.* [135] for gold colloid surfaces and Tyrode *et al.* [134] for glass-water interface.

Summary of Phase I, II, and III

Figure 3.10 summarizes plausible morphologies of adsorbed surfactant molecules on the glass substrate and gold colloids, at increasing CTAC concentrations. It depicts gradual changes in the surface coverage as well as the likely surfactant assemblies on different interfaces, adapted from Li *et al.* [135] and Tyrode *et al.* [134]. Below the lowest concentration (C_{min}), the particle is electrostatically attracted and stuck on the negatively-charged glass surface (Phase 0). For stable colloids, a minimum concentration of 0.1 mM was required in this study. From C_{min} to CMC (Phase I), the particle trapped close to the glass wall may rearrange the admicelles, inducing a self-constraint on its movement and thus exhibiting the most stable trapping among the examined concentration groups. From CMC up to C_{sat} (Phase II), the particle is stably trapped on the fully covered glass surface, where the effect of the admicelles vanishes. At this stage, the particle surface has not yet been saturated. Above C_{sat} (Phase III), all the interfaces are completely saturated, and the particle starts to be impeded from finding a stable trap position, possibly due to the effect of the surfactants in the bulk [115, 117].

3.3.5 Comparison with non-thermal probes

We explained the motion of the trapped gold nanoparticles based on the surfactant assembly structures that develop with increasing surfactant concentration (admicelles, bilayers, and micelles in the bulk) and the possible influence of the particle on these structures. One of the hypotheses was the thermal effect of the optically trapped gold nanoparticles, which causes the local rearrangement of admicelles at the glass-solution interface. To test this hypothesis, we performed trapping experiments with polystyrene (PS) beads, which absorb much less

light and thus produce much less heat (Figure 3.2 for the absorbance spectrum for gold and PS nanoparticles).

Properties of polystyrene (PS) beads

We used PS beads that have carboxyl groups on their surfaces, making them negatively charged (-41.5 ± 0.5 mV) like the gold nanoparticles with citrate coatings (-27.2 ± 0.2 mV). Figure 3.11a and b show their ζ potentials and hydrodynamic sizes as a function of CTAC concentration, superimposed on the gold nanoparticle data for comparison. The initially negative surface charge became immediately positive with the addition of CTA^+ molecules, and their ζ potential magnitudes changed almost identically to those of gold nanoparticles with increasing CTAC concentration (Figure 3.11a). The development of their hydrodynamic size also resembles those of gold nanoparticles with about 70 nm offset (Figure 3.11b). The similar behaviors in the surface charges and the stark contrast in the optical absorbance make the PS beads a successful candidate to test the thermal effects.

MSD analysis for PS beads

Figure 3.11c summarizes the MSD analysis for the PS beads, with the results for gold nanoparticles for comparison. The beads were trapped by the same optical tweezer at four different CTAC concentrations (0.1, 1, 2.5, and 5 mM). By comparing the results from this non-thermal probe, we discovered a few interesting differences. First, the distributions remain similar across vastly different concentrations, supporting our hypothesis that the changes originate from the thermal effects. Furthermore, the distributions for the PS beads are narrower and symmetrical. We have previously explained the gold nanoparticles' skewed distribution by combining the asymmetric size distribution and the size-dependent optical heating. The PS beads also have an asymmetric log-normal size distribution with a comparable variance (Figure 3.5a), but the optical heating effects are absent in this case. Therefore, we can understand that the optical heating makes the distribution skewed and broader for gold nanoparticles. The remaining variance in the $\text{MSD}(\infty)$ distribution for the PS beads can be attributed to other experimental variations such as the surface charges and shapes of the particles and site-specific local surface variations. The only exception occurs at 1.0 mM CTAC, where the gold nanoparticles have a narrower yet skewed distribution. As we suggested earlier, it may be explained by the interactions with the admicelles, which disrupt the distribution of admicelles and reduce their randomness through rearrangement.

Figure 3.11d reveals the different developments of the $\text{MSD}(\infty)$ for the gold and PS nanoparticles. The points and error bars respectively represent the modes and interquartile ranges (25–75 %) of the data. The modes of the PS beads remain similar, as expected from Figure 3.11c, showing neither the decrease in Phase I nor the increase in Phase III that are observed for the gold nanoparticles. The overall shifts of the MSDs to higher values for the PS beads can be attributed to weak axial confinement due to their relatively small scattering force compared to

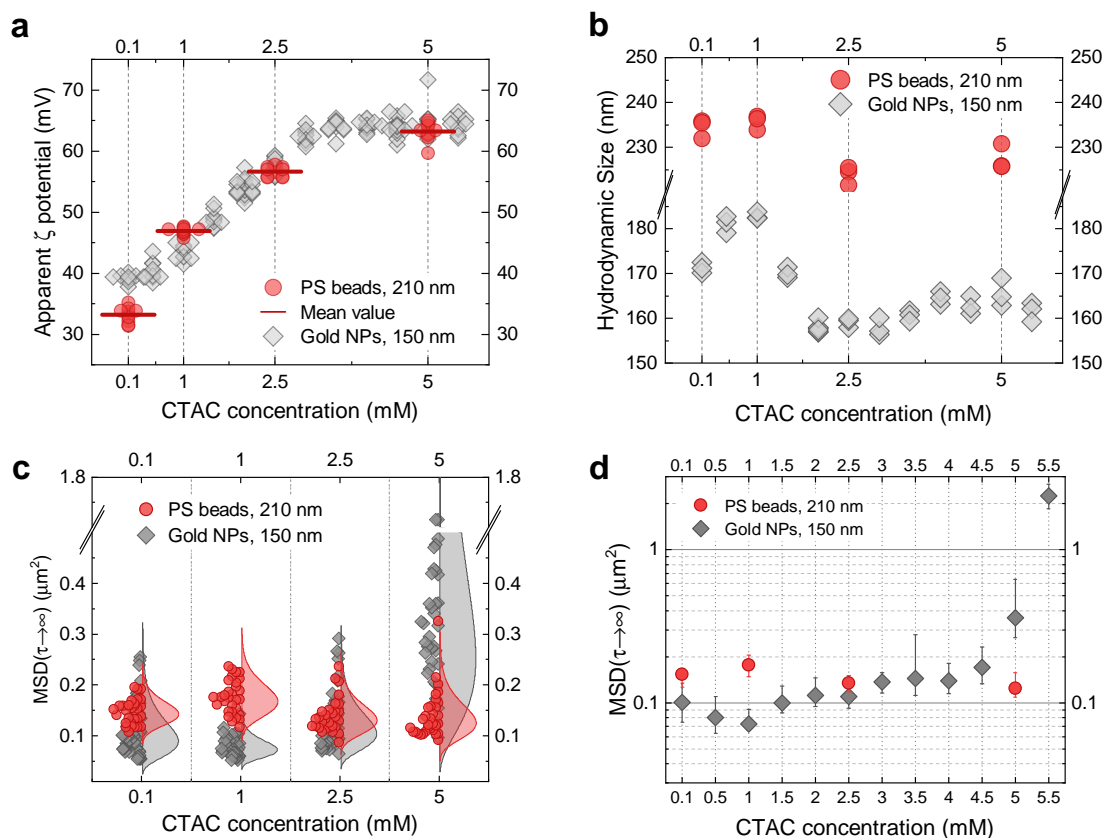


Figure 3.11 – Polystyrene (PS) beads as a non-thermal probe. **a**, Zeta potential and **b**, hydrodynamic size of the PS beads compared with those of gold nanoparticles as a function of CTAC concentration. Each data point represents an average of 10 measurements. For each concentration, 10 data points are displayed for the ζ potential, and 3 data points for the hydrodynamic size. **c**, Distributions of $MSD(\infty)$ for optically trapped PS beads near the glass wall. The left half shows the data points of at least 30 measurements, and the right half shows the fitted log-normal distribution. The data and its distribution for gold nanoparticles are plotted behind for comparison. **d**, Comparison of the $MSD(\infty)$ between gold and PS nanoparticles for the whole concentration range in a semi-logarithmic scale. The data points represent the mode of each distribution. The error bars indicate (25%, 75%) interquartile range.

that of the highly reflective gold nanoparticles. Since the ζ potential of the PS beads and the surface coverage of the glass substrate drastically change over the examined concentration range, the adsorption of surfactant molecules seems to have negligible effects on the motion of the PS particles. It also appears that the micelles in bulk do not perturb the trap from the results at 5.0 mM CTAC. Therefore, the observations with the PS beads support the two hypotheses regarding the thermal effects of the gold nanoparticles on their motions, namely the heat-induced migration of the adsorbed micelles on the glass surface at low concentrations and the disturbance caused by the bulk micelles in the presence of a temperature gradient at high concentrations.

3.4 Conclusion

This chapter has studied the effect of adsorbed surfactants (CTAC) on an optically trapped gold nanoparticle by analyzing its trajectories inside the trap. Close to the liquid-glass interface, the particle interacts with the surfactants in a way that strengthens or inversely disturbs stable trapping, depending on the surfactant concentration. Below the CMC, we have evidenced that the unsaturated surfactant layer can create an additional trapping potential. The interaction between the surfactant admicelles and the optical heated metallic particle has been suggested as a possible mechanism, which was supported by theoretical modeling using the DLVO theory and controlled experiments with cooler PS beads. Above the concentration at which both the particle and glass surfaces are fully saturated, we have found that micelles in bulk perturb the optical trap, analogous to the recent findings by Lin *et al.* [115] Our findings develop a fundamental understanding of the influence of surfactants on optically trapped objects, where surfactants are often required for colloidal stability. The same methodology can be applied to different combinations of surfactants, colloidal particles, and substrates. Moreover, a gold nanoparticle as a thermal probe can become a versatile tool in surface sciences to locally elevate the temperature around the particle and simultaneously investigate temperature-related phenomena such as desorption or polymerization, by statistically analyzing its motion.

4 Probing molecular interactions with trapped nanoparticle motion analysis

A part of this chapter has been published in a peer-reviewed journal [146]:

Probing surfactant bilayer interactions by tracking optically trapped single nanoparticles

Jeonghyeon Kim and Olivier J. F. Martin

Advanced Materials Interfaces, 2022, 2201793

<https://doi.org/10.1002/admi.202201793>

4.1 Introduction

As we have seen in the previous chapter, the motion of a microscopic particle suspended in a medium provides information about its interactions with its surroundings [28, 147]. The observation of individual trajectories, known as single-particle tracking (SPT), has established itself as a powerful tool to study molecular processes and interactions, especially in biological systems [28, 30–33]. SPT also holds great promise for studying nanoscale chemical and physical processes [24, 40, 148, 149], and novel applications of SPT are still actively emerging [30].

The utilization of optical tweezers in SPT experiments brings important advantages in giving a tracer particle pinpoint access to an area of interest and providing controlled forces to facilitate observation. After their initial and major applications in biophysics [35, 36, 150], optical tweezers and SPT are being increasingly implemented together in physics such as microrheology [37] and hydrodynamics [23]. Franosch et al. [24], for instance, studied the Brownian motion of an optically trapped bead in water and revealed that surrounding water molecules act back on the particle once disturbed by the particle's thermal motion. In particular, the optical tweezer played a crucial role in their discovery of such weak interactions by providing controlled forces and thus facilitating the characterization of the particle motion.

Unlike these successful demonstrations in biophysics and physics, the combination of optical tweezers and SPT has not yet actively emerged in chemistry and surface science. The SPT alone has been extensively used in surface science to unveil molecular-level details of diffusion [38,

39], mass transport [40], catalytic reactions [41], and many other processes [42], which were inaccessible with classical bulk or ensemble measurements [151]. On the other hand, optical trapping has also found its distinctive applications, such as in Raman spectroscopy [152, 153] and photo-catalysis [154]. Despite these various attempts, a marriage of optical tweezers and SPT has yet to be implemented, but their marriage holds great promise for monitoring the time evolution of chemical reactions at the microscopic scale.

This chapter demonstrates the combined application of optical tweezers and SPT to probe surface interactions at an interface. Continuing from the previous chapter, we study the case of optically trapped gold nanoparticles, interacting with surfactant molecules adsorbed at water–glass interface. Here we introduce a new parameter, which is the chemical state of the glass surface. We alter the properties of the glass surface, which can change the morphology of the adsorbed surfactants. We compare the differences in particle behaviors on bare and treated glass surfaces. Particle trajectories on treated surfaces show evidence of long-term interactions between adsorbed molecules, which was not found in the case of bare glasses. We will discuss a likely mechanism of this phenomenon, which is related to the formation of surfactant bilayers on treated glasses and their fusion with particle bilayers. Finally, we perform statistical analyses on the time-averaged mean squared displacement of a single-particle trajectory, strengthening our interpretation of long-term bilayer interactions.

4.2 Materials and methods

4.2.1 Materials and experiments

We used the same materials and measurement setups as described in Chapter 3. A dataset for all the particle recordings and the corresponding trajectories is available in our Zenodo data repository [155].

4.2.2 Preparation of glass surface

Starting with borosilicate glass coverslips (Menzel Gläser), we prepared two different types of glass surfaces to alter the adsorbed morphologies of the surfactant molecules. One type of glass is native glass without any surface modification. The other type of glass is treated with oxygen plasma (at 200 W for 60 s with a 400 mL/min flow rate) to activate its surface [156]. The plasma-treated glasses were immediately used to prepare the fluid chambers so that we minimize the time between the surface treatment and the sample preparation. The likely structures of adsorbed molecules and the effect of surface modification on them are discussed in the following section.

4.3 Results and discussion

4.3.1 Surfactant adsorption at water–glass interface

Surfactant molecules adsorb at water–glass interfaces, spontaneously forming complex structures [132]. One of our hypotheses is that the morphology of surfactant self-assemblies can influence the particle–surface interactions. We examine this effect by altering the structure of the adsorbed molecules and comparing the subsequent particle movements. Cetyltrimethylammonium chloride (CTAC) was used as an example of a cationic surfactant.

The self-assembly structures of the adsorbed molecules depend on several factors such as pH [157], salt [158, 159], and surface preparation [160, 161]. The change in solution pH or salinity can alter the overall surfactant self-assemblies on both the particles' surfaces and the glass walls. In contrast, the surface treatments on glass surfaces can provide a selective modification of adsorbed surfactants on the treated glass walls. Therefore, we used the latter approach to examine any changes in the particle–surface interactions due to a structural change of self-assemblies on glass surfaces while keeping the surface characteristics of the particles the same.

We prepared two different glass surfaces, and surfactants formed either spherical aggregates or bilayer membranes depending on the properties of the glass surfaces (Figure 4.1). The first type of glass surface is native glass without any surface modification. We have briefly discussed how the surfactants adsorb on bare glass in the previous chapter, but here, let us take a closer look at it.

In general, a glass surface becomes negatively charged when immersed in water through the deprotonation of its silanol groups [162]:



In case of cationic surfactants, the negatively charged silanol (SiO^-) groups drive the initial adsorption through the electrostatic attraction with the cationic surfactant head groups. The adsorption of cationic molecules reduces the overall surface charge, and once the surface becomes neutralized, these molecules act as nucleation points for further adsorption [132]. At this stage, the hydrophobic interactions among surfactant tail groups drive the adsorption, similar to micelle formation in bulk solution. The molecules start to form centrosymmetric aggregates [134], aka admicelles, as shown in Figure 4.1a. The surface coverage rises steeply by forming these admicelles in this concentration span, and it soon reaches saturation near the critical micellar concentration (CMC).

The second type of glass surface is modified by oxygen-plasma treatment to increase the number of silanol groups on its surface [156]. Henceforth, we call this type of glass activated glass. After the plasma treatment, the activated surface becomes superhydrophilic due to the increased charged groups. We empirically tested the contact angle with water after oxygen-

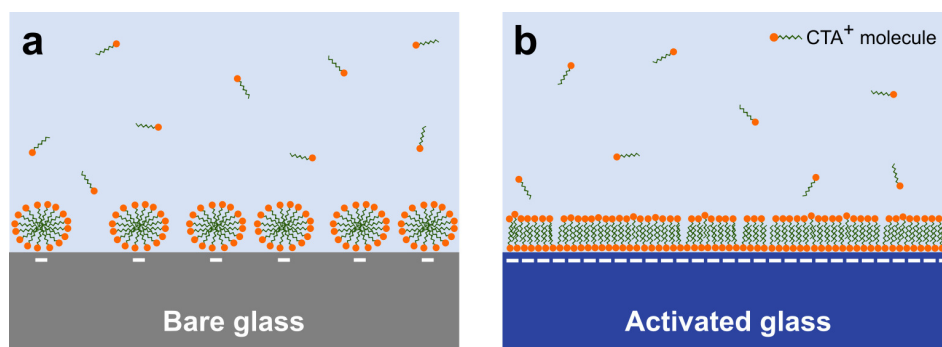


Figure 4.1 – Schematic diagram showing probable morphologies of adsorbed surfactant molecules at the glass-water interface. **a**, A bare glass and **b**, a glass surface treated with oxygen (O_2) plasma. The activated glass surface has denser silanol groups compared to the native glass. These silanol (SiO^-) groups on each surface act as electrostatic binding sites for cationic surfactant adsorption.

plasma treatment and observed complete wetting with a 0° contact angle (Figure 4.2).

When such an activated glass is immersed in a surfactant solution, the electrostatic attraction drives the initial adsorption like the adsorption with native glasses. We postulate that the adsorbed molecules are so close together that they form a quasi-continuous film. In experiments, we observed with the naked eye an immediate increase in the contact angle with surfactant solution compared to the 0° contact angle with water. Figure 4.2 shows the contact angle with the activated glass as a function of CTAC concentration, which increases with the concentration until it reaches saturation at 1 mM. Such an increase implies that a surfactant monolayer is formed with hydrophilic head groups electrostatically adsorbed to the surface and hydrophobic tail groups facing toward the bulk liquid. Any further adsorption that is hydrophobically driven forms a second layer above the first one (Figure 4.1b), rather than clustering as discrete aggregates as was the case for the bare glass (Figure 4.1a).

Such changes in self-assembly morphologies induced by the surface properties have been extensively studied in the literature [159, 161, 163]. Ducker et al. [163] studied surfactant (cetrimonium bromide, CTAB) aggregates on mica using AFM imaging. They found a transition from a flat bilayer to cylinders when reducing the binding sites on mica by introducing electrolyte (KBr). Lamont et al. [159] reported similar findings where they observed sequential changes in the structures of CTAC on mica (bilayer \rightarrow ordered cylinder \rightarrow disordered cylinder \rightarrow short cylinder \rightarrow sphere) on the addition of rival cations (Cs^+). Lastly, Grant et al. [161] investigated the influence of surface hydrophobicity on the aggregate structures of nonionic surfactants where hydrophobic interactions are the main adsorption driving force. They observed the evolution of adsorbed structures from diffuse spherical aggregates to a monolayer with increasing surface hydrophobicity. All these findings deliver the same message that the increase in active binding sites on surfaces leads to lower-curvature structures. Based on these ideas, we postulate that CTAC forms a bilayer structure on activated glass and discrete globular aggregates on bare glass as illustrated in Figure 4.1.

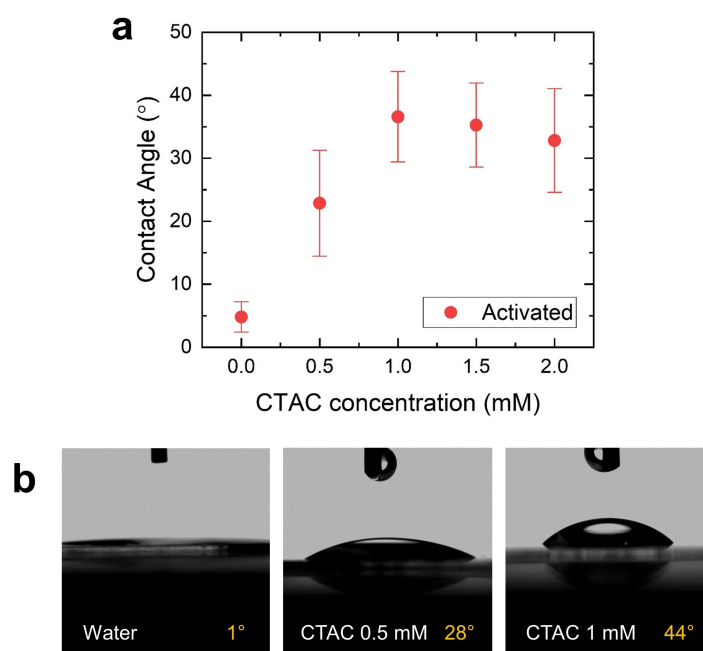


Figure 4.2 – Contact angles on activated glass surfaces. **a**, Contact angles as a function of CTAC concentration (mM). At 0 mM (pure water), the contact angle is nearly zero due to the superhydrophilic surface after oxygen plasma treatment. The angle saturates above 1 mM concentration. A contact angle goniometer (Easy Drop from Krüss) was used to measure the contact angles. At least three points on a glass surface were measured and averaged for each concentration. The standard deviations are represented by the error bars. **b**, Images of droplets captured by the goniometer's camera. Three representative concentrations (0, 0.5, and 1 mM) are shown.

4.3.2 Time-varying trajectory in an optical trap

An optical tweezer was employed to confine the motion of a particle in a local domain and facilitate monitoring the particle's trajectory. Without an optical tweezer, the gold nanoparticles did not stay in the interfacial area due to electrostatic repulsion and also because of fast Brownian motions at such a small size. We emphasize that the optical tweezer not only provided a lateral confinement (parallel to the glass–water interface) but also a vertical confinement (normal to the interface) by constantly pushing the particle towards the glass surface with its radiation pressure. These lateral and vertical confinements significantly increased the chances of particle–surface interaction and enabled monitoring *long-term* phenomena.

Figure 4.3a shows an example time-series position data extracted from a single-particle video recording. (More example trajectories are shown in Figure 4.4.) Each position data point is color-mapped, gradually changing from yellow to dark blue for legibility. The position fluctuation inside the optical trap decreases over a timespan of 40 s in Figure 4.3a. Such changes with time deviate from a simple diffusion model and can be related to the interaction that the particle undergoes with its surroundings, especially with the molecules adsorbed on the glass wall. In other words, without surface interactions, the distribution would remain the same, only restricted by the optical trap, with no temporal dependence.

To quantitatively assess the time-dependent position data, we defined a radial displacement, r_t , as the distance from the origin (corresponding to the trap center) to the particle position ($X(t), Y(t)$) where the XY -plane is a plane parallel to the glass–water interface:

$$r_t = \sqrt{X(t)^2 + Y(t)^2}. \quad (4.2)$$

Figure 4.3b shows the evolution of r_t for the same trajectory in Figure 4.3a. The gradual decrease in the envelope of r_t depicts well the temporal changes in the particle motion inside the optical trap. Since r_t fluctuates between its extremes, we calculated the moving average of r_t to smooth out the short-term fluctuations and quantify its long-term decrease. We used a time window of 5 s (corresponding to 1730 data points) to calculate the moving average, \bar{r}_t , and plotted it as the red-dashed line in Figure 4.3b.

Interestingly, such changes in particle motions occur only with activated glass surfaces. For a bare glass substrate at the same CTAC concentration – shown in the inset of Figure 4.3b – there is no apparent change in the average radial displacement, \bar{r}_t (the solid grey line in the inset). This difference between the native and activated glasses indicates that the structure of the adsorbed surfactants at the water–glass interface plays a role in the particle–surface interactions.

In addition, the absence of any changes in \bar{r}_t for the bare glass case indicates that some long-term effects of the optical tweezer, such as optical heating, are still negligible in our experimental conditions. To be more precise, the optical heating itself is not negligible based on the comparison between the thermal and non-thermal probes in Chapter 3. In fact, it can

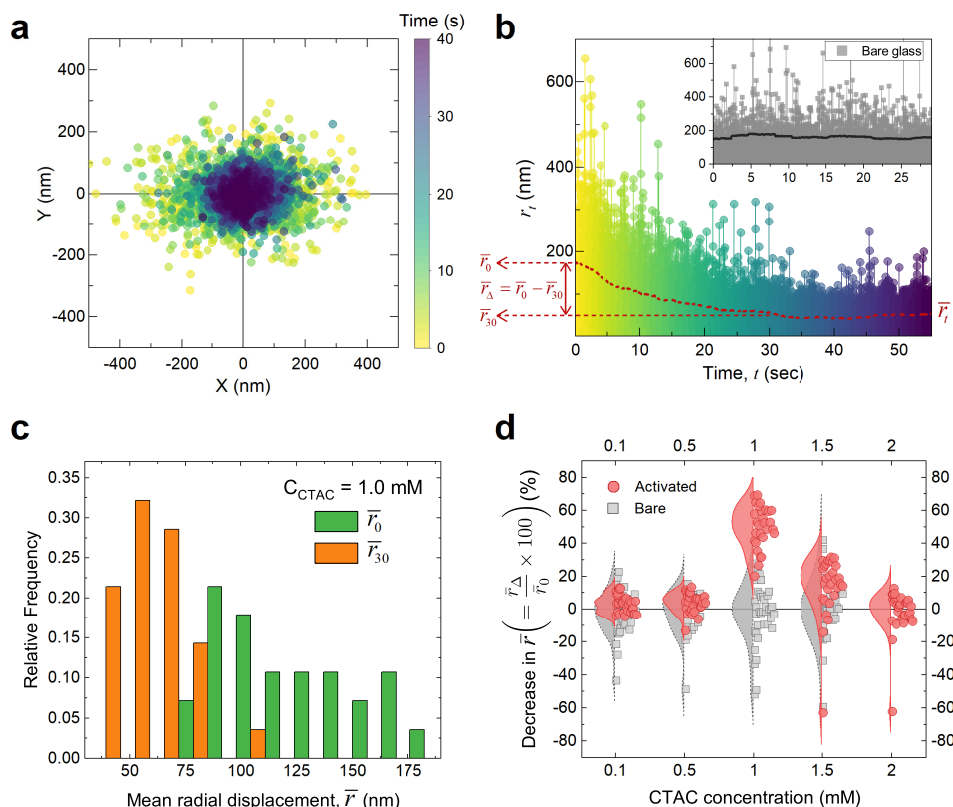


Figure 4.3 – Time-varying motion of particles in harmonic optical traps. **a**, Position distribution of a single optically-trapped particle near an activated glass wall, color-mapped with time. The XY coordinates are defined on a plane parallel to the glass surface, and the origin is aligned with the laser trap center along the laser propagation direction. **b**, Radial displacements (defined in Equation 4.2) as a function of time for the same particle in **a**. The red dashed line indicates a moving average (\bar{r}_t) with a subset size of 1730 data points. The inset shows the radial displacement of the same kind of particle at the water/bare glass interface for comparison; the grey solid line shows the same moving average. **c**, Histograms of the mean radial displacements at $t = 0$ and 30 s. The particles were trapped at $t = 0$ s and stayed in the optical trap for 30 s or more. From **a** to **c**, the CTAC concentration was 1.0 mM, and the glass surface was activated by O_2 -plasma treatment. **d**, Comparison of the decreases in \bar{r} for the first 30 seconds between the bare and activated surfaces as a function of CTAC concentration. The reduced amount, \bar{r}_Δ , is expressed as a percentage of its initial value, \bar{r}_0 .

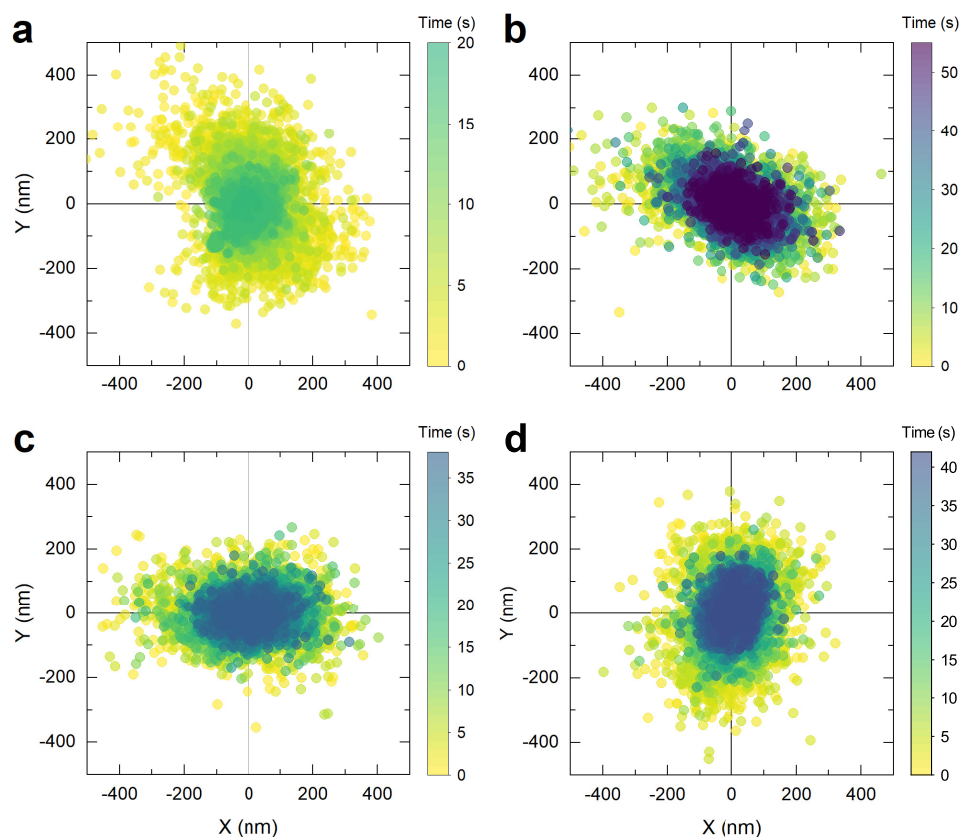


Figure 4.4 – Four more example trajectories showing different patterns. All these trajectories were measured under the same controlled condition (1mM CTAC on activated glass). A uniform color map that changes from yellow to dark blue over time is applied to all the examples for comparison. They all exhibit different position-distribution patterns and different timescales to reach an equilibrium.

accelerate the interactions by providing thermal energy. However, the thermal equilibrium is reached almost instantaneously compared to the timescale discussed in the present study (Section 2.5 for more details). Therefore, we can say that optical heating has no “long-term” effect.

The hypothesis that the particle–surface interaction is sensitive to the surfactant morphologies can be tested in two ways: (1) comparing the behavior of \bar{r}_t between bare and activated glass surfaces and (2) varying the CTAC concentration which provides different adsorption states, e.g., surface coverage and aggregate structures. To facilitate the comparisons between the different surfaces and among different concentrations, we quantified the amount of long-term decrease by the difference in the value of \bar{r}_t during the first 30 s of trapping:

$$\bar{r}_{\Delta} = \bar{r}_0 - \bar{r}_{30}, \quad (4.3)$$

which is also indicated as a red arrow in Figure 4.3b. We chose the time window of 30 s as it is a typical length of each recording, and (not all but) most of the particles reach a steady state within this period.

We performed dozens of measurements for each of the experimental conditions to average out the effect of experimental variations such as variances in particle sizes and/or charges, and the inhomogeneity of glass surfaces. Different trajectories in Figure 4.4 demonstrate these variances within the same experimental conditions. Figure 4.3c illustrates an example analysis for 28 measurements at 1.0 mM CTAC with activated surfaces. The \bar{r}_0 represents the average displacement immediately after trapping, whereas the \bar{r}_{30} represents the average displacement after staying 30 s in the optical trap. In that case, the overall left-shift of the histogram toward smaller values indicates the converging trends of particle footprints for randomly chosen particles in random locations.

We tested five different concentrations (0.1, 0.5, 1.0, 1.5, and 2.0 mM), which cover the range below and above the CMC so that each concentration corresponds to different adsorption phases. In general, the extent of surface coverage reaches its maximum near the CMC [132, 134]. In the previous chapter, we found that the CMC of our particle-CTAC mixture is 1.4 mM, which is slightly higher than the values reported in the literature (1.0 to 1.1 mM) due to the existence of the gold colloids in the solution.

Figure 4.3d summarizes the analyses of the amount of the decrease in \bar{r} for bare and activated substrates as a function of CTAC concentration. The reduction in the mean radial displacement, \bar{r}_{Δ} , is expressed as a percentage of its initial value, \bar{r}_0 . For each concentration, the data points (32 ± 6 measurements on average) are shown on the right, and the distribution fit is shown on the left. For all the examined concentrations, the average temporal change is absent for the bare glass cases (as seen in the inset of Figure 4.3b), with a distribution centered around the origin. It implies that regardless of the surface coverage increase with the concentration, the spherical admicelles on bare glass substrates have no influence on the long-term changes in particle motion.

On the other hand, the average decay in \bar{r} is much noticeable for the activated glasses but only at specific concentrations, notably at 1 mM and 1.5 mM in Figure 4.3d. These concentration-dependent results bolster the proposed hypothesis that the particle–surface interaction is responsive to the surfactant morphologies. We will elaborate on the effect of surface coverage and adsorbed morphologies in detail in the following subsection.

4.3.3 Surfactant bilayers on particle surfaces

The stark contrast of the particle motion between the bare and activated surfaces proves that the arrangement of the surfactant molecules at the water–glass interface determines whether or not long-term particle–surface interactions occur. One remaining question is why these interactions occur only with the bilayer structures and not with the globular aggregates.

A key to answering this question can be the surfactant structure on the particle surface. As we studied in detail in the previous chapter, the surfactant molecules form a bilayer on particle surfaces. In the case of the activated glass, the surfactant bilayers are present at both the water–glass interface and the particle surface. Their structural resemblance can be the key to understanding their interactions. For instance, these bilayers can be more likely to merge, similar to the fusion of lipid bilayers in life [164, 165]. In general, bilayers are known as a highly mobile structure [144]. As a result, the outer layer can migrate over the first layer without leaving the surface completely [132]. The first layer, which is electrostatically adsorbed on the surface, can be more tightly bound and not easily dissociated from the surface. Therefore, when the two bilayers come close in the instances of particle trapping, a disruption and rearrangement of the outer layers may occur, which can affect particle behaviors.

4.3.4 Effects of bilayer coverages on long-term interactions

Figure 4.5a and c illustrate the likely development of the surfactant morphologies over the investigated concentration range. We studied in depth the particle behaviors on bare glass substrates (Figure 4.5a) in Chapter 3. Here we focus more on the difference between bare and activated surfaces, and especially, on the particles' behaviors on bilayer membranes (Figure 4.5c) and their long-term interactions (Figure 4.5b).

Before going into detailed discussions, we make an assumption about this system. We assume that the effect of surfactants in the bulk solution is insignificant in long-term reactions. As supporting evidence, long-term changes were not observed in the bare glass case across the whole concentration range tested in this study (Figure 4.3d). This implies that the surfactants in the bulk solution are of little effect in long-term behaviors, whether they exist as monomers below the CMC (0.1, 0.5, and 1.0 mM) or micelles above the CMC (1.5 and 2.0 mM).

Figure 4.5b shows the summary of trajectory analyses, quantified as the statistics of the mean radial displacement, \bar{r}_t , as a function of CTAC concentration. Each data point was calculated from an independent measurement of single-particle trajectory. Three datasets are plotted

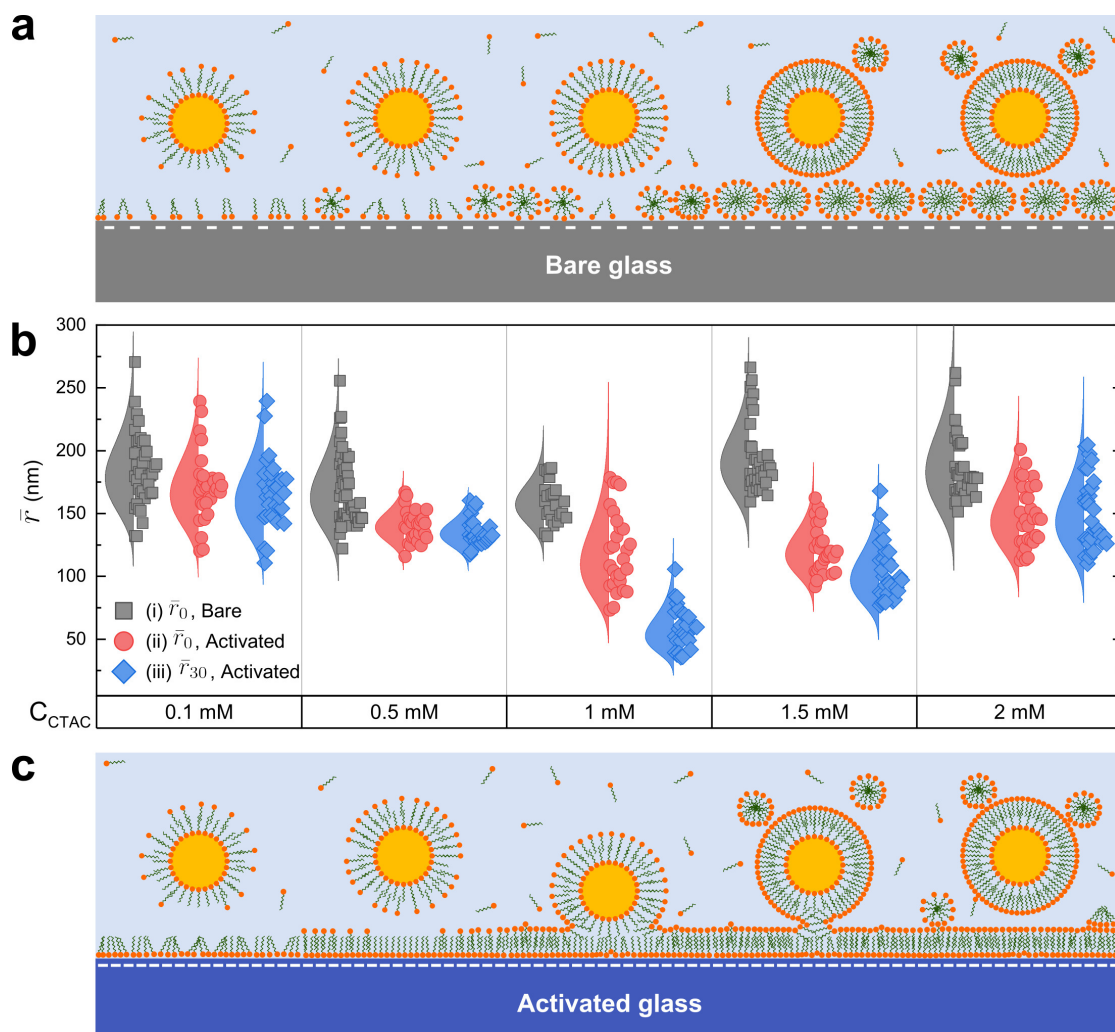


Figure 4.5 – Effects of surfactant morphologies on particle motion as a function of concentration. **a** and **c**, Cartoons showing plausible surfactant self-assembly formations at the gold/water and glass/water interfaces. When the glass surface is activated with O_2 -plasma treatment, the adsorbed surfactant structure is assumed to undergo a conformational change from globular aggregates to bilayers. The changes in surface coverage and aggregate morphologies is depicted according to the surfactant concentration. **b**, Distributions of mean radial displacement (\bar{r}) as a function of CTAC concentration. Three datasets are displayed side by side for comparison: (i) \bar{r}_0 , bare glass, (ii) \bar{r}_0 , activated glass, and (iii) \bar{r}_{30} , activated glass.

side by side for comparison: (i) the initial mean (\bar{r}_0) for bare glass, (ii) the initial mean (\bar{r}_0) for activated glass, and (iii) the mean after 30 s (\bar{r}_{30}) for activated glass. The distribution of \bar{r}_{30} for bare glass is not shown in Figure 4.5b for clarity as it remains similar to \bar{r}_0 in (i). The data points in (ii) and (iii) were calculated from the same dataset as they refer to the initial and steady-state values, respectively.

A comparison among (i), (ii), and (iii) across different concentrations provides qualitative insights into the mechanisms that govern the particles' motions on different surfaces: one is the hydrophobic interaction between the particle and the surface, and the other is the extent of bilayer coverage. Compared to admicelles, the primary distinction of bilayer structure is that the hydrophobic interiors can be exposed to the bulk fluid. The exposed hydrophobic groups on a glass surface can interact with hydrophobic groups on a particle surface when the particle approaches. The resulting attraction force explains the decrease in \bar{r} for the bilayer structures in Figure 4.5b compared to the spherical ones. An exception occurs, however, at the lowest concentration (0.1 mM), where the structural difference at this low coverage is negligible.

On the other hand, the coverage extent determines how much and how fast the \bar{r} decrease will be. When a particle is brought to the surface by the optical tweezer, the hydrophobic interaction brings the particle closer to the surface. As a result, the charged head groups can be disrupted and rearranged, creating a hydrophobic patch below the particle (as illustrated below the second particle in Figure 4.5c) and, consequently, developing an electrostatic trapping potential. The size of the hydrophobic patch in the bilayer membrane will determine how tight the confinement will be. At low coverages, the confinement of the particle will be moderate, and the reaction will take place promptly as there are a relatively small number of molecules to rearrange. The results at the second lowest concentration (0.5 mM) in Figure 4.5b support this idea. They show a relatively modest decrease in \bar{r} compared to higher concentrations (1 mM or 1.5 mM); furthermore, this decrease happens in the early stage of the trapping so that we do not see much differences between \bar{r}_0 and \bar{r}_{30} . The variance of the distribution of \bar{r} also decreases significantly, compared to that at the lowest concentration. In other words, the rearrangement process seems to reduce the effect of experimental variations originating from surface heterogeneity.

As the coverage increases with concentration, the overall hydrophobic area (i.e., the exposed hydrophobic regions of the first layer) shrinks, and the surfactant bilayer surrounds a trapped particle more tightly, as depicted in Figure 4.5c. The dramatic decrease in \bar{r} at 1.0 mM supports this explanation. Other noticeable differences at this concentration are the long-term decrease in \bar{r} over tens of seconds (from \bar{r}_0 in (ii) to \bar{r}_{30} in (iii)) and the broadened distribution of \bar{r}_0 in (ii). These two phenomena can be closely related and understood by the following explanation. The slow interaction can be a consequence of a two-step process. The incomplete particle bilayer is first combined with the nearest hydrophobic patches on the glass surface (the initial response related to \bar{r}_0). This contact domain then gradually grows by taking in other hydrophobic patches that were initially not in the immediate vicinity but slowly diffused over

the surface to the particle location (the transition from \bar{r}_0 to \bar{r}_{30}) [38]. Due to the random nature of the surface states, this process can happen at various rates (as shown in Supplementary Figure 4.4), which can result in the broad distribution of \bar{r}_0 in the initial stage of the process. Such a slow diffusion is less obvious at 1.5 mM in Figure 4.5b. This can be interpreted as that the bilayer coverage has almost reached its saturation at this concentration near the CMC (as expected in general [132]), and there are hardly any exposed hydrophobic interiors nearby that can diffuse and cooperate.

As a side note, a similar effect of rearrangements can also occur with spherical admicelles [112], shown as a slight decrease in \bar{r}_0 in (i) when increasing the CTAC concentration from the lowest concentration up to the full coverage concentration in Figure 4.5b. However, the effect seems much more limited than in the bilayer case.

At the highest concentration (2.0 mM) above the CMC, the effect of bilayer interaction is further reduced. The particles' zeta potentials have increased due to micelles' association with the particle surface (Figure 3.6c in Chapter 3). This can be interpreted as the completion of the particle bilayer. We also expect a full surface coverage on the glass surface at this concentration higher than the CMC. As a result, the complete bilayers and stronger electrostatic repulsion between the particle and the surface can hamper the interaction (the last particle in Figure 4.5c). Accordingly, the \bar{r} recovers its mean and variance comparable to those at the lowest concentration.

4.3.5 MSD analysis of a time-varying trajectory

We have interpreted particle dynamics by examining particle trajectories and investigating the effect of surfactant morphologies and coverages in particle–surface interactions. So far, we have focused on the statistical mean and variance of \bar{r} , changing with time and concentration. On the other hand, each trajectory can also be analyzed further by taking the statistics along its time axis. The *time-averaged* mean squared displacement (MSD) is the most common measure as we have dealt with in Chapter 3. Using the time-averaged MSD, for example, we can analyze the forces acting on the particle, based on a priori knowledge of particle dynamics [125, 147]. To be more precise, we first formulate a Langevin equation to describe the motion of a particle and compare the measured MSD with the MSD solved for the Langevin equation. Any deviation from the theoretically solved MSD can prove the involvement of additional forces or interactions.

We have already modeled a particle in an optical trap as a damped harmonic oscillator in a fluid in Chapter 3 (Equation 3.2) [125]. We write the Langevin equation here again:

$$m\ddot{x}(t) + \gamma\dot{x}(t) + \kappa x(t) = F_{\text{therm}}(t), \quad (4.4)$$

where m is its inertial mass, γ is its damping (fluid friction) coefficient, κ is the spring constant of the optical trap, and F_{therm} is the random thermal force. We also repeat the solution for

MSD to the Langevin equation [125]:

$$\text{MSD}_{\text{Langevin}}(\tau) = \frac{2k_B T}{\kappa} (1 - e^{-\tau\kappa/\gamma}), \quad (4.5)$$

where k_B is the Boltzmann constant and T the temperature.

To attest to the involvement of additional forces arising from the particle–surface interactions, we calculated the time-averaged MSD from the measured trajectory shown in Figures 4.3a. This trajectory, \mathbf{T}_N , is a time-series position data of length N :

$$\mathbf{T}_N = \{(X_1, Y_1), (X_2, Y_2), \dots, (X_N, Y_N)\}, \quad (4.6)$$

where each position is defined in a two-dimensional space. For this trajectory, \mathbf{T}_N , the time-averaged MSD is defined as follows [147]:

$$\text{MSD}_{\text{measured}}(\tau) = \frac{1}{N - \tau} \sum_{i=1}^{N-\tau} \{(X_{i+\tau} - X_i)^2 + (Y_{i+\tau} - Y_i)^2\}, \quad (4.7)$$

for any time lag $\tau = 1, 2, \dots, N - 1$. We subdivided the trajectory into five second-long segments and calculated the time-averaged MSD for the first segment ($t = 0 - 5$ s) and another segment after reaching the steady state ($t = 50 - 55$ s) for comparison.

The first segment corresponds to the timespan when the particle has just been trapped and initiated any interaction. The MSD calculated from this segment using Equation 4.7 is plotted in Figure 4.6a in a double logarithmic scale. The next step is to fit the $\text{MSD}_{\text{Langevin}}$ to this MSD obtained from the experiment. However, the solution given in Equation 4.5 is for a one-dimensional trajectory. Since we used the measured trajectory defined in two dimensions (Equation 4.7), the solution of the Langevin equation should also be multiplied by the trajectory dimension. Therefore, we used a modified solution of the Langevin equation for two dimensions ($= 2 \times \text{MSD}_{\text{Langevin}}(\tau)$) to fit it to the measured MSD. Before executing the curve fitting, we also estimated the temperature K at the particle to be 366.61 K, a value calculated from an electromagnetic heating simulation (Section 2.5 for more details). Then we estimated the values of the spring (κ) and damping (γ) constants in the least-squares sense as shown in Figure 4.6a. The measured MSD shows a good agreement with the theoretical MSD, implying that the Langevin equation successfully describes the initially trapped particle motions.

Since we know the average size of the particle, we can also roughly estimate the drag coefficient γ using Stokes' drag (the frictional force exerted on a spherical object in a viscous fluid): $\gamma_{\text{Stokes}} = 3\pi\eta d$, where η is the viscosity of the fluid and d the particle diameter. This drag should be corrected further as the particle moves near the glass wall [142]. Assuming that the particle–surface gap is roughly 1/10 of the particle radius, the hydrodynamic drag increases by ~ 2.36 times near the surface compared to the Stokes' drag [166]. The drag coefficient, therefore, is approximated as 1.41×10^{-9} N·s/m by assuming the particle diameter $d = 150$ nm

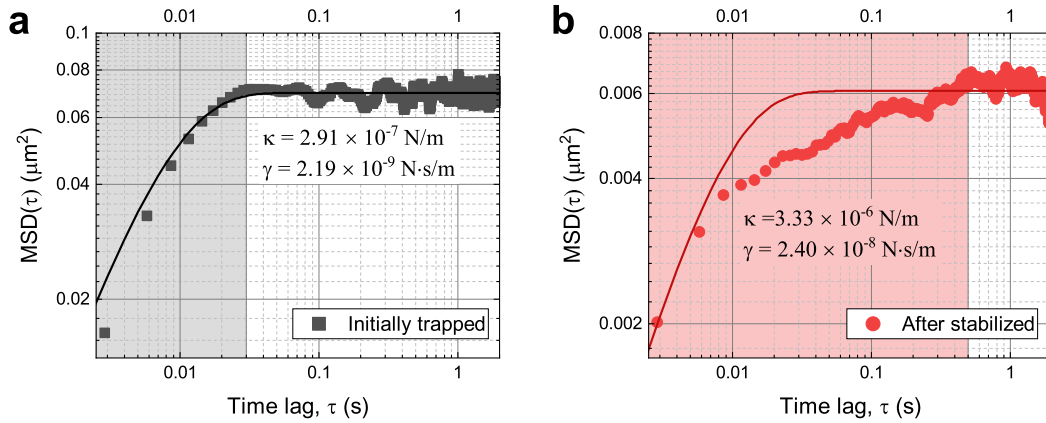


Figure 4.6 – Time-averaged mean squared displacement (MSD) of segmented trajectories. **a**, Time-averaged MSD calculated from the first five-second segment of the trajectory shown in Figure 4.3a. The MSD solution of the Langevin equation in 2D (black solid line) is fitted to the measured MSD (grey squares). **b** Time-averaged MSD from a segment of the same trajectory after reaching a steady state (red circles). The 2D solution of the Langevin equation (red solid line) is fitted to the data, with constraints on κ and γ to keep the fitted curve within the upper and lower limits of the measured MSD. The shaded areas in **a** and **b** indicate the time lags to reach the MSD plateaus.

and the viscosity $\eta = 0.423 \text{ mPa}\cdot\text{s}$ for water viscosity at 340 K (Section 2.5 for water temperature simulation). This value of γ is comparable to the value we found from the curve fitting of MSD_{Langevin} to the measured MSD ($2.19 \times 10^{-9} \text{ N}\cdot\text{s/m}$). The discrepancy between them can be attributed to any mismatch between the assumptions and the actual values for the particle size and water viscosity. It can also be attributed to the particle–surface interaction during the first five trapping seconds.

In contrast to the initial segment, the MSD calculated from the segment after reaching the steady state exhibits an anomalous behavior that is significantly deviating from the theoretical prediction (Figure 4.6b). For the curve fitting in this case, we applied a boundary condition for κ and γ ($0 < \kappa < 4 \times 10^{-6}$; $0 < \gamma < 2.4 \times 10^{-8}$) to keep the fitted curve between the minimum and maximum values of the measured MSD for the measured time lags. The estimated value for κ has increased about ten times compared to the value fitted to the initial segment. It supports our hypothesis that the rearrangement of the incomplete bilayer can create a complementary trapping potential. The estimated drag, γ , has also increased about ten times, likely due to the increased restrictions in particle motion imposed by the bilayer interactions based on our hypothesis. Most importantly, the Langevin equation now fails to describe the motion of the particle after reaching the steady state. This implies that the particle does not behave like a damped harmonic oscillator anymore, suggesting the emergence of a new type of force or physical interaction such as the fusion of the bilayers, as we suggested earlier.

Some theoretical works also suggest that the subdiffusive behavior between $\tau = 0.01 \text{ s}$ and 0.5 s

in Figure 4.6b can represent geometrical confinement [167, 168]. Furthermore, several experiments in biology reported similar findings that the subdiffusive motions of probe molecules were caused by an increased obstruction such as polymer networks in the cytoplasm [169] or the presence of the cell nuclei [170]. In addition, a very similar time-averaged MSD dependence on τ was also reported by Jeon et al. [171] with a polystyrene bead in a worm-like micellar solution, where the elongated micelles form a transient polymer network. They explained that such a characteristic subdiffusive motion in the millisecond range resembles the movement of a particle in a viscoelastic medium. These theoretical and experimental findings provide solid evidence that the particle in Figure 4.6b experiences geometrical confinement and a coincident viscoelastic effect, which can be related to the interactions among surfactant molecules. However, an important difference in our case is that these interactions were constrained to the interface since the surfactant concentration was below the CMC, i.e., prior to the micelle formation in the bulk solution. Therefore, the MSDs in Figure 4.6a and b corroborate the idea of the bilayer rearrangement and the partial fusion proposed in the previous section.

4.4 Conclusion

We have examined the trajectories of colloidal particles locally confined at a water–glass interface by an optical tweezer. Individual trajectories of single nanoparticles showed local and dynamic behaviors of the surrounding molecules in real time, which have been obscured in traditional thermodynamic experiments. We analyzed the particles' spatial and temporal motions and provided new insights into the interactions governing the particle motions at the nanoscale. Especially, by studying the unique system consisting of a gold nanoparticle, a glass–water interface, and surfactants, we found evidence of the fusion of surfactant bilayers at the narrow gap between the particle and the surface. Our findings demonstrate the great potential of optically trapped nanoparticles as a probe to investigate real-time chemical processes at the nanoscale. In particular, we expect that this marriage of SPT and optical manipulation can also shed new light on even more complex interfacial phenomena when combined with recent developments in three-dimensional SPT [42] and high-speed imaging [172].

5 Optical forces on a plasmonic particle in a plasmonic trap

A part of this chapter has been published in a peer-reviewed journal [70]:

Studying the different coupling regimes for a plasmonic particle in a plasmonic trap

Jeonghyeon Kim and Olivier J. F. Martin

Optics Express, Vol. 27, Issue 26, pp. 38670–38682 (2019)

<https://doi.org/10.1364/OE.379435>

5.1 Introduction

Conventional optical trapping has a limit in its stiffness and resolution, especially when manipulating nanoscale particles [11, 73, 173]. Due to the decrease in the viscous drag for small particles, the Brownian motion lets tiny particles easily escape from the trap. Furthermore, the optical force also scales down with the volume of the object [173]. Another issue is the diffraction limit of the trapping laser: an object much smaller than the focal spot or the beam waist experiences unstable trapping [11]. As a result, the manipulation of nanoscale particles is inherently challenging [73, 173]. In order to enhance the trapping stiffness of such small objects, one can increase the power of the trapping laser, for example [11], or implement an alternative trapping geometry such as counter-propagating beams [174].

Near-field optics and plasmonics have provided another possibility to achieve nanoscale manipulation by focusing light below the diffraction limit and locally amplifying the fields [88, 89, 175–181]. Plasmonic antennas are metallic, mostly gold or silver, nanostructures where their conduction electron clouds can resonantly oscillate through optical illumination [84, 182]. Under resonant conditions, the electron oscillations produce a strong near-field, which decays very rapidly in space; thus, the enhanced field gradient around the antenna provides additional confinement for trapping, overcoming the diffraction limit [183, 184]. Plasmonic antennas also amplify fields through localization, which can also improve the trapping stiffness [185].

Metallic nanoparticles, thanks to their strong optical response, are very good candidates for

nanoscale manipulation. A previous belief on metallic particles was that they are difficult to trap due to their highly reflecting properties [186, 187]. Another issue was that metallic particles have resonant characteristics like plasmonic antennas, which can significantly alter the trapping conditions on resonance [188]. However, metallic particles are found to experience either an attractive or repulsive force depending on the incident wavelength [67, 189, 190]. This behavior originates from the wavelength-dependent scattering, absorption, and polarizability of plasmonic particles. In particular, experimental studies have shown that metallic particles can be stably trapped when illuminated with infrared light since they behave like a high refractive index dielectric particle at wavelengths longer than the resonance [191–194]. Since the trapping force is proportional to the polarizability of a particle, it is especially strong for a metallic particle that has large polarizability [74]. This compensates for the decrease in optical force associated with the small volume of nanoscale particles.

A combination of plasmonic antennas and metallic nanoparticles is appealing for the precise positioning of single nanoscale objects. However, special attention must be paid in this case because both the trap, i.e. the antennas, and the trapped metallic objects can be optically excited and can furthermore interact with each other. Although several experiments have demonstrated plasmonic trapping [88, 89, 176–178, 180, 184], the sheer resonant characters of both the trap and the trapped particle call for studies on the coupling between these two resonant structures and the influence of this coupling on the optical forces.

In this chapter, we theoretically study the optical force exerted on a metallic particle trapped by a plasmonic dipole antenna. We investigate the change in optical force as a function of the particle size, position, and incident wavelength (throughout we refer to the particle diameter as its size). A priori, one would think that the influence of the metallic particle on the near-field of the antenna can significantly influence the field distribution and therefore the optical force. In practice, this would imply that only full-field calculations taking into account both the plasmonic dipole antenna and the trapped particle can accurately capture the physics of the system. Quite surprisingly, it appears that the dipole approximation remains accurate, even in such an intricate system, when the particle size is small enough to apply that approximation. We confirm this by comparing the force obtained from full-field calculations that consider the self-consistent system with those from an analytical equation that assumes the particle as a mere induced dipole. In the second half of the paper, we also study the force acting on a wide range of particle sizes (10 – 200 nm) with full-field calculations. We evidence attractive and repulsive behaviors for particles larger than 150 nm in the presence of a plasmonic antenna.

5.2 Results and discussion

5.2.1 Plasmonic dipole antenna

We consider a nanoscale dipole antenna as a plasmonic optical tweezer (Figure 5.1). The dipole antenna consists of two gold nanorods separated by a gap. Each nanorod is a rounded

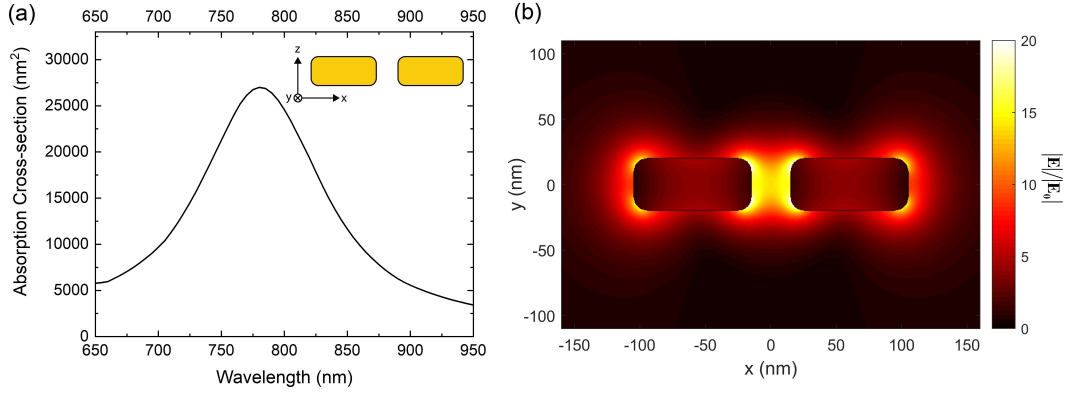


Figure 5.1 – Gold dipole antenna used in this chapter. The antenna consists of two nanorods with dimensions $90 \times 40 \times 40 \text{ nm}^3$ separated by a 30 nm gap. The light is incident in the $+z$ -direction, polarized along the x -axis. (a) Absorption cross-section and (b) electric near-field amplitude enhancement factor at $\lambda = 780 \text{ nm}$; the gradient of this enhanced near-field exerts an optical force on an object located nearby.

rectangular cuboid (90 nm length, $40 \times 40 \text{ nm}^2$ cross-section) and the gap is set to be 30 nm. We choose a 30 nm gap size such that a 20 nm spherical particle, which is the target object to trap here, can pass through the gap. For all the simulations throughout the paper, we put the antenna in a Cartesian coordinate system with the origin at the center of the gap and the longitudinal axis of the antenna along the x -axis. We set the dielectric constant of gold from Johnson and Christy [195] and that for the medium to be 2.013, an average of water (1.77, superstrate) and glass (2.25, substrate), to mimic the effect of a substrate [196, 197]. The incident light propagates along the $+z$ -direction, polarized along the x -axis (Figure 5.1(a), inset) with the power intensity of $4 \text{ mW}/\mu\text{m}^2$.

5.2.2 Methods for calculating optical forces

When we place a metallic nanoparticle in the near-field around the antenna, the spatially varying near-field induces a force on the particle. Furthermore, since the metal particle is close to the antenna, the particle can modify the near-field due to a strong interaction with the antenna. Depending on the size and the location of the particle, the field disturbance caused by the interaction may well be significant or negligible. We shall study this effect by computing the optical force using two different approaches.

Full Maxwell's stress tensor (MST)

The first approach is based on Maxwell's stress tensor, with which we compute the time-averaged optical force \mathbf{F} by integrating the stress tensor σ on the surface of the particle S :

$$\langle \mathbf{F} \rangle = \oint_S \langle \sigma \rangle \cdot \mathbf{n} ds, \quad (5.1)$$

where the expression $\langle \dots \rangle$ denotes the time average, \mathbf{n} the outward unit vector normal to the surface, and ds an infinitesimal surface element. In the remaining of the paper, we refer to this approach as the Maxwell's stress tensor (MST) approach.

The Maxwell's stress tensor σ is commonly expressed as a function of electric (\mathbf{E}) and magnetic (\mathbf{H}) fields; here we obtain it directly from the surface integral equation (SIE) formulation of Maxwell's equations [106, 109]. We use the SIE formulation throughout this chapter to simulate the interaction of light with plasmonic structures. For the derivation of SIE, we refer to Refs. [106] and [109]. The details of its practical use for the computation of MST can be found in the Methods section (Section 2.4). We also provide open datasets from the SIE formulation and its analysis for calculating the force and other physical values in Ref. [198].

Dipole approximation (DA)

The second approach starts by assuming that the particle is sufficiently smaller than the illumination wavelength (with a particle size $< 1/10$ the background wavelength) to behave like an induced point dipole. By approximating the particle as a point-like dipole, this method does not take into account the influence of the particle's physical boundary onto the near-field. We first evaluate the near-field generated by the antenna alone at the location of the particle and then find an analytical solution for a time-averaged force with the electric field at the particle position [66].

We assume an arbitrary monochromatic electromagnetic wave with angular frequency ω , which describes the near-field generated by the antenna. With the assumption of time-harmonic fields with the form $\exp(-i\omega t)$ [74], the induced dipole moment of the particle is proportional to the electric field at the particle position \mathbf{r}_0 [43]:

$$\mathbf{p} = \varepsilon_m \alpha(\omega) \mathbf{E}_0(\mathbf{r}_0), \quad (5.2)$$

where ε_m is the relative permittivity of the surrounding medium and α is the polarizability of the particle. The polarizability α is the parameter that includes the size information of the particle; under the dipole approximation, it can be expressed as [74]:

$$\alpha(\omega) = 4\pi\varepsilon_0 a^3 \frac{\varepsilon - \varepsilon_m}{\varepsilon + 2\varepsilon_m}, \quad (5.3)$$

with the parameters ε_0 denoting the permittivity of the free space, ε the relative permittivity of the particle, and a the radius of the particle. The relative permittivities in Eqs. (5.2) and (5.3) are those appropriate to the incident frequency ω . The time-averaged force exerted by an

arbitrary electromagnetic field can then be evaluated as [43, 66]:

$$\langle \mathbf{F} \rangle = \sum_i \frac{1}{2} \text{Re}\{p_i^* \nabla E_{0i}\}, \quad (5.4)$$

where p_i^* and E_{0i} ($i = x, y, z$) are respectively the complex conjugates of the dipole moments and the electric field components of a three-dimensional Cartesian coordinate system. Since this approach is based on the dipole approximation, we will refer to it as the dipole approximation (DA) method.

Let us emphasize that while the MST method provides a self-consistent solution that includes the interaction between the trapped particle and the trapping antenna, the DA method does not include this interaction, and the optical force is merely computed from the near-field distribution produced by the antenna in the absence of the particle. Since the interaction between a metallic particle and a plasmonic antenna can be very strong [199], we would anticipate that the MST method provides a much better accurate description of the optical force. The next subsection aims at clarifying this point.

5.2.3 Comparison between Maxwell's stress tensor (MST) and dipole approximation (DA) methods

Using the MST and DA methods, we first compare the optical force vectors when moving a spherical gold nanoparticle with a 20 nm diameter (the green circle in Figure 5.2) above the antenna. We assume that a monochromatic plane wave at $\lambda = 800$ nm, close to the resonance of the antenna, comes from the bottom of the figure (in the $+z$ -direction). We change the position of the particle between -150 nm and 150 nm in the x -direction while keeping the spacing between the bottom surface of the particle and the top surface of the antenna to 5 nm. The red and black arrows show a line of force vectors calculated using the MST and DA methods, respectively. The values computed with MST (red arrows) are larger than those computed with DA (black arrows), especially where the field is extreme, at each corner of the nanorods. This implies that the interaction between the particle and the antenna becomes stronger when the particle is located at those extreme fields. It also indicates that the interaction between the particle and the antenna works in a way that reinforces the fields and, therefore, the optical force. This is in agreement with the binding interaction that is evidenced within the hybridization model [189].

The optical force depends on the wavelength of the incoming plane wave due to the resonant characteristics of the antenna. In Figure 5.3(a), we compute the vertical component of the optical force (along the z -axis) as a function of the wavelength of incident light while fixing the position of the 20 nm diameter gold nanoparticle 5 nm above the top of the antenna (i.e., the particle center is 35 nm above the center of the gap, viz. the origin). The negative sign of the force means an attraction toward the gap. Both MST and DA methods result in similar wavelength-dependent forces with less than approximately 10 % difference, although the

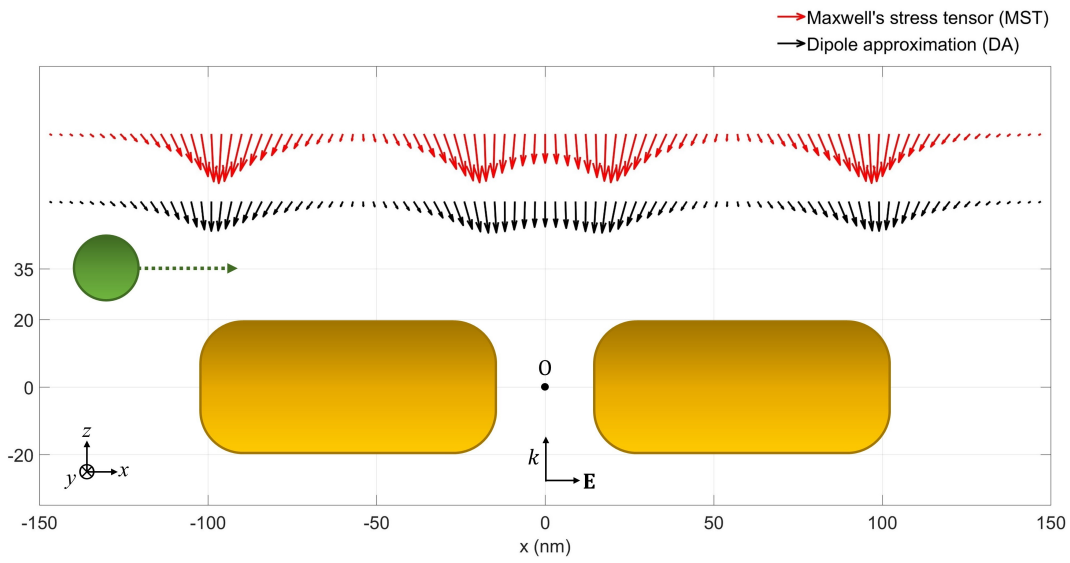


Figure 5.2 – Optical force vectors for a 20 nm gold nanoparticle (green disk), as a function of its position along the x -axis. The spacing between the bottom surface of the nanoparticle and the top surface of the antenna is 5 nm and the illumination wavelength is $\lambda = 800$ nm. The optical force vector at each position is computed 1) analytically using the dipole approximation (DA, the black arrows) or 2) numerically using the Maxwell's stress tensor (MST, the red arrows); the corresponding data are shifted vertically for legibility.

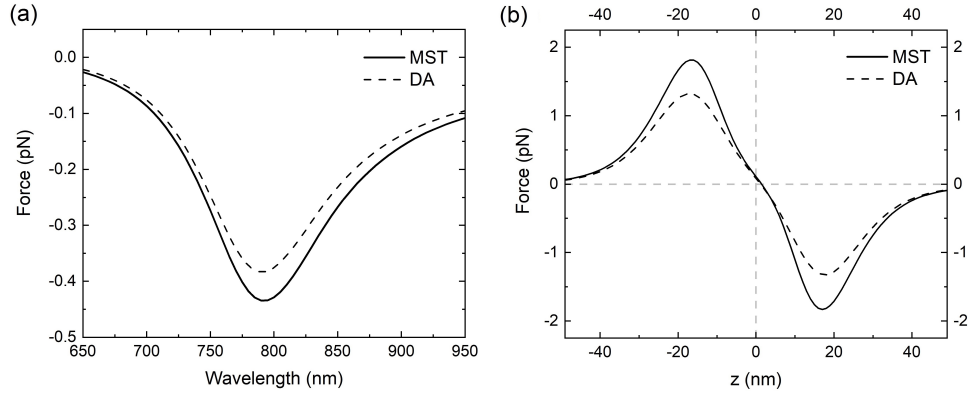


Figure 5.3 – (a) Force as a function of the illumination wavelength when the particle is fixed at (0, 0, 35 nm), which is 5 nm above the antenna top surface. (b) Force when the particle is moved along the z-axis in the center of the gap ($x = y = 0$) while the incident wavelength is fixed as $\lambda = 800$ nm.

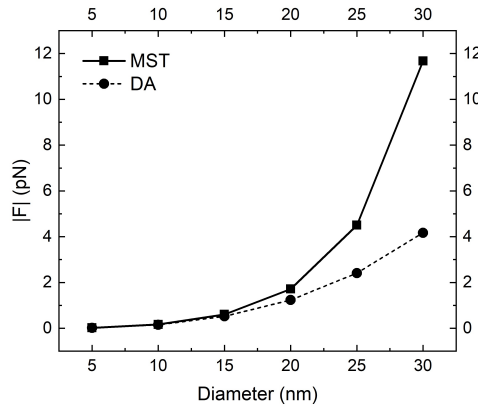


Figure 5.4 – Optical forces acting on particles with different sizes, centered at the point (0, 0, 20 nm), where the field is strongest ($\lambda = 800$ nm).

solution from MST always shows larger forces than that from DA for the range of calculations. The MST method also shows the force spectrum slightly red-shifted compared to that of the DA method since it includes the nanoparticle and its hybridization with the antenna, which lowers the energy of the system, leading to a redshift [189, 200].

While the two calculation methods show a good agreement in the previous case, they can also give considerably different results, especially when the particle stands between the corners of the nanorods where it feels the most substantial field gradient. In Figure 5.3(b), we evaluate the force as a function of the particle position while the particle passes through the gap of the antenna vertically along the z-axis. The difference in the force becomes prominent when the particle becomes closer to the points where the gradient of the field is most significant, i.e. the force magnitude is the largest. Like in the case of Figure 5.3(a), this difference implies the active involvement of the particle in the field since the DA method does not include such influence [179].

This effect stands out more when increasing the size of the particle while fixing its position between the top corners where the field is strongest, i.e. at the point (0, 0, 20 nm). In Figure 5.4, we evaluate the magnitude of the trapping force for different particle sizes ranging from 5 to 30 nm (incident wavelength $\lambda = 800$ nm). The force magnitude increases to the third power of the diameter when we use the dipole approximation since the polarizability is proportional to the particle volume [43]. When we introduce the actual particle geometry for numerical calculations with MST, the gaps formed between the particle and the corners of the antenna enhance the field, leading to significantly greater forces for larger particles. For instance, the force for the 30 nm-diameter particle, where the additional gap size goes down to 2 nm, becomes 2.8 times larger than that from the DA method.

5.2.4 Wavelength and particle size dependence of the optical force

As seen in Figs. 5.3 and 5.4, the force depends on the particle size, the illumination wavelength as well as the location of the particle. Here we look in greater detail into the influences of these parameters on the optical force, whereas the previous section was dedicated to the comparison between the numerical and analytical methods. We use the MST method since it predicts the near-field acting on a particle more accurately by taking into account the field modification caused by the particle and also because the dipole approximation is not valid anymore for particles exceeding the Rayleigh regime.

In Figure 5.5, we plot the optical force as a function of the particle size (10 – 200 nm, the x -axis) and the illumination wavelength ($\lambda = 650 - 950$ nm, 5 nm step, the y -axis). In order to vary the particle diameter up to 200 nm without changing gaps and hence varying coupling between the particle and the antenna, we fix the distance between the bottom of the particle and the top surface of the antenna to be 5 nm and move the particle center accordingly, as shown in the inset of Figure 5.5.

In this wide range of sizes, interesting features start to appear. First, the force increases with the diameter up to 100 nm, and then it decreases above this size. However, for particle size larger than 160 nm, we discover a different regime whereby the force becomes either attractive or repulsive, depending on the wavelength. To better understand the physics behind these complicated features, we selected four different parameter sets indicated as A, B, C, and D in Figure 5.5, which represent different coupling regimes. We first analyze the resonance spectra of the coupled particle-trap system for those instances (Figure 5.6) and look into further details by evaluating the near-fields and surface polarization charges (Figure 5.7).

Coupled particle-trap system

In Figure 5.6, we show the absorption cross-sections of the system including both the antenna and the particle as the resonance spectra of the coupled particle-trap system. The grey solid line in each figure represents the response of the antenna only, and they are plotted

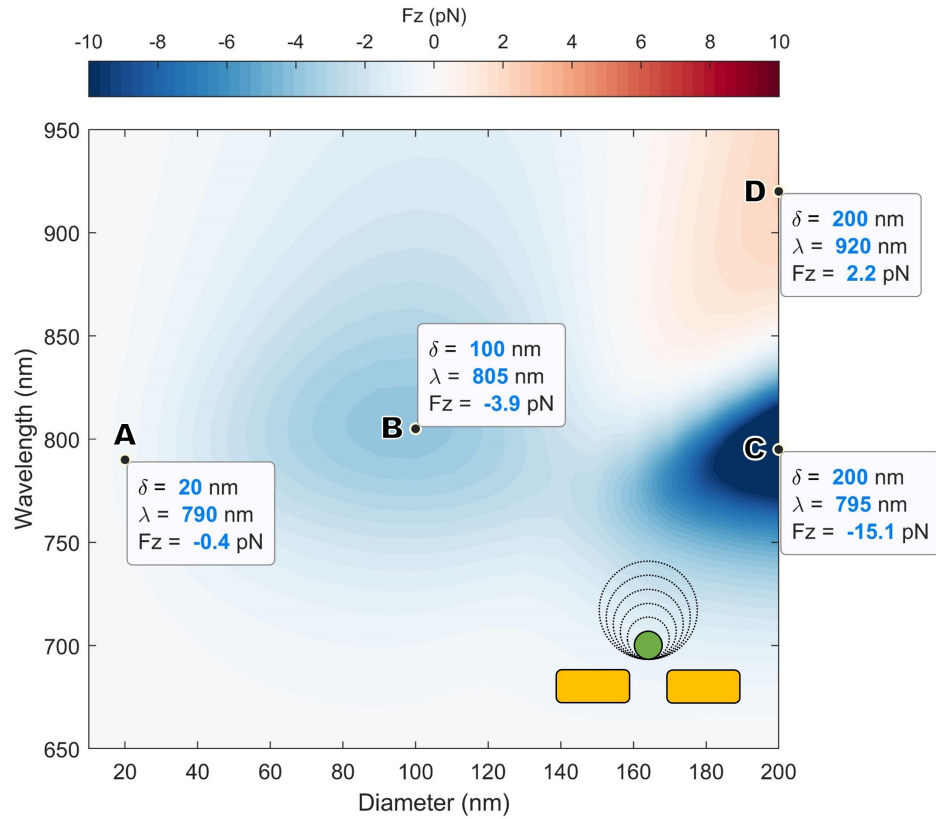


Figure 5.5 – Size and wavelength dependence of the optical force using the MST approach. The gold nanoparticle diameter δ is varied from 10 nm to 200 nm. The bottom of the nanoparticle is fixed 5 nm above the top surface of the dipole antenna to maintain the physical gap, while its center position is moved accordingly, as sketched in the inset (Bottom right). We analyze the points A, B, C, and D in Figures 5.6 and 5.7.

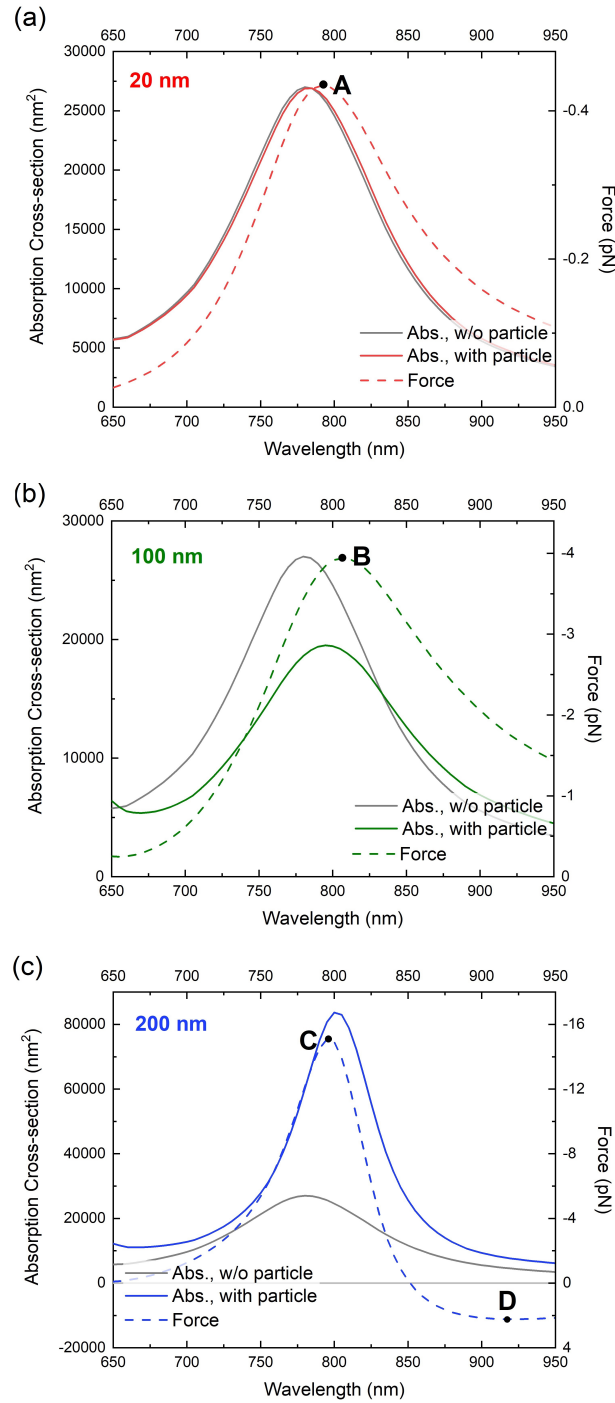


Figure 5.6 – Resonance spectra of the coupled particle-trap system for the particle size of (a) 20 nm, (b) 100 nm, and (c) 200 nm. The force exerted on the corresponding particle is plotted as dashed lines. The response of the trap itself (without particle) is shown as grey solid lines for comparison. The instances A, B, C, and D from Figure 5.5 are indicated on the force spectra.

together to show how the coupling affects the resonance spectrum. The force spectra on the corresponding particles are shown together as dashed lines. The force spectrum is reversed in the vertical axis to make the comparison with the resonance spectrum easy. The instances A, B, C, and D from Figure 5.5 are also indicated on the force spectra.

Often the active involvement of the particle in optical trapping is described in the context of a self-induced back-action (SIBA) trapping [179]. For metallic particles, the SIBA effect can be even more prominent by changing the resonant response of the system itself. Figure 5.6 shows that the resonant response of the system is strongly modified by the presence of the trapped particle, especially when the particle size is comparable to that of the trap. The coupled system shows redshifts for all the instances investigated, which implies that the mode of the antenna is hybridized with that of the particle to lower the energy, forming a bonding mode [189]. In particular, depending on the strength of the coupling, the spectrum with the particle can remain similar (Figs. 5.6(a) and 5.6(b)) or become very different (Figure 5.6(c)) from that of the trap.

Most importantly, Figure 5.6 shows that the force spectrum follows the spectrum of the coupled system, rather than that of the sole antenna. This gives evidence on the active involvement of the particle in trapping. For more detailed analysis, we study the distribution of the near-fields and surface polarization charges on the points indicated as A, B, C, and D in Figures. 5.5 and 5.6 in the following subsection.

Near-fields and polarization charges

The near-fields and polarization charges on the nanostructure surfaces show how the particle couples with the antenna. In particular, the polarization charges are typically a complex quantity, and we shall report both its real and imaginary parts since they together provide information about the phase shift between the incident light and the charge oscillations as well as the amplitude of the response [110]. For example, depending on the excitation frequency, a time-harmonic forced oscillator is not oscillating in phase with the driving force but lags by a certain amount of phase that becomes 90° on resonance. This 90° phase lag moves all the information to the imaginary part so that we must look at both the real and imaginary parts for accurate analysis.

Figure 5.7(a) shows the near-field amplitude distribution around the antenna and a 20 nm particle when the force is maximum at $\lambda = 790$ nm. The incident field amplitude was set to be 1 for all the near-field plots so that the field amplitude can also be read as amplitude enhancement factor. The field distribution is similar to that without the particle in Figure 5.1(b). This implies that the field disturbance caused by the particle is not significant, which we already confirmed in the previous section through the comparison of the force between the two approaches. It is also clear from Figure 5.6(a) that the inclusion of the particle to the system shows very little change in the resonance spectrum. The dipolar charges on the particle surface on the right side of Figure 5.7(a) prove that the dipole approximation is valid for this size. In addition, the

imaginary part of the complex charge dominates over the real part, which tells us that the system behaves simply like a driven oscillator.

The optical force then reaches its local maximum at the particle size of 100 nm, and the corresponding fields and polarization charges are shown in Figure 5.7(b). They show that the larger particle has a stronger coupling with the antenna. Particularly, in the near-field plot, the field is intensely localized at the gap between the particle and the antenna. In the charge plot, on the other hand, the particle is still polarized like a dipole, but it has a higher charge density closer to the antenna. This is indicative of an attraction of opposite charges between the particle and the antenna, which can also be interpreted as optical binding [201, 202]. The resonant wavelength of maximum force is also shifted from 790 nm to 805 nm as a result of the strong coupling.

As the particle size further increases, the optical force enters a new phase: its magnitude becomes much more extensive, and the force sign changes from negative (attracting the particle) to positive (pushing it away) depending on the incident wavelength of light. For example, the force magnitude exerted on a 200 nm particle is approximately 4 times larger than that on a 100 nm particle at each investigated points (the points B and C in Figure 5.5).

The near-field and charge plots for the antenna with a 200 nm particle in Figs. 5.7(c) and 5.7(d) offer some insights into the underlying physics of these complex phenomena, and they have many interesting points to address. First of all, Figure 5.7(c) shows that the particle couples with the antenna in a way that reinforces the antenna resonance; the factor of near-field amplitude enhancement reaches up to 50 (not obviously shown in the plot due to the uniform color bar scale), and the polarization charge magnitude is also larger compared to the other cases with the smaller particles. The charge plots on the right side of Figure 5.7(c) also illustrate that the charges on the particle surface develop into a more complicated way, showing asymmetric multipole modes. The charges especially tend to concentrate on the side closer to the antenna and form the inverse mirror image on that face. This peculiar behavior of the charges may explain the extraordinary force that attracts the particle towards the antenna, which may also be understood as optical binding induced by the intense optical near-fields. Lastly, the real part of the charge now becomes comparable to its imaginary part. It implies that the particle and the antenna form a compound system, which is not anymore like a simple harmonic oscillator [110].

On the contrary, Figure 5.7(d) shows the field and charge plots for the particle of the same size, 200 nm, but when the antenna is out of resonance, i.e., the incident wavelength is $\lambda = 920$ nm. At this wavelength, the antenna does not produce significant near-fields, which means that the gradient force would not be strong enough to trap the particle. At the same time, the scattering force acting in the direction of propagation scales up with the particle size since in first approximation it is proportional to the scattering cross-section. As a result, the net force, which is the sum of the gradient and scattering forces that are opposite each other, can push the particle away.

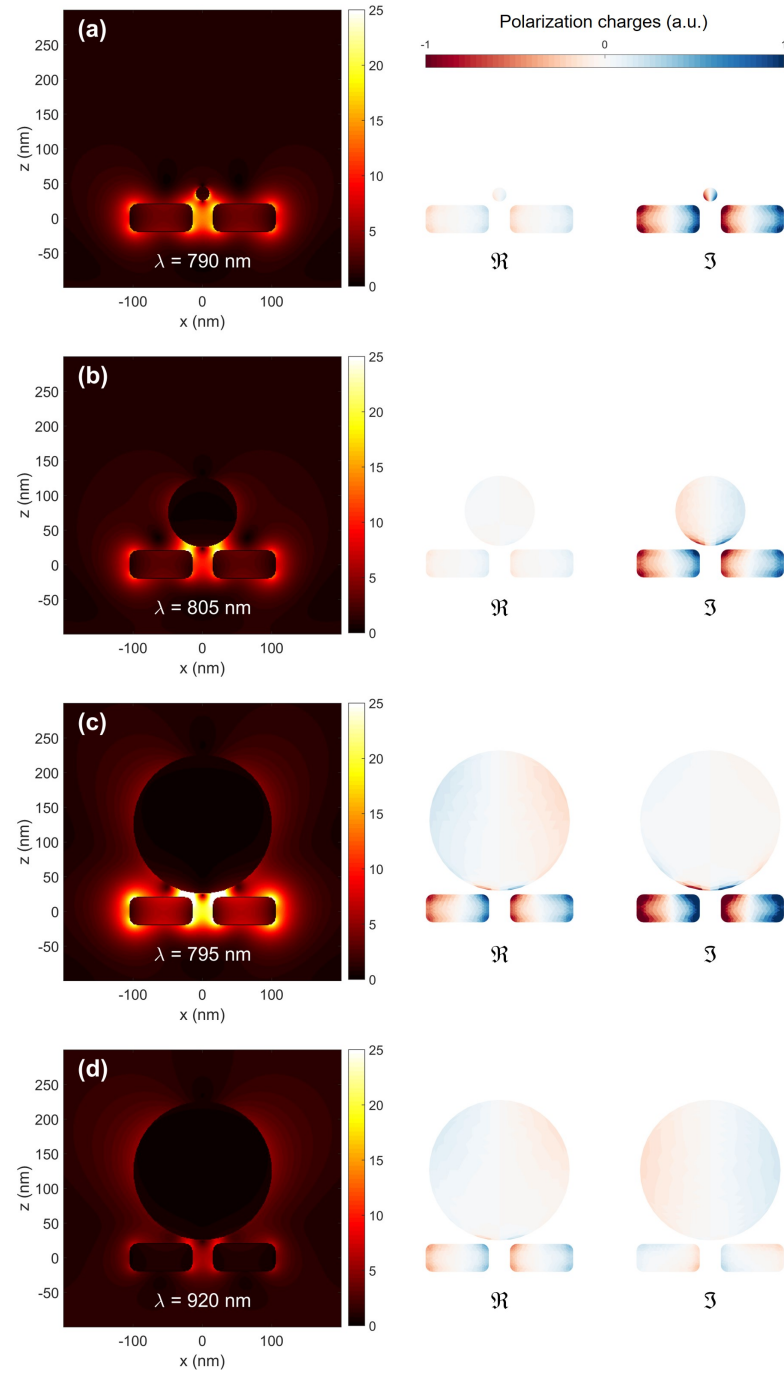


Figure 5.7 – (Left) Near-field amplitude distributions and (Right) real \Re and imaginary \Im parts of the polarization charges on the nanostructure surfaces. The parameter sets marked as A, B, C, and D in Figure 5.5 are analyzed to represent different coupling regimes. (a) Nanoparticle diameter $\delta = 20$ nm and incident wavelength $\lambda = 790$ nm; (b) $\delta = 100$ nm and $\lambda = 805$ nm; (c) $\delta = 200$ nm and $\lambda = 795$ nm; (d) $\delta = 200$ nm and $\lambda = 920$ nm.

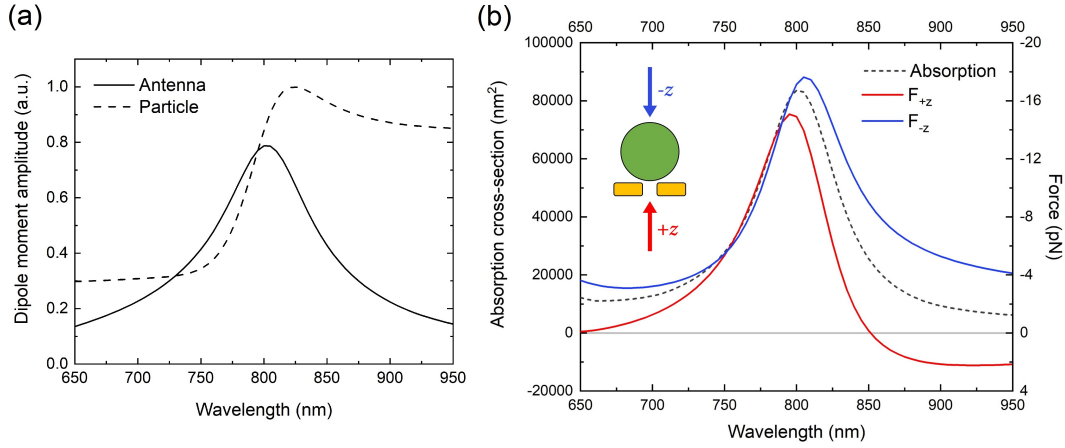


Figure 5.8 – Origin of the repulsive force. (a) Dipole moment amplitudes of the antenna (solid line) and the 200 nm particle (dashed line). (b) Force exerted on the 200 nm particle with two different illuminations: the light propagating $+z$ and $-z$ directions (red and blue solid lines). The absorption cross-section of the total system with the 200 nm particle (black dashed line).

Contribution of the scattering force acting on a particle

Figure 5.8 makes this argument more convincing. Figure 5.8(a) shows the dipole moment amplitudes for the antenna and the particle, computed from their surface polarization charges. The antenna's dipole moment has a maximum at $\lambda = 800$ nm where the antenna is on resonance. On the contrary, the particle's moment remains large for longer wavelengths. So at $\lambda = 920$ nm, which is the wavelength used in Figure 5.7(d), the incident light mainly interacts with the particle, and therefore, the scattering force is likely to dominate the net force. In addition, if we compute the scattering force acting on the 200 nm particle in the absence of the antenna under the same conditions, the force become 2.3 pN; this value is very close to the total force obtained from the computation with the antenna, which is 2.2 pN.

On the other hand, Figure 5.8(b) shows the force spectra on the 200-nm particle for two different illumination directions as well as the spectral response of the total system. The force spectra (the blue and red lines) are reversed in the vertical direction to make the comparison with the system response easier. So far, the light is incident in the $+z$ direction so that the scattering force is in the direction of pushing the particle away from the antenna. If the light is incident in the $-z$ direction such that the scattering force also pushes the particle toward the antenna as the gradient force does (the inset of Figure 5.8(b)), we expect that the repulsive behavior will disappear. The blue line in Figure 5.8(b) shows the force spectrum for this case and we do not see any repulsive force.

Another interesting point in Figure 5.8(b) is that the force spectrum deviates from the spectrum of the absorption cross-section of the system (the black dashed line) in the opposite way depending on the direction of illumination. In this way, we can observe the contribution of

the scattering force according to whether it is additive or subtractive to the gradient force.

5.3 Conclusion

We have compared the MST method with DA for force calculations to study how the interaction between a metallic particle and a trapping plasmonic dipole antenna influences the optical force. Quite surprisingly, and in spite of the strong coupling between both structures, the DA method still works very well, especially particles smaller than 15 nm. The discrepancy between the two approaches become noticeable for extreme cases, for example, when the antenna is on resonance, and the particle is in the location of high-intensity fields. In most cases, however, the DA method remains accurate and reliable. Besides that, we have studied the optical force in systems with larger particles, whose sizes are beyond the range of the dipole approximation. We have found different coupling regimes with large particles, where the particle polarization is much more complicated than a simple dipole. The force in such an intricate system has shown either attractive or repulsive behaviors depending on the excitation conditions, and the distribution of polarization charges on the structures at hand explain well these behaviors.

6 Plasmonic assemblies realized by optical manipulation

A part of this chapter is in preparation for publication in a peer-reviewed journal.

6.1 Introduction

Optical tweezers are an extremely useful tool to grab, move, arrange, and assemble small objects in the microscopic world in a similar way that human hands can [11, 16, 203, 204]. With their general ability to manipulate matter, optical tweezers hold a unique position when it comes to manufacturing at the nanoscale [13]. If an optical tweezer can place an object precisely where we want, we can utilize it to realize nanoscale additive manufacturing. For instance, it can be used to create a three-dimensional architecture by incorporating an element into a planar device fabricated by top-down lithographic processes. As Richard Feynman stated in his famous lecture, *“there is plenty of room at the bottom.”* [1]

In this final chapter, we will look at the use of optical tweezers from that perspective. In particular, we will investigate how the optical response of a nanostructure can be altered by introducing a new element into the system. Plasmonic nanoantennas and nanoparticles are excellent candidates for investigating this effect [86]. They can be resonantly excited with visible light, resulting in strong near-fields that can be used in a variety of applications such as Raman spectroscopy [205, 206], biosensing [82, 207], photocatalysis [208, 209], and photovoltaics [78, 79]. When the near-fields of two independent systems are brought close together and overlap, they interact strongly and, in some cases, completely transform the manner in which they interact with light [84, 210–212]. This fascinating phenomenon can be used to engineer the optical response of a system, transforming nanostructures into “tailor-made” materials suitable for diverse applications. Optical tweezers can provide an unprecedented way to realize this concept by hierarchically assembling a coupled system on demand.

Figure 6.1a illustrates the optical system that will be studied in this chapter. Inspired by plasmonic oligomers [211, 213–215], which are artificial molecules made up of nanoparticles, we considered a ring-type hexamer (a plasmonic analog of a benzene molecule) that can

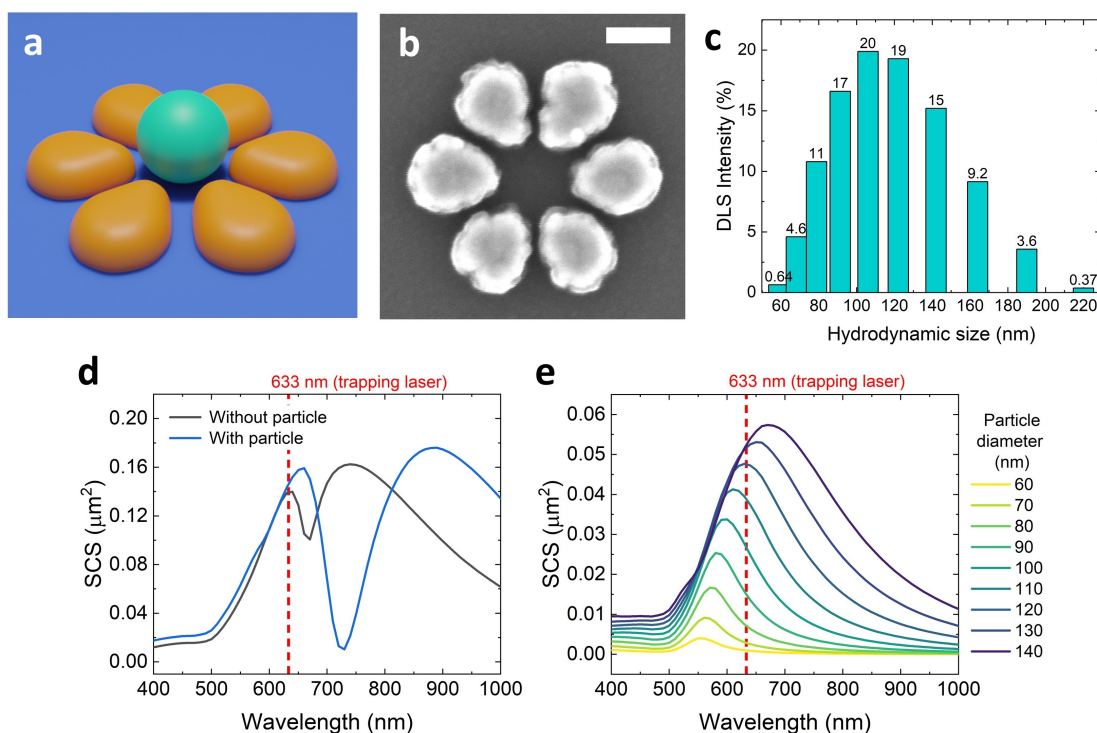


Figure 6.1 – Nanoflower trapping. **a**, Schematic picture of a nanoflower and a nanoparticle trapped at the center. **b**, Scanning electron microscope (SEM) image of a fabricated nanoflower (top view). Scale bar, 100 nm. All credit to Robert Wolke (a former member of the Nanophotonics and Metrology Laboratory) for nanofabrication. **c**, Size distribution of colloidal nanoparticles used for trapping experiments. This probability distribution of hydrodynamic size was determined by the intensity of dynamic light scattering (DLS). **d**, Optical scattering cross sections (SCS) numerically calculated for a nanoflower with and without a particle (100 nm). **e**, Optical SCSs computed for different particle sizes ranging from 60 to 140 nm.

be converted to a heptamer by introducing a central particle inside the ring. The resonant coupling transition from a hexamer to a heptamer was studied by Hentschel *et al.* [213]; they measured the extinction spectrum of large hexamer and heptamer arrays fabricated by electron-beam lithography and experimentally demonstrated the emergence of a dark Fano resonance [211] with the introduction of the central particle.

With this well-studied example, we demonstrate the possibility of optical tweezers to provide a bridge between lithographically defined structures and chemically synthesized colloidal particles. Starting with a lithographically fabricated nanostructure (Figure 6.1b), which we refer to as a *nanoflower* because of its flower-looking shape, we trap a colloidal gold nanoparticle inside the nanoflower, resulting into a modest three-dimensional profile due to the relatively flat nanoflower (40 nm thickness) and the spherical colloidal particle (100 nm in diameter on average) as well as an interesting spectral change (Figure 6.1d). Unlike structures that are entirely defined by the lithographic process, structures assembled by the optical tweezer contain inherent variances. Hence, we theoretically investigate various particle–flower coupling scenarios caused by variance in colloidal particle size and uncertainty in particle position. To this end, we introduce a coupled oscillator model in order to quantify the optical coupling between particle and nanoflower in simulation results. Finally, this model is applied to experimental data to better comprehend optical coupling in measured spectra.

6.2 Materials and methods

6.2.1 Gold colloids

We obtained gold nanoparticles in a citrate buffer with an average diameter of 100 nm from Sigma-Aldrich. Following the method described in Section 2.2.4, dynamic light scattering was used to determine the gold colloids' size distribution. The result is shown in Figure 6.1c, which follows a well-known log-normal distribution [216].

6.2.2 Fabrication of nanoantennas

The procedure detailed in Section 2.3 was used to create the nanoantenna structures. As a side note, besides the nanoflower geometry studied throughout this chapter, we also investigated the dipole antenna structures that were the subject of Chapter 5. The 30 nm gap size of the dipole antenna was much smaller than the particle size used in this study. There were three hot spots on the antenna, one in the gap and two at the ends of the arms. Even though these three hot spots were the likely trap positions [184], we discovered that after a particle was trapped, it moved around among these spots. This is possibly because, in relation to the size of the antenna, these hot spots are situated so close that the particle can jump from one hot spot to the other. When compared to the one without the antenna structures, this led to exceedingly unstable trapping of particles.

On the contrary, the nanoflower structure features a pocket at the center that can accommodate a particle within its structure. Figure 6.1b shows an electron micrograph of a realized structure using e-beam lithography. The optical force exerted on a particle around the nanoflower will be discussed in the results and discussion section.

6.2.3 Trapping experiments

We used the identical optical trapping setup in Section 2.2.2. The He-Ne laser power was set to 16 mW before the entrance pupil of the trapping objective, which was the maximum output of the laser at the power-measurement plane.

The particle solution and fluidic chambers were prepared in accordance with Section 2.2.1. The only distinction was the nanoflower arrays fabricated on the chamber's bottom wall. The particles were either captured directly on the nanoflower or captured on a neighboring glass surface before being transported to the nanoflower using the piezo-electric stage. For colloidal stability, CTAC, a cationic surfactant, was added to the particle solution to reach a 1 mM concentration.

6.2.4 Spectral measurements

To investigate the interactions between nanoflowers and trapped particles, the optical spectra of individual antennas were measured before and after particle trapping. For spectral measurements, we used a spectrograph (Andor Shamrock 303i) connected to a side port of the imaging microscope and a spectroscopic CCD camera (Andor iDus 401, DU401A BR-DD). We initially measured the spectra of each nanoflower immersed in the particle solution under white light illumination (a halogen lamp). Next, we switched the trapping laser on and recorded the trapping process with an imaging CMOS camera. Due to the resolution of the optical microscope, it was difficult to determine whether or not particles remained within nanoflowers after they were trapped. The spectrum of each antenna measured again after the trapping trials helped validate the existence of a particle.

6.3 Results and discussion

6.3.1 Trapping nanoparticles within a nanoflower

Let us assume that we grab a particle and deliver it to a nanoflower with an optical tweezer. Will the particle be attracted toward the nanoflower's central void, as illustrated in Figure 6.1a? How would the particle behave in the near-fields of the nanoflower? To answer these questions, we calculated the optical force exerted on a particle while it was in close proximity to a nanoflower. Given that we used particles with an average size of 100 nm, the dipole approximation may not be applicable in this case [72]. Therefore, to figure out the optical force numerically, we used the the Maxwell's stress tensor (MST) method. For all the force calculations, the light was

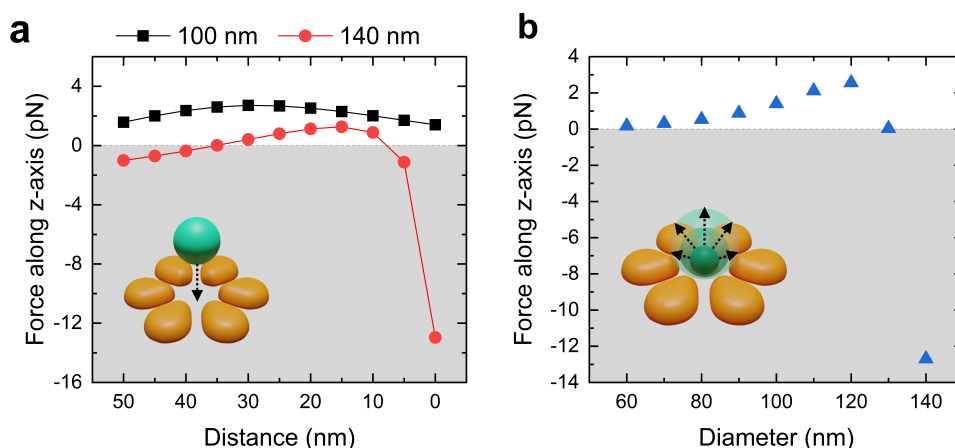


Figure 6.2 – Computed optical force along the z -axis while varying the particle's height (a) or its diameter (b). The distance in a refers to the distance between the particle's bottom surface and the glass surface at the center of the nanoflower. In the case of b, the particle's bottom surface is fixed to the glass surface. The excitation field was incident from the top and had a wavelength of 630 nm, corresponding to the trapping laser wavelength.

incident from the top to the bottom at the wavelength of 630 nm to simulate the experimental trapping configuration.

We started by placing a particle along the z -axis in a three-dimensional space with a nanoflower resting on the x - y plane and with the origin at the center of the nanoflower. We varied the distance between the particle's bottom and the glass surface from 50 to 0 nm, bringing the particle down to the central space. The force calculated along the z -axis is shown in Figure 6.2a. We considered two different particle sizes, 100 nm and 140 nm. Interestingly, the vertical force acting on the 100 nm particle was always positive, pushing the particle upward. The 140 nm particle, on the other hand, encountered a sudden attractive force when the distance became less than 10 nm.

Such a size-dependent force is reminiscent of the optical force examined in Chapter 5 near the dipole antenna. Figure 6.2b depicts our subsequent examination of the optical force while varying the particle size. We fixed the particle's bottom to the x - y plane and increased the particle diameter from 60 nm, the smallest size observed in the DLS size distribution, to 140 nm, the largest size that can fit within the nanoflower's central space. Figure 6.2b reveals that the force stays repulsive (positive) up to a size of 120 nm, after which it declines abruptly. This behavior differs significantly from that of the dipole antenna. We recall from Chapter 5 that the force of repulsion was caused by the momentum transfer of light traveling in the opposite direction. For the calculations in Figure 6.2, however, the light was incident from the top to the bottom, such that the scattering force also pushed the particle toward the nanoflower. The scattering force is also proportional to the size of the particle, and thus it cannot explain the growing repulsive force for particle sizes between 60 nm and 120 nm.

Examining their resonant coupling to an external excitation may shed light on this behavior. Going back to Figures 6.1d and e, we can find the wavelength of the trapping laser indicated as vertical dashed lines on top of the resonant spectra. According to Figure 6.1d, the laser wavelength is shorter than the nanoflower's resonance peak. In the case of the particles, however, this wavelength can be shorter or longer than the particle's resonant wavelength depending on its size. For particles larger than 120 nm, the laser wavelength is shorter than the resonant wavelengths for both the particles and the nanoflower. This suggests that the light-induced oscillations of the electrons are more or less in-phase between the particle and the nanoflower, a condition in favor of bonding attractions [200, 211]. On the other hand, the increase in their phase difference for particles smaller than 120 nm can result in anti-bonding interactions rather than bonding ones. This interpretation supports the inversion of the force direction in Figure 6.2b for particles smaller than 120 nm in diameter.

To confirm this interpretation, we visualized the polarization charge distributions on the particle and nanoflower surfaces. Figure 6.3 shows the result with two different particle sizes: 100 and 140 nm. For the 100 nm particle, we observe that both the particle and the nanoflower are excited, but with opposite dipole moments: The particle is excited like a dipole, and the

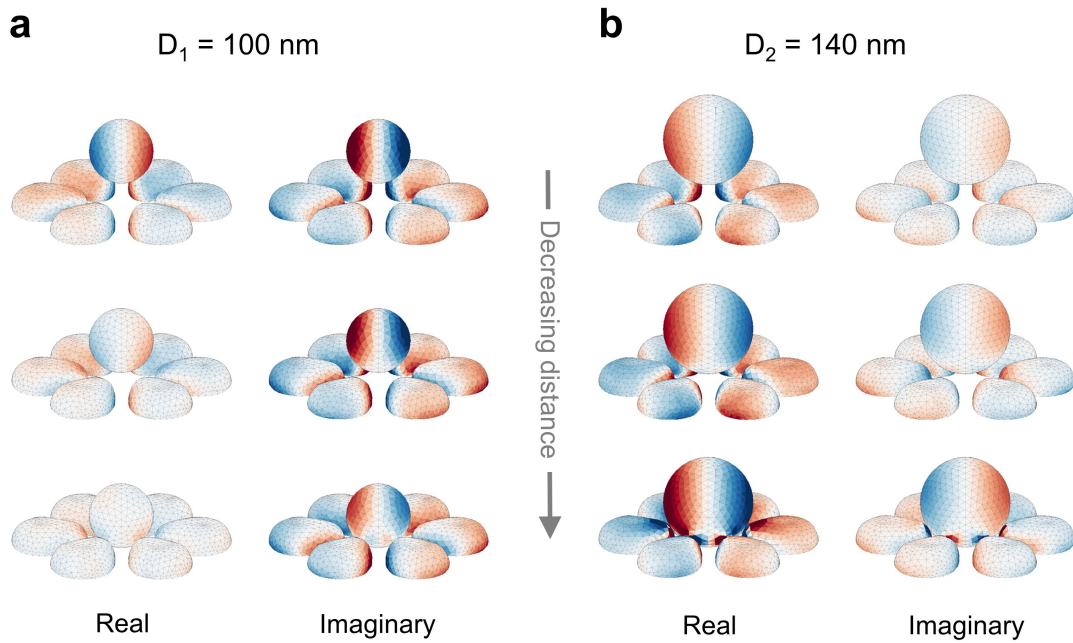


Figure 6.3 – Polarization charges on the surfaces of the coupled system (**a**, 100 nm and **b**, 140 nm particle diameters), while changing their distance to the nanoflower. The distances are respectively 50, 25, and 0 nm from top to bottom. Blue and red colors represent positive and negative charges, and the color scales indicate charge density. For comparison, the same color scales are applied to all plots (i.e., the same color represents the same value). Both real and imaginary parts of the polarization charges are shown together to deliver phase information.

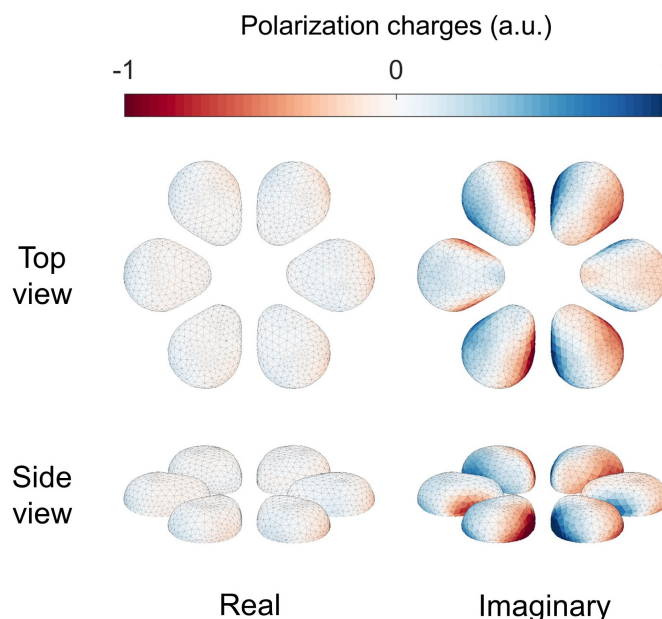


Figure 6.4 – Polarization charges on the nanoflower surfaces without a particle.

charge distribution of the nanoflower resembles that of the nanoflower without the particle, as depicted in Figure 6.4. As the particle approaches the nanoflower, local perturbations in the charge distribution at the particle's bottom are detected. With the exception of these local charge attractions, it appears that they are independently excited and, especially, out-of-phase with one another, confirming the idea of anti-bonding modes.

For the larger particle scenario depicted in Figure 6.3b, we observe substantial differences compared with the 100 nm particle, especially in the charge distribution on the nanoflower's surfaces. Compared to the charge distribution of the isolated nanoflower (Figure 6.4), this distribution appears drastically different and is strongly affected by the particle. This indicates that the particle controls the global charge behavior. Another noticeable difference with this larger particle is that the particle diameter (140 nm) is more than three times the height of the nanoflower (40 nm), creating a three-dimensional profile. This profile increases the complexity of the charge behaviors and reveals additional charge coupling along the vertical axis as illustrated in Figure 6.3b.

There is an additional distinction between 100 nm and 140 nm particles: As the particles approach the nanoflower, the amplitude of the charge separation decreases for the smaller particle while it increases for the larger particle. As depicted in Figure 6.5, this is much more noticeable when we examine the near-field distribution of the coupled system. These opposing trends in the near-fields support the bonding and anti-bonding modes and indicate whether the coupling is favorable or not. From these force calculations, we can conclude that the nanoflower structure is more likely to trap larger particles.

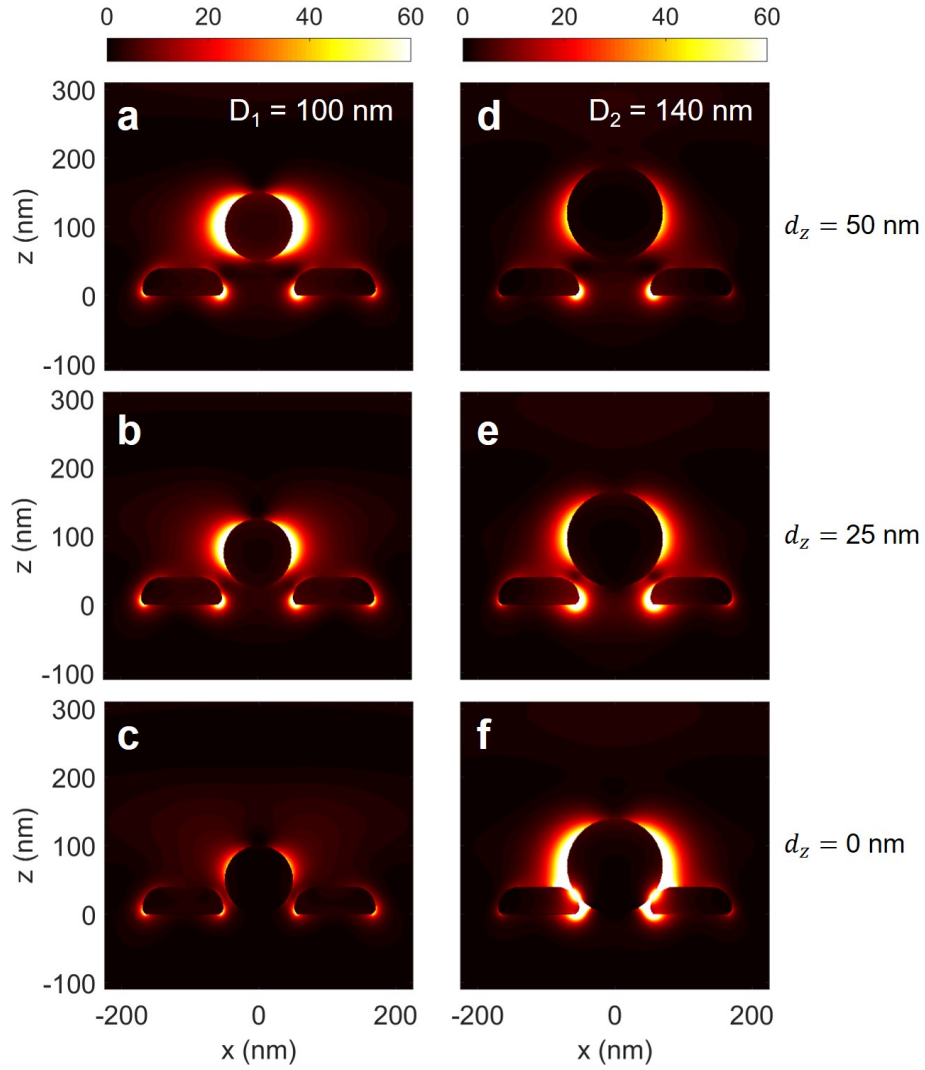


Figure 6.5 – Near-field intensity distributions for the two particles (100 nm diameter from **a** to **c** and 140 nm diameter from **d** to **f**) while changing their vertical location along the z -axis. The distance d_z refers to the distance between the particle's bottom surface and the glass surface. The particle touches the glass surface when $d_z = 0$.

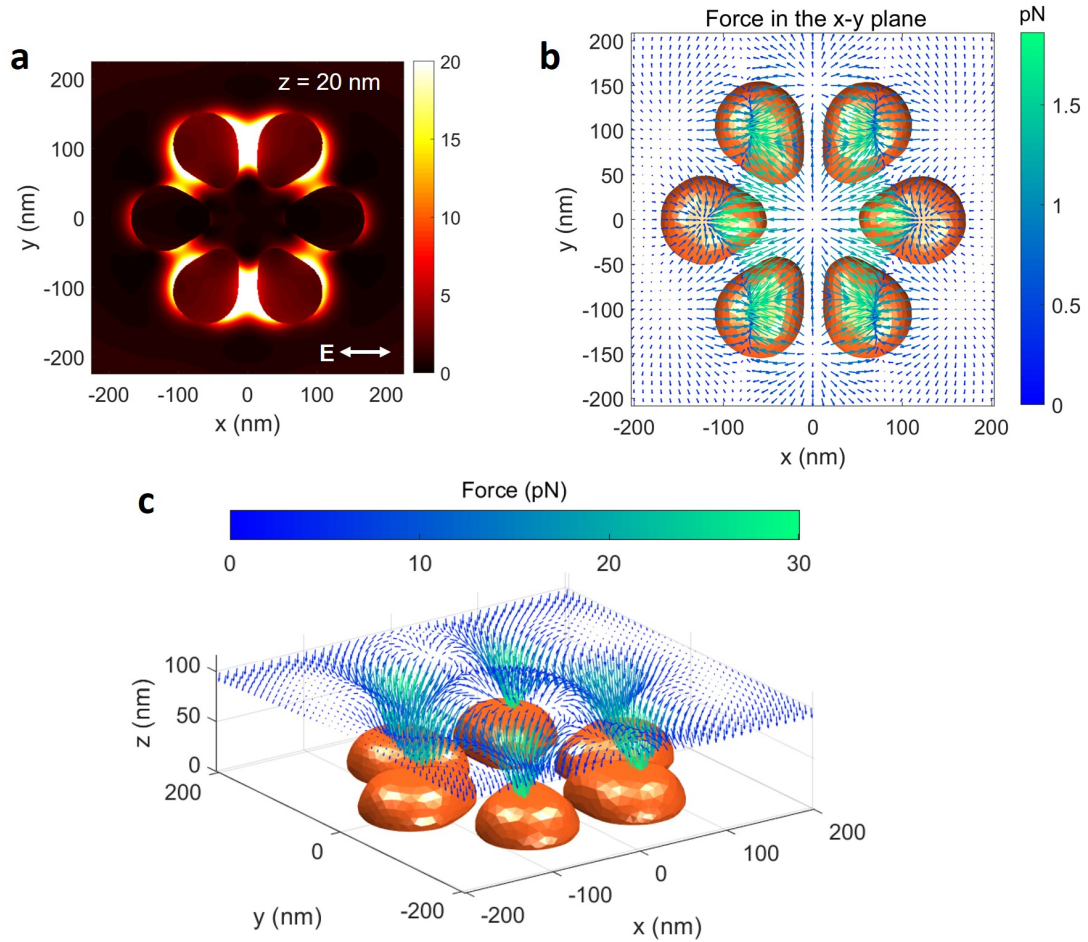


Figure 6.6 – Optical force exerted on a 100 nm nanoparticle located 5 nm above the nanoflower. **a**, Near-field intensity enhancements at the cross-section of a nanoflower parallel to the x - y plane ($z = 20$ nm). **b**, Optical force calculated by the Maxwell's stress tensor (MST) method by sweeping the position of a 100 nm gold nanoparticle (not shown) above the x - y plane. The gap distance between the nanoflower's top surface and the particle's bottom surface remains 5 nm. Only the force components parallel to the x - y plane (F_x, F_y) are shown as a two-dimensional (2D) vector plot. The force magnitudes are represented by both the colors and the lengths of the arrows. **c**, A three-dimensional (3D) vector plot for the same optical force, including the force along the z -axis (F_z). The incident light has a wavelength of 630 nm, propagating from the top to the bottom of the structure (along the $-z$ direction), polarized along the x axis for all the calculations in **a**, **b**, and **c**.

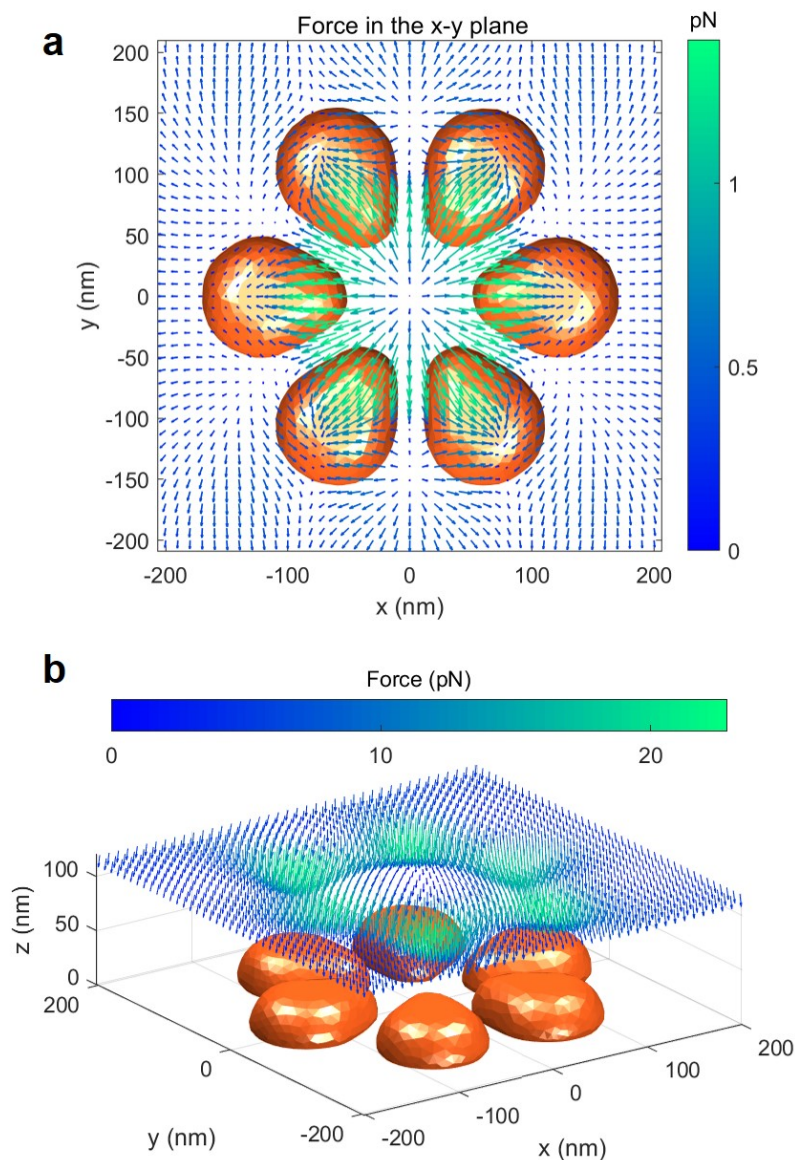


Figure 6.7 – Optical force exerted on a 140 nm nanoparticle located 5 nm above the nanoflower. **a**, 2D vector plot for the optical force. The particle geometry is included in the numerical calculation but omitted for legibility. **b**, 3D vector plot for the same optical force, including the force along the z -axis (F_z). Simulation conditions are the same as in Figure 6.6 except for the particle size.

So far, we have only observed the force along the vertical direction when the particle is at the central axis. We also calculated the force while sweeping the particle's x - and y -positions above the nanoflower. Figure 6.6 summarizes the result with a 100 nm nanoparticle located 5 nm above the nanoflower structure. Cross-sectional near-field intensities at the nanoflower's mid-height (at $z = 20$ nm) is shown in Figure 6.6a, where the incident field was polarized along the x -axis. Due to the narrow gaps between the petals (the upper and lower pairs), the field intensities are the strongest at those gaps. When we place the particle above the structure, the particle feels the force in the x - and y -directions as shown in Figure 6.6b, i.e., the particle is pushed toward the outer rim of the nanoflower. Specifically, the three-dimensional force representation in Figure 6.6c reveals that the particle is strongly attracted to each of the petals.

Figure 6.7 shows a similar result with the largest nanoparticle (140 nm) located 5 nm above the nanoflower. Comparing Figures 6.6 and 6.7, we find close similarities between the 100 nm and 140 nm particles in the way they feel forces near the nanoflower, in contrast to our earlier observation on the vertical forces, which revealed opposite behaviors for these two particles (Figure 6.2a). However, if this 140 nm particle happened to be in the exact center of the nanoflower where the forces in both x - and y -directions are balanced due to symmetry, the particle would only feel the downward force and could be trapped inside the nanoflower. This seems to be improbable for the 100 nm particle as it feels only the upward force even when it is in the center.

In actual experiments, the trapping laser is a focused beam rather than a plane wave. Since we simplified the incident beam as a plane wave in the simulation, there must be a discrepancy between the force calculated in the simulation and the force experienced by a particle. For example, the focused laser beam exerts a trapping force that must be superimposed on the force generated by the nanoflower's near-field. Furthermore, we can control the particle's position to some extent using the optical tweezer and the piezoelectric stage. When combined, they can increase the likelihood of particle trapping within the nanoflower structure, overcoming the simulation's diverting forces.

6.3.2 Experimental results

We performed trapping experiments with gold nanoparticles (100 nm diameter on average) and lithographically fabricated nanoflower arrays in order to observe a strong optical interaction between them. As depicted in Figure 6.8, we subtly modified the nanoflower configuration. In this figure, the inner pocket size increases from left to right by shortening the petal lengths while maintaining the overall dimension. After performing dozens of tests, we determined that the nanoflower with the smallest pocket (F1) was incapable of capturing particles, possibly because the particles were too large to fit in the central space. However, nanoflowers with medium (F2) and large (F3) pockets were able to trap particles and exhibited spectral changes after trapping. Therefore, we focus on the results with designs F2 and F3.

Figure 6.9 displays three example spectra for nanoflowers with the F2 configuration. It shows

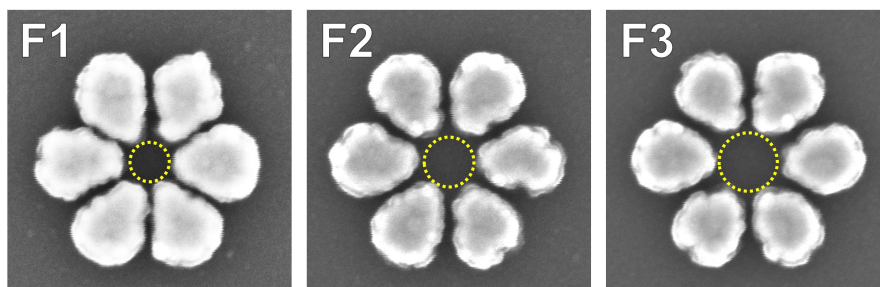


Figure 6.8 – SEM images of three nanoflower configurations with different pocket sizes. The inner pocket size increases from F1 to F3 by reducing the size of the petals while maintaining the overall dimension. The diameters of the pockets are respectively 65, 85, and 105 nm.

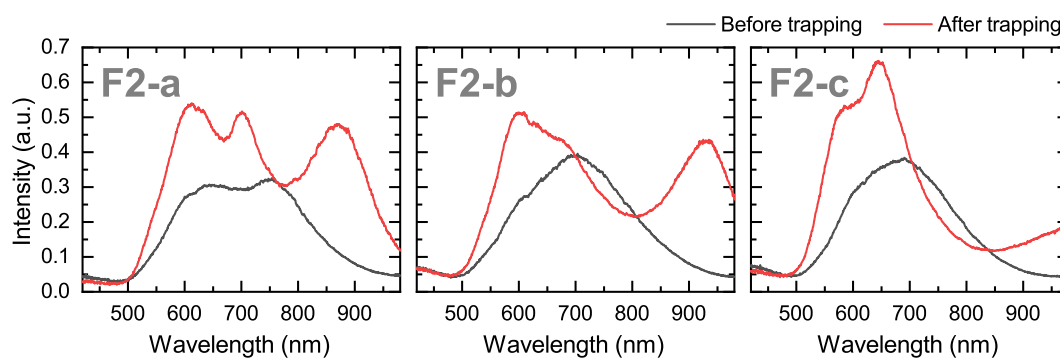


Figure 6.9 – Three example spectra from individual nanoflowers with the F2 design (F2-a, F2-b, and F2-c), comparing spectra before (gray) and after (red) particle trapping.

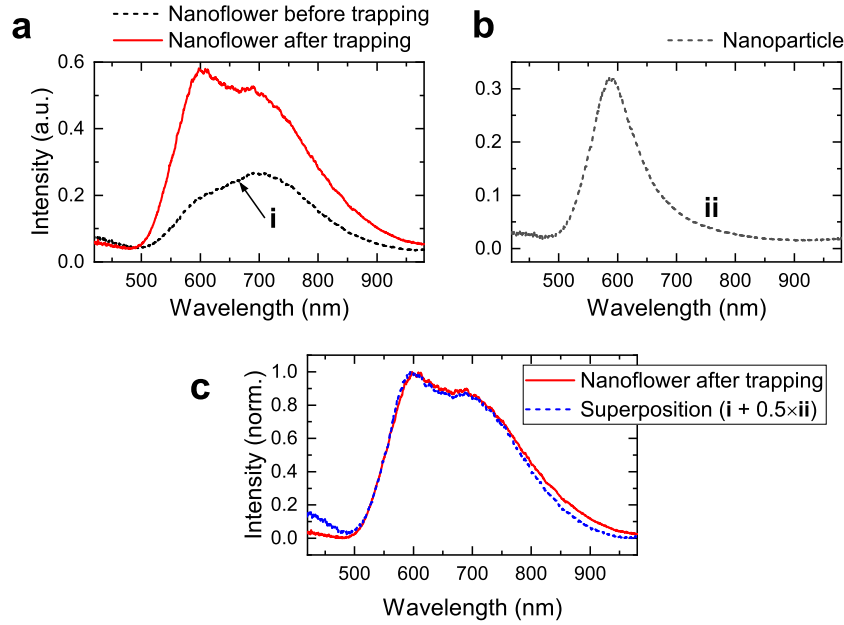


Figure 6.10 – Example spectrum with no spectral splitting after particle trapping. **a**, This example exhibits an overall enhancement, with a notable increase at around 600 nm after particle trapping. **c**, This change can be interpreted as the absence of coupling, where the coupled spectrum can be reproduced by a simple superposition of the nanoflower (**i** in **a**) and nanoparticle (**ii** in **b**) spectra.

spectra from individual nanoflower measurements before and after particle trapping, clearly demonstrating a spectral transition due to the flower–particle coupling. However, not every trapping experiment produced a prominent transition. Only four of the 32 trapping measurements from this batch of F2 arrays exhibited such a significant difference; the rest showed overall signal increases or more pronounced enhancements at shorter wavelengths (600–700 nm), as illustrated in Figure 6.10a. We discovered that this enhancement at approximately 600 nm can be reproduced by a simple superposition of the nanoflower measurement without a particle and that of a separate nanoparticle, as shown in Figure 6.10c. This suggests that the coupling between the particle and the nanoflower is negligible for this measurement, which could be the case when the particle is fixed outside at a distance from the nanoflower (roughly more than 300 nm from the nanoflower center based on calculations).

In order to understand the odds against a strong coupling, we should consider the necessary conditions for strong coupling. First, the particles should be contained within the nanoflowers' centers. Suppose it is trapped elsewhere, such as on top of a petal or on the outside of the nanoflower. In that case, it is only coupled to a portion of the nanoflower's structure, from which we cannot expect the same effect as when the particle interacts with all the petals and forms an ensemble. Second, the particles should be large enough to fill the central space. Figure 6.11 depicts how the spectral splitting evolves as particle size increases. This simulation result demonstrates that the larger particle induces a more pronounced spectral shift. On

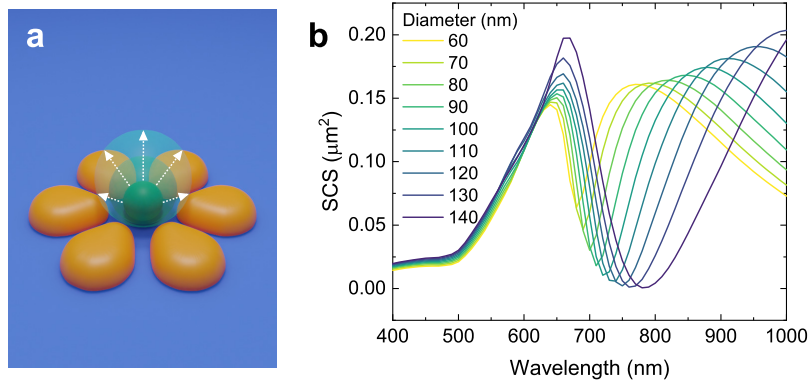


Figure 6.11 – Spectral variation of the nanoflower–particle system while increasing the particle diameter. **a**, Drawing of the configuration. **b**, Scattering cross-section when varying the diameter of the particle from 60 to 140 nm.

top of that, we observed repulsive force in the force calculation for particles smaller than 130 nm. This vertical repulsive force may have made it difficult to trap smaller particles. With these arguments, we can understand the low probability of strong coupling as a result of the interplay between the inherent variance in particle size in the colloidal dispersion (Figure 6.1c) and the disturbance in particle position due to random thermal movements or repulsive force generated by the nanoflower’s near-field.

Figure 6.12 illustrates three additional examples with the F3 configuration. They were chosen from a total of 64 trapping measurements. The likelihood of achieving a strong coupling was slightly higher with the larger pocket size (10 out of 62). The rest of this measurement set showed diverse transitions: Some exhibited an increase in the overall signal strength or a more pronounced enhancement at the particle resonant wavelength, similar to the F2 design. Others showed unexpected spectral changes, possibly due to broken symmetries when particles are trapped not exactly at the center. Another noticeable difference is that the F3 designs have a narrower spectral splitting than the F2 designs for those showing prominent

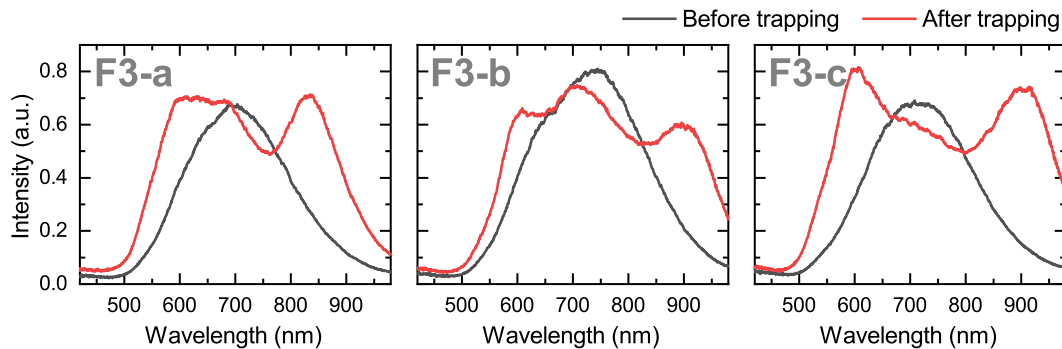


Figure 6.12 – Three exemplary spectra from individual nanoflowers with the F3 design (F3-a, F3-b, and F3-c), comparing spectra before and after trapping nanoparticles.

transitions, possibly implying a weaker coupling with a larger pocket size.

6.3.3 Coupled oscillator model

We have looked at several examples of experimental results. However, these experimental results clearly diverge from the simulation results observed previously. Simulations allow precise control over the size and location of particles, whereas experimental results do not reveal such information. Consequently, it is challenging to determine which factors account for the differences between experiments and simulations. In order to comprehend these experimental findings in-depth, we will investigate this problem using the well-known coupled oscillator model. We will first search for model parameters that can express the simulated and measured spectra. Then, instead of comparing spectra themselves, these parameters will be compared to gain a quantitative understanding of the optical coupling in flower-particle systems.

Single forced oscillator with damping

The free electron cloud in a metallic nanostructure is bound by its geometry. This geometrical boundary exerts a restoring force when the electrons are displaced by an external force. With an oscillating force, the electron cloud oscillates back and forth like a mass on a spring. Therefore, the resonance spectrum of a plasmonic nanoparticle can be modeled as that of a forced oscillator with damping. In this case, the driving force can be an external electromagnetic wave, and the damping process can be attributed to both radiative damping (i.e., the transformation of particle plasmons into photons) and non-radiative damping (i.e., energy dissipation through collisions and release of heat).

To model a single nanoparticle, we begin with the equation of motion of a damped oscillator with mass m_P (the subscript P stands for particle, and we use it to distinguish it from nanoflower parameters for that will be discussed later):

$$m_P(d^2x/dt^2) + c_P(dx/dt) + k_Px = F, \quad (6.1)$$

where x is a displacement of the oscillator, $c_P(dx/dt)$ is a friction term proportional to the velocity, k_Px is a restoring force proportional to the displacement, and F is an external driving force. Dividing out the mass m_P and writing $c_P/m_P = \gamma_P$ and $k_P/m_P = \omega_P^2$, Equation 6.1 becomes

$$(d^2x/dt^2) + \gamma_P(dx/dt) + \omega_P^2x = F/m_P. \quad (6.1a)$$

Suppose that the driving force F is a linearly polarized light with a frequency ω , i.e., $F = \hat{F}e^{i\omega t}$

and consequently $x = \hat{x}e^{i\omega t}$. Then Equation 6.1a would become

$$[(i\omega)^2 \hat{x} + \gamma_P(i\omega) \hat{x} + \omega_P^2 \hat{x}]e^{i\omega t} = (\hat{F}/m_P)e^{i\omega t}. \quad (6.2)$$

If we divided by $e^{i\omega t}$ on both sides, we would obtain the complex response \hat{x} to the given force \hat{F} :

$$\hat{x} = \frac{\hat{F}/m_P}{\omega_P^2 - \omega^2 + i\gamma_P\omega}. \quad (6.3)$$

By multiplying its complex conjugate, we get the square of the magnitude. This quantity corresponds to the signal intensity (I) that we obtain in spectral measurements:

$$|\hat{x}|^2 = \frac{\hat{F}^2/m_P^2}{(\omega_P^2 - \omega^2)^2 + \gamma_P^2\omega^2} \propto I. \quad (6.4)$$

Equation 6.4 considers a mechanical oscillator with mass m_P and external driving force amplitude \hat{F} . For a single charge q , the force becomes $q\hat{E}$ and the numerator in Equation 6.4 thus involves q and \hat{E} . However, in practice, the signal intensity also depends on measurement conditions such as the exposure time of a spectral measurement and the slit width of the spectrometer. Therefore, we simplify the numerator just as A_P for the measured signal intensity I :

$$I = \frac{A_P}{(\omega_P^2 - \omega^2)^2 + \gamma_P^2\omega^2}, \quad (6.5)$$

which we use for modeling the response of a single nanoparticle resonance, both for simulation and measurement.

Figure 6.13 illustrates the results fitted to particle responses using Equation 6.5. The particle response in **a** was obtained by simulating a gold sphere of 100 nm diameter in a uniform background whose dielectric permittivity was the average of that of the glass and water [217]. The particle response in **b** was obtained by measuring a random particle stuck on the glass substrate during a trapping experiment. The fitting range of the spectrum was between $\lambda = 500$ and 1000 nm. We chose this region because the scattering spectrum has a shoulder below 500 nm, as seen in both **a** and **b**. The reason for this shoulder is the interband excitation of electrons, which refers to the transition of electrons from the d band to the conduction band in metals; the corresponding threshold energy for gold is 2.38 eV or about 520 nm [218]. The oscillator model does not account for this interband transition, so the response below 500 nm was excluded from the fitting.

We estimated the three parameters (ω_P^2 , γ_P , and A_P) in Equation 6.5 for the results in Figure 6.13. The first parameter ω_P^2 refers to the squared resonant frequency of the system, which is directly related to the peak wavelength in the spectrum. The second parameter γ_P refers to the damping of the particle plasmon and can be related to the spectral width at the half

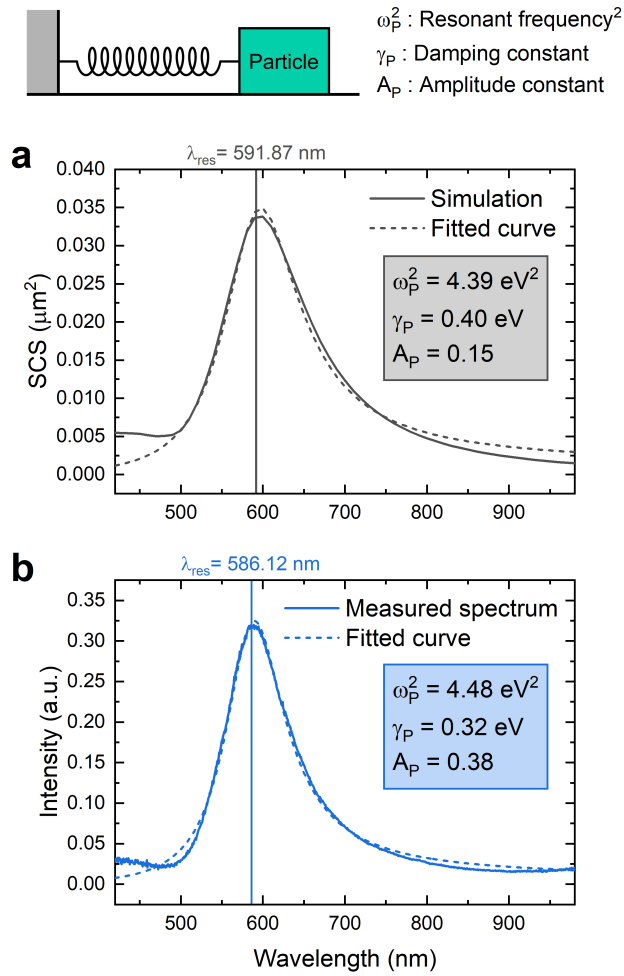


Figure 6.13 – Single particle response modeled with a forced harmonic oscillator with damping. **a**, Numerical simulation for 100 nm gold nanoparticle (solid line) and its fitting result (short dashes). **b**, Experimental measurement for a gold nanoparticle stuck on a glass substrate (solid) and its fitting result (short dashed). The responses below $\lambda = 500 \text{ nm}$ were excluded in the fitting process due to the high absorption of gold.

maximum. The last parameter A_P corresponds to the amplitude of the spectrum but has no physical significance as it is dependent on the measurement (or simulation) conditions.

The fitting results in Figure 6.13 demonstrate that the harmonic oscillator model successfully represents the particle's spectral response. Furthermore, the simulation fitting in **a** and the measurement fitting in **b** has a good agreement in ω_P^2 and γ_P , providing strong evidence that the simulation and measurement results are complementary to each other.

On the basis of this understanding, we extend the concept of a single harmonic oscillator to coupled oscillators, in which two or more oscillators are “connected” to influence one another. Our ultimate objective is to use these coupled oscillators to represent a system consisting of a nanoflower and a nanoparticle and investigate the coupling behaviors.

Two coupled oscillators

A nanoflower's spectrum has a characteristic that distinguishes it from that of a single oscillator. As shown in Figure 6.15b, it features a shallow dip near the resonance peak. To describe this suppression in scattering, we introduced the idea of interference between two modes, which is well known as Fano interference (Figure 6.14 for more details). In optical systems, Fano interference can arise when a broad resonant mode interferes with a narrow resonant mode. These broad and narrow resonant modes can be modeled as oscillators with strong and weak

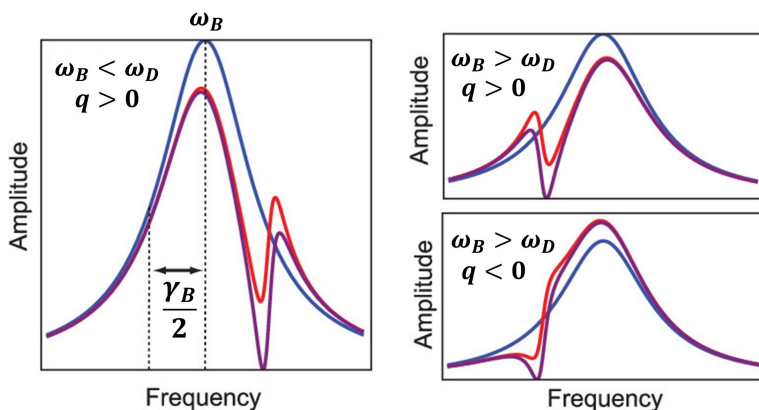


Figure 6.14 – Fano interference in optical systems. The broad scattering amplitude (blue) shows a slow phase development by π , and a narrow one exhibiting a sudden phase jump of π . The interference between these two amplitudes results in an asymmetric lineshape (purple and red) due to constructive interference (where the total scattering becomes larger than the broad scattering) and destructive interference (where the total scattering becomes smaller than the broad scattering). The broad state has a high damping (= scattering), so we refer to it as the bright mode. In the same manner, we refer to the narrow state as the dark mode. The constant q refers to the Fano parameter appearing in the original Ugo Fano's formula [219], which describes the asymmetric shape. Adapted with permission from Ref. [48]. Copyright 2011 American Chemical Society.

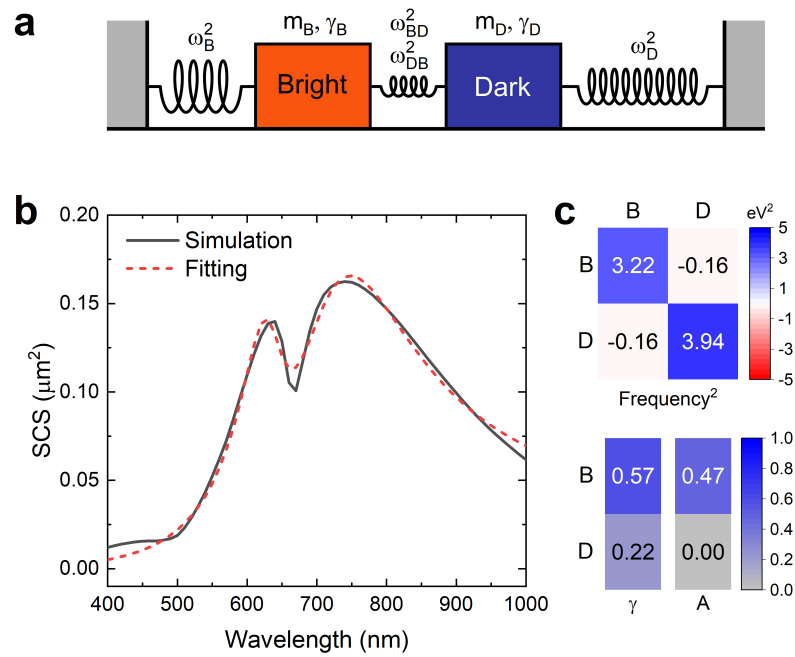


Figure 6.15 – Nanoflower response modeled with two coupled oscillators. The concept of Fano resonance was introduced, which assumes interference between a bright mode (one that is excited externally and scatters resonantly) and a dark mode (one that is excited via near-field and does not scatter into the far field). **a**, Two-coupled oscillator model and its parameters. **b**, Spectral response of a nanoflower and that reproduced by the coupled-oscillator model. **c**, Parameters used to plot the fitted curve in **b**.

damping. Since we are concerned with the scattering response, the principal damping process is radiative damping. Thus, we refer to the response of the oscillator with strong radiative damping as a “bright” mode and that of the oscillator with weak radiative damping as a “dark” mode.

Assuming that these bright and dark oscillators are connected by a spring as depicted in Figure 6.15a, we can formulate the equations of motion for the two modes:

$$\frac{d^2 x_B}{dt^2} + \gamma_B \frac{dx_B}{dt} + \omega_B^2 x_B + \frac{g}{m_B} (x_B - x_D) = \frac{F}{m_B}, \quad (6.6a)$$

$$\frac{d^2 x_D}{dt^2} + \gamma_D \frac{dx_D}{dt} + \omega_D^2 x_D + \frac{g}{m_D} (x_D - x_B) = \frac{F}{m_D}, \quad (6.6b)$$

where the subscripts B and D stand for the bright and dark modes, respectively. Compared to the equation of motion for a single oscillator, the last term containing the coupling constant g multiplied by the positional difference is added on the left-hand side of each equation to represent the effect of the second oscillator's movement on that of the first one and vice versa. We write $\frac{g}{m_B} = \omega_{BD}^2$ for the coupling effect of the dark mode on the bright mode, and $\frac{g}{m_D} = \omega_{DB}^2$ for the coupling effect of the bright mode on the dark mode. (Unlike other literature [49, 220, 221], we do not assume that these two terms are identical in order to develop the equation further later with the particle, although they can be taken as equal for now.) Since g can be positive or negative depending on the type of interactions (similar to how the Fano parameter q can be positive or negative, as illustrated in Figure 6.14) [49], the values for ω_{BD}^2 and ω_{DB}^2 can also be positive or negative despite their squared expression, which follows the convention of the oscillator model for convenience.

Introducing $F = \hat{F}e^{i\omega t}$ and $x_{B,D} = \hat{x}_{B,D}e^{i\omega t}$ into Equations 6.6a and 6.6b and expressing them in a matrix form yields the following equation:

$$\begin{bmatrix} \omega_B^2 + \omega_{BD}^2 - \omega^2 + i\gamma_B\omega & -\omega_{BD}^2 \\ -\omega_{DB}^2 & \omega_D^2 + \omega_{DB}^2 - \omega^2 + i\gamma_D\omega \end{bmatrix} \begin{bmatrix} \hat{x}_B \\ \hat{x}_D \end{bmatrix} e^{i\omega t} = \begin{bmatrix} \frac{\hat{F}}{m_B} \\ \frac{\hat{F}}{m_D} \end{bmatrix} e^{i\omega t}. \quad (6.7)$$

By dividing out $e^{i\omega t}$ and multiplying with the inverse matrix on both sides, the following responses are obtained for the bright and dark modes:

$$\begin{bmatrix} \hat{x}_B \\ \hat{x}_D \end{bmatrix} = \begin{bmatrix} \omega_B^2 + \omega_{BD}^2 - \omega^2 + i\gamma_B\omega & -\omega_{BD}^2 \\ -\omega_{DB}^2 & \omega_D^2 + \omega_{DB}^2 - \omega^2 + i\gamma_D\omega \end{bmatrix}^{-1} \begin{bmatrix} \frac{\hat{F}}{m_B} \\ \frac{\hat{F}}{m_D} \end{bmatrix}. \quad (6.8)$$

The ultimate quantity of interest is the squared magnitude of the sum of \hat{x}_B and \hat{x}_D (i.e., $|\hat{x}_B + \hat{x}_D|^2$), which corresponds to the total signal intensity of the coupled system. For curve fitting, we simplify $\frac{\hat{F}}{m_B} = A_B$ and $\frac{\hat{F}}{m_D} = A_D$ as we did with the single oscillator model; the final fitting parameters in $|\hat{x}_B + \hat{x}_D|^2$ are ω_B^2 , γ_B , and A_B for bright mode; ω_D^2 , γ_D , and A_D for dark mode; and ω_{BD}^2 and ω_{DB}^2 for the coupling.

Table 6.1 – Constraints and settings used in nanoflower simulation fitting.

| Boundary constraints | | | | |
|---|--|------------------------------------|------------------------------------|-----------------------|
| Parameter name (unit) | Lower bound | Lower bound for initial points* | Upper bound for initial points* | Upper bound |
| ω_B^2, ω_D^2 (eV ²) | 2 (\approx 877 nm) | 2 | 4 | 7 (\approx 469 nm) |
| $\omega_{BD}^2, \omega_{DB}^2$ (eV ²) | -3 | -0.5 | 0.5 | 3 |
| γ_B, γ_D (eV) | 0.01 | 0.01 | 1 | 3 |
| A_B, A_D | 0 | 0 | 1 | 5 |
| * Initial values are randomly chosen within these bounds. | | | | |
| Additional constraints | | | | |
| $\omega_{BD}^2 = \omega_{DB}^2$ | (Assuming that $m_B = m_D$) | | | |
| $\omega_D^2 > \omega_B^2$ | (Assuming that the dark mode has a higher energy than the bright mode) | | | |
| Miscellaneous settings | | | | |
| a. Number of trials: | 64 | | | |
| b. Fitting range: | 500 nm < λ < 1000 nm | | | |
| c. Regularization: | L2-norm [223] | | | |

In our curve fitting, the primary objective is to minimize in the least-squares sense the difference between the response from the coupled oscillator model and that from the simulation. The dashed line in Figure 6.15b shows the fitted curve, and the heat map in Figure 6.15c depicts the values of the fitting parameters. The diagonal values in the above heat map refer to ω_B^2 and ω_D^2 , which are the squared resonance frequencies of the uncoupled bright and dark modes. The off-diagonal terms are the coupling constants, ω_{BD}^2 and ω_{DB}^2 . During the fitting process, we assumed $\omega_{BD}^2 = \omega_{DB}^2$ under the assumption that all electrons in the nanoflower participate in both modes and thus $m_B = m_D$. The resonant frequencies of the coupled bright and dark modes are the sum of each row's diagonal and off-diagonal components. The detailed fitting constraints are provided in Table 6.1. We utilized a Python package (Scipy optimization; *scipy.optimize.minimize* function) to solve the optimization problem with linear and non-linear constraints [222].

The fitted spectrum in Figure 6.15b closely matches the simulated spectrum, demonstrating the congruence of the Fano interference model in representing the nanoflower's response. Moreover, the damping constant for the bright mode is much larger than that for the dark mode. ($\gamma_B \gg \gamma_D$) as predicted by the Fano model. It also appears that the bright mode drives the dark mode rather than the external field since $A_D = 0$, as shown in Figure 6.15b.

Figure 6.16 depicts the polarization charges close to and far from the Fano resonance wavelength, which provides some physical insight into the bright and dark modes in the nanoflower system. For wavelengths far from the Fano interference range, e.g., at $\lambda_{\text{inc}} = 800$ nm in Figure 6.16a, the charges have a dipole-like distribution (the incident field was polarized along the horizontal direction). This distribution persists across the whole wavelength spectrum, with the exception of the narrow region where Fano interference occurs. In the middle of

the Fano interference region, e.g., at $\lambda_{inc} = 660$ nm in Figure 6.16b, a more complex distribution of charges emerges on top of the dipole-like distribution. Because the external electric field only has a horizontal component, it is more likely that the nanoflower's near-field was responsible for this intricate charge distribution than the direct external electric field. This interpretation supports the fitting result that the dark mode is not externally driven. ($A_D = 0$). In addition, it is widely understood that quadrupoles and higher-order modes contribute little to far-field scattering. Consequently, the development of these higher-order modes provides a new, complementary perspective on the decrease in the scattering spectrum.

Having validated its applicability with simulated data, we applied the Fano interference model to experimental results (Figure 6.17, for the nanostructures shown in Figure 6.8). For experimental data fitting, we utilized some prior information from the simulation fitting, as the measurement fitting was more challenging due to weakened Fano features, as visible in Figure 6.17a. To summarize, we tightened the upper and lower limits on fitting parameters and implemented additional parameter regulations, as detailed in Table 6.2. To be more specific, we imposed the following two constraints: First, we assumed that the dark mode is not driven externally, in agreement with the simulation fitting, and set accordingly $A_D = 0$. Second, we constrained the damping and coupling constants to satisfy $\gamma_B > |\omega_{BD}| > \gamma_D$, which corresponds to the regime of weak coupling in Fano interference [224]. The simulation fitting result satisfied this condition, and we applied it to the measurement fitting; without this constraint and as a result of overfitting, the parameters would have values diametrically opposed to those predicted by the Fano model, such as $\gamma_D \gg \gamma_B$. To comply with this constraint, we applied additional regularization on $|\omega_{BD}|$ and $|\omega_{DB}|$ and adjusted the regularization weights for each fitting.

As a result, good agreements were observed between the measured and fitted spectra in Figure 6.17a. Fluctuation in the values of the fitting parameters in Figure 6.17b might have been caused by variations in the shapes of nanoflowers after fabrication, although we did not observe a clear distinction between F2 and F3. The diminished Fano interference in the

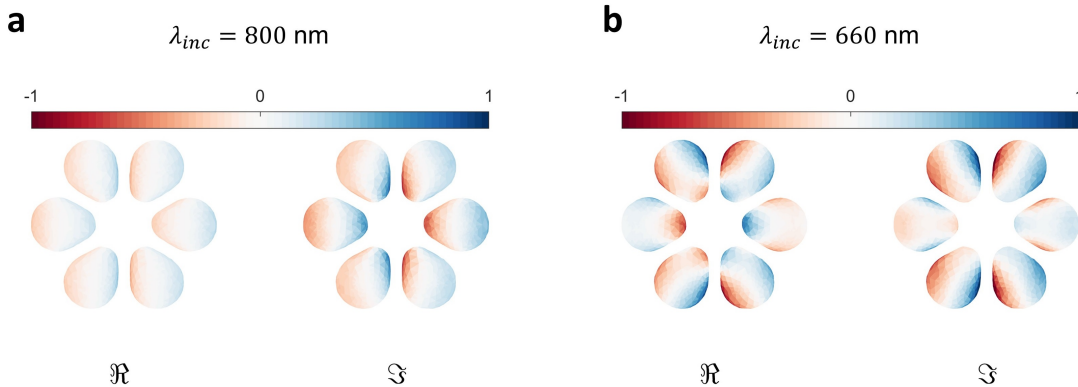


Figure 6.16 – Polarization charge distributions far from the Fano resonant wavelength (a) and in the middle of the Fano resonant wavelength (b).

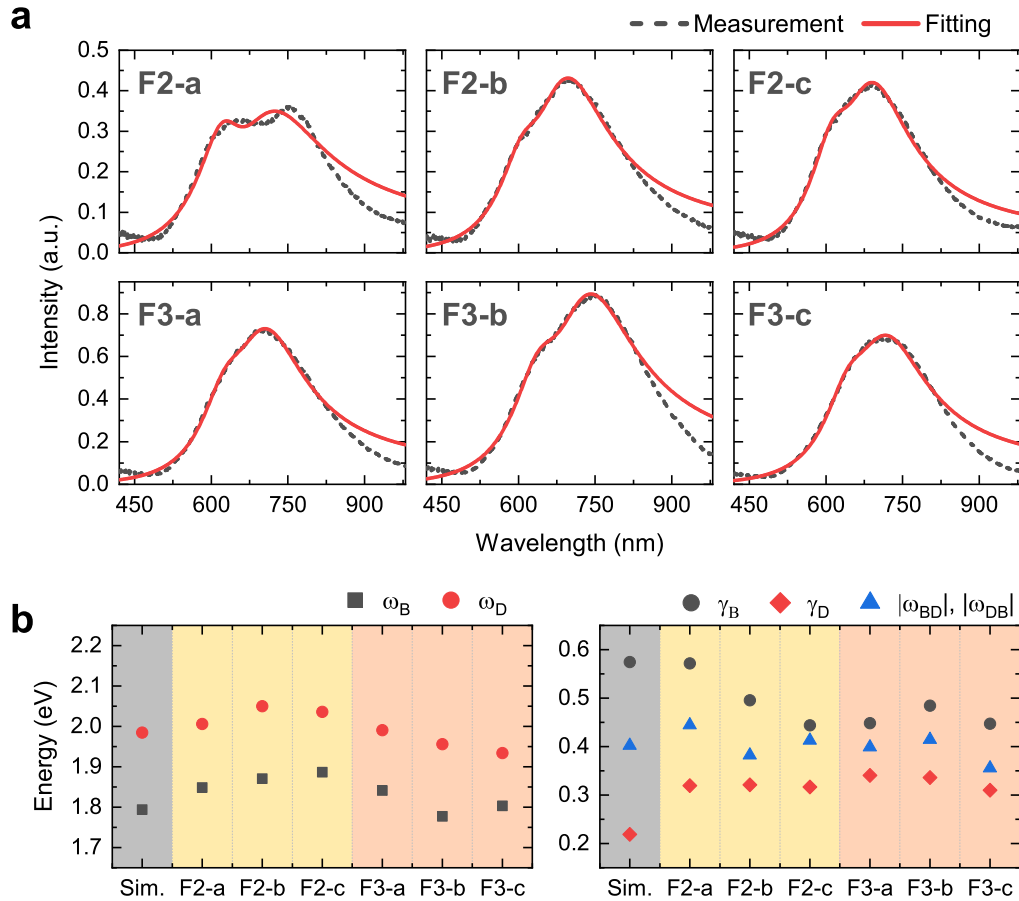


Figure 6.17 – Two-coupled oscillator model fitted to the nanoflower spectral measurements. **a**, Measured and fitted spectra for the six previously presented examples. **b**, Corresponding fitting parameter values including those for simulation: (left) the resonant frequencies of the bright and dark modes, ω_B and ω_D ; (right) the damping constants (γ_B and γ_D) and the absolute value of the coupling constants (ω_{BD} and ω_{DB} , which are set to be equal).

Table 6.2 – Constraints and settings used in nanoflower measurement fitting.

| Boundary constraints | | | | |
|---|--|------------------------------------|------------------------------------|--------------|
| Parameter name (unit) | Lower bound | Lower bound for initial points* | Upper bound for initial points* | Upper bound |
| ω_B^2, ω_D^2 (eV ²) | 2 (≈ 877 nm) | 3 | 4 | 5 (≈ 555 nm) |
| $\omega_{BD}^2, \omega_{DB}^2$ (eV ²) | -3 | -0.5 | 0 | 0** |
| γ_B, γ_D (eV) | 0.01 | 0.1 | 1 | 3 |
| A_B | 0 | 0 | 1 | 5 |
| * Initial values are randomly chosen within these bounds. | | | | |
| ** The upper limit of 0 makes these parameters always negative. | | | | |
| Additional constraints | | | | |
| $\omega_{BD}^2 = \omega_{DB}^2$ | (Assuming that $m_B = m_D$) | | | |
| $\omega_D^2 > \omega_B^2$ | (Assuming that the dark mode has a higher energy than the bright mode) | | | |
| $A_D = 0$ | (Assuming that the dark mode is not externally driven) | | | |
| $\gamma_B > \omega_{BD} > \gamma_D$ | (Weak-coupling regime [224]) | | | |
| Miscellaneous settings | | | | |
| a. Number of trials: | 32 | | | |
| b. Fitting range: | 500 nm < λ < 850 nm | | | |
| c. Regularization: | L2-norm | | | |

measured spectra led to smaller differences between γ_B and γ_D .

So far, the parameters used in the single oscillator and two-coupled oscillator models have successfully represented the nanoparticle and nanoflower systems, respectively. Using these parameters as building blocks, we will construct a coupled system with three oscillators: one for the nanoparticle and two for the nanoflower. We will then estimate the spring constants connecting these two systems to quantify the coupling strength, which will be discussed in depth in the following section.

Three coupled oscillators

What would happen if two independent systems were brought close together? We know that the charges on each system would interact more strongly as they get closer [225]. We model this additional interaction by adding new “springs” into the existing system. When we trap a particle inside a nanoflower, we assume that two additional connections form between the particle and the nanoflower’s bright and dark modes, as depicted in Figure 6.18. Using these three coupled oscillators, we attempt to find parameters that describe the spectral response of coupled flower–particle system.

The equations describing the motion of these oscillators are very similar to those describing the motion of the two coupled oscillators (Equation 6.6). Although Figure 6.18 is drawn in two dimensions, we formulate the equations of motion in one dimension. In other words, we

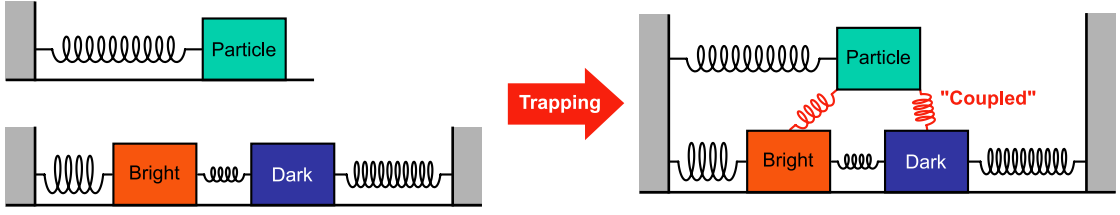


Figure 6.18 – Coupled oscillator model for nanoflower–nanoparticle coupled system. (Left) Separate systems before trapping. (Right) Coupled particle–flower (bright and dark) system after trapping.

describe each oscillator's displacement with a single coordinate, x , as we did previously for the particle and nanoflower modeling. The underlying idea is that since the external driving force is a linearly polarized electric field, we only consider the charge oscillations along this direction to simplify the problem. In addition, the bright and dark oscillators are notional oscillators with no direct relationship to physical space. This notion allows us to align the three oscillators in one dimension.

Based on this understanding, we construct the equations of motion for the bright (B), dark (D), and particle (P) oscillators as follows:

$$\frac{d^2 x_B}{dt^2} + \gamma_B \frac{dx_B}{dt} + \omega_B^2 x_B + \omega_{BD}^2 (x_B - x_D) + \frac{h}{m_B} (x_B - x_P) = \frac{F}{m_B}, \quad (6.9a)$$

$$\frac{d^2 x_D}{dt^2} + \gamma_D \frac{dx_D}{dt} + \omega_D^2 x_D + \omega_{DB}^2 (x_D - x_B) + \frac{q}{m_D} (x_D - x_P) = \frac{F}{m_D}, \quad (6.9b)$$

$$\frac{d^2 x_P}{dt^2} + \gamma_P \frac{dx_P}{dt} + \omega_P^2 x_P + \frac{h}{m_P} (x_P - x_B) + \frac{q}{m_P} (x_P - x_D) = \frac{F}{m_P}, \quad (6.9c)$$

where h and q are the spring constants for the newly added springs connecting the particle and the nanoflower's bright and dark modes.

Introducing $F = \hat{F}e^{i\omega t}$ and $x_{B,D,P} = \hat{x}_{B,D,P}e^{i\omega t}$ into Equations 6.9 and expressing them in a matrix form yields the following equation:

$$\begin{bmatrix} \omega_B^2 + \omega_{BD}^2 + \omega_{BP}^2 - \omega^2 + i\gamma_B\omega & -\omega_{BD}^2 & -\omega_{BP}^2 \\ -\omega_{DB}^2 & \omega_D^2 + \omega_{DB}^2 + \omega_{DP}^2 - \omega^2 + i\gamma_D\omega & -\omega_{DP}^2 \\ -\omega_{PB}^2 & -\omega_{PD}^2 & \omega_P^2 + \omega_{PB}^2 + \omega_{PD}^2 - \omega^2 + i\gamma_P\omega \end{bmatrix} \begin{bmatrix} \hat{x}_B \\ \hat{x}_D \\ \hat{x}_P \end{bmatrix} = \begin{bmatrix} \frac{\hat{F}}{m_B} \\ 0 \\ \frac{\hat{F}}{m_P} \end{bmatrix}, \quad (6.10)$$

where ω_{BP}^2 , ω_{PB}^2 , ω_{DP}^2 , and ω_{PD}^2 refer to the spring constants of the newly added springs, renamed following the previous naming convention (similar to Figure 6.15a). We do not assume that $\omega_{BP}^2 = \omega_{PB}^2$ and $\omega_{DP}^2 = \omega_{PD}^2$ because the mass of the particle oscillator and that of the nanoflower oscillators may not be the same. Consequently, we now have four new parameters to estimate for the two new springs. We also assume that the dark mode of the nanoflower is not externally driven as was previously the case, and thus, the second row on

the right-hand side of Equation 6.10 is set to zero.

Using Equation 6.10, we can obtain the total signal intensity of the three coupled oscillators, $|\hat{x}_B + \hat{x}_D + \hat{x}_P|^2$, by multiplying the inverse matrix on both sides and calculating the squared magnitude of their sum. We will fit this function, $|\hat{x}_B + \hat{x}_D + \hat{x}_P|^2$, initially to simulated data and subsequently to experimental data. The fitting parameters are listed in the following:

- For the bright mode: ω_B^2 , ω_{BD}^2 , ω_{BP}^2 , γ_B , and A_B .
- For the dark mode: ω_D^2 , ω_{DB}^2 , ω_{DP}^2 , and γ_D .
- For the particle: ω_P^2 , ω_{PB}^2 , ω_{PD}^2 , γ_P , and A_P .

We have a total of 14 parameters to fit. This large number of fitting parameters reduces the reliability of the analysis and makes it prone to overfitting [223]. To reduce this inaccuracy, we can draw on prior knowledge from the decoupled individual systems. For example, we already know the natural frequency of each oscillator when they are completely decoupled. We can assume that the trapping process has no effect on these natural frequencies. Likewise, we assumed that the coupling between the bright and dark modes, which is solely determined by the nanoflower, remains constant. The value of A_B , which is related to the external excitation of the nanoflower's bright mode, was also fixed to reduce the number of fitting parameters, sacrificing the fitting exactness. We highlighted in red the parameters in the list above that we assumed were unaffected by particle trapping.

To test this three-coupled oscillator model, we developed two independent simulation scenarios: First, we fixed the particle size and only changed its height from the x - y plane. (This height refers to the distance between the bottom surface of the particle and that of the nanoflower. We call it z_{offset} henceforth. When $z_{\text{offset}} = 0$, the bottom surfaces of the particle and the nanoflower are on the same plane.) Second, we fixed the z_{offset} to zero and changed its size. Both scenarios change the gap distance between the particle and the nanoflower. Consequently, we expect a change in coupling strength, and therefore, the values of ω_{BP}^2 , ω_{PB}^2 , ω_{DP}^2 , and ω_{PD}^2 in both scenarios.

A massive benefit of numerical simulation is that we can disassemble the system and examine the response from each component. For all different simulations in each scenario, we first calculated the surface currents on the geometric mesh of the coupled system. Then, by selecting the surface currents only on the particle mesh or the nanoflower mesh, we separated the coupled response into one from the nanoparticle and one from the nanoflower. In the three-coupled oscillator model, this process corresponds to separating $|\hat{x}_B + \hat{x}_D + \hat{x}_P|^2$ into $|\hat{x}_B + \hat{x}_D|^2$ (for nanoflower) and $|\hat{x}_P|^2$ (for nanoparticle). Obviously, this cannot be accomplished with measurement data. However, by finding the parameters simultaneously describing the three distinct responses in simulation fitting, we can significantly improve the fitting accuracy, which will serve as a valuable guideline for measurement fitting.

Figure 6.19 illustrates the fitting results with the varying z_{offset} scenario for a 100 nm particle. The first row demonstrates an example set of the spectra at $z_{\text{offset}} = 25$ nm. The spectral

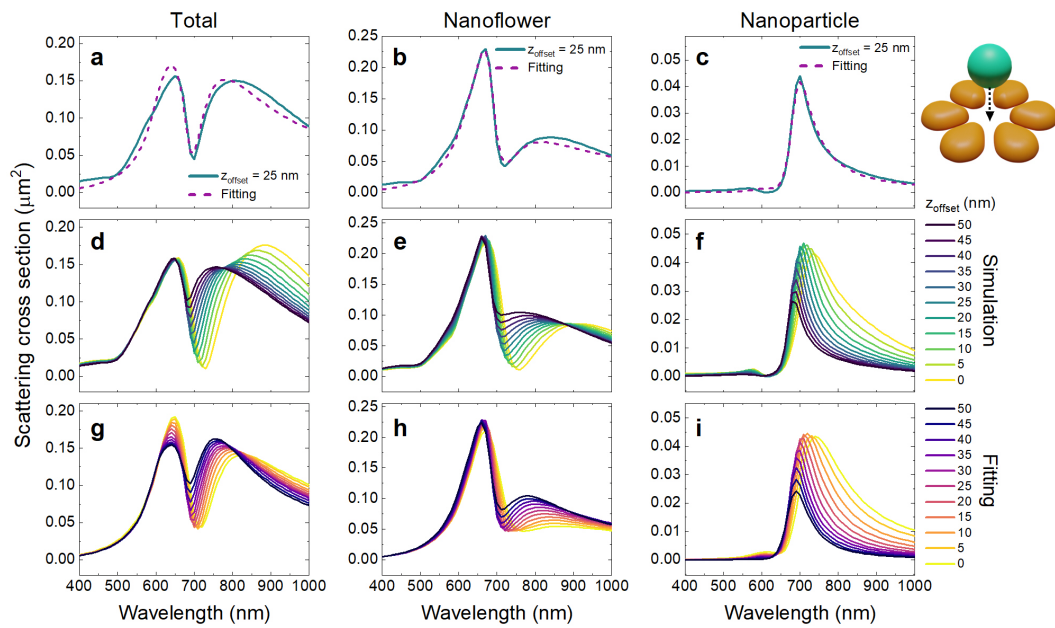


Figure 6.19 – Simulation fitting while changing the particle's height (z_{offset}). The particle diameter was fixed as 100 nm.

1st row: Numerically simulated spectra of the coupled system when $z_{\text{offset}} = 25$ nm (a), as well as partial responses from the nanoflower and nanoparticle (b and c), respectively. The dashed lines show fitting results with the three-coupled oscillator model.

2nd row: A collection of simulation spectra for the entire and partial systems while changing the z_{offset} from 50 nm (deep blue) to 0 nm (yellow), which in the direction towards the nanoflower.

3rd row: The corresponding fitting curves for the results shown in d, e, and f.

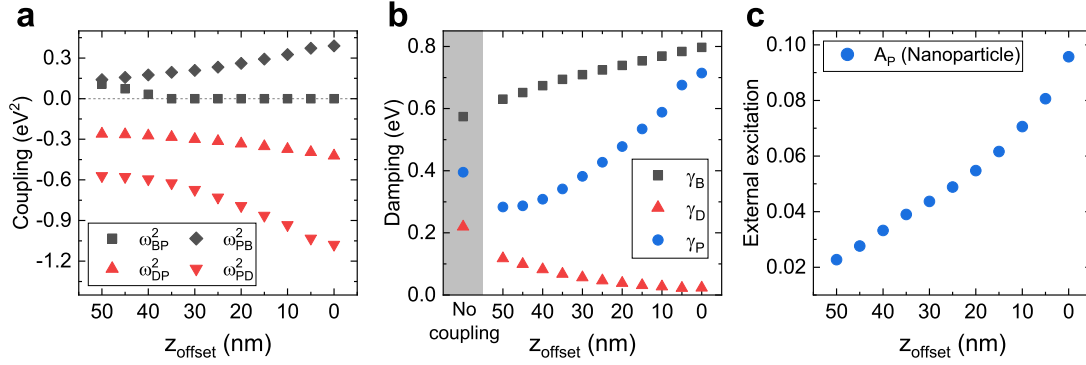


Figure 6.20 – Fitting parameter values as a function of the particle height from the x - y plane (z_{offset}). **a**, Four coupling constants for the two additional springs. **b**, Three damping constants for the three oscillators. **c**, An amplitude constant for the nanoparticle. The values of A_B and A_P for the bright and dark modes were fixed at 0.47 and 0, respectively.

response of the entire system is shown in **a**, while the responses of the cleaved nanoflower and particle are depicted in **b** and **c**, respectively. The fitting results (dashed lines) are, respectively, $|\hat{x}_B + \hat{x}_D + \hat{x}_P|^2$, $|\hat{x}_B + \hat{x}_D|^2$, and $|\hat{x}_P|^2$ for the three (B , D , and P) oscillators. The second row shows the simulated spectra obtained by varying the value of z_{offset} from 50 to 0 nm toward the nanoflower. The spectral splitting becomes greater in the case of the total response (**d**), and the partial responses for the nanoflower and the particle also develop gradually (**e** and **f**). In the last row, the fitted curves are presented in the same manner, demonstrating that the fitting outcomes satisfy the three curves at the same time for all different z_{offset} values.

Figure 6.20 provides a summary of the fitted parameters used to generate the fitting spectra in Figure 6.19. We fitted a total of eight parameters, including four coupling constants (**a**), three damping constants (**b**), and an amplitude constant for the particle (**c**). The fitting constraints and settings are described in detail in Table 6.3. As the particle approaches the nanoflower, the magnitudes of each of these parameters gradually change. This consistent trend indicates that the fitted parameters capture the spectrum's gradual transitions. However, the physical interpretations of these parameters are not straightforward. For instance, what is the meaning of positive and negative spring constants? What causes an increase or decrease in damping constants? To obtain an understanding of their physical origins, we will investigate the behavior of the polarization charges of the coupled system.

We first calculated the nanoflower's and nanoparticle's dipole moments for quantitative analysis. In particular, we separated the dipole moments not only between the particle and the nanoflower but also among the petals. This calculation revealed that the dipole moments of the two horizontal petals are identical due to their symmetries, and so are the four diagonal petals. Therefore, we shall examine the representative responses of a horizontal petal, a diagonal petal, and the nanoparticle.

Figure 6.21b illustrates the amplitudes of the dipole moment along the x -axis. The horizontal

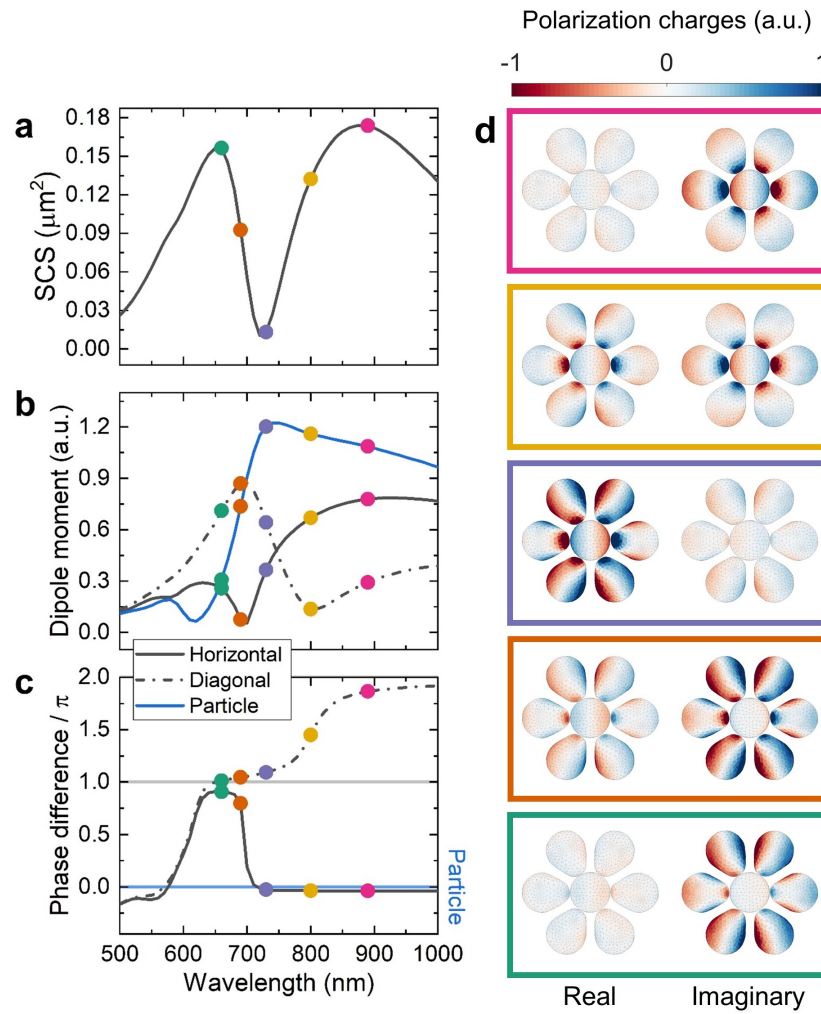


Figure 6.21 – Examples of polarization charge distributions at five different wavelengths. These wavelengths were chosen by examining the maxima, minima, or inflections points in the scattering cross section (a), the amplitudes of dipole moments (b), and their phase (c). d, The polarization charge distributions were evaluated at these wavelengths (890, 800, 730, 690, and 660 nm, from pink at the top to green at the bottom).

Table 6.3 – Fitting constraints for coupled system (varying the particle's z_{offset}).

| Boundary constraints | | | | |
|--|------------------------------|-----------------------------------|-----------------------------------|-------------|
| Parameter name (unit) | Lower bound | Lower bound for initial points | Upper bound for initial points | Upper bound |
| $\omega_{BP}^2, \omega_{PB}^2, \omega_{DP}^2, \omega_{PD}^2$ (eV^2) | -3 | -1 | 0 | 3 |
| γ_B (eV) | γ_B (decoupled)* | 0.01 | 1 | 10 |
| γ_D, γ_P (eV) | 0.01 | 0.01 | 1 | 10 |
| A_P (eV) | 0 | 0 | 1 | 5 |
| * 0.57 eV | | | | |
| Fixed parameters [†] | | | | |
| ω_B^2 | 3.22 eV^2 | | | |
| ω_D^2 | 3.93 eV^2 | | | |
| $\omega_{BD}^2, \omega_{DB}^2$ | -0.16 eV^2 | | | |
| ω_P^2 | 4.39 eV^2 | | | |
| A_B | 0.47 | | | |
| A_D | 0 | | | |
| [†] The values are obtained from the decoupled nanoflower or nanoparticle response. | | | | |
| Miscellaneous settings | | | | |
| a. Number of trials: | 32 | | | |
| b. Fitting range: | 500 nm < λ < 1000 nm | | | |
| c. Regularization: | L2-norm | | | |

and diagonal petals display opposing patterns in their spectra, particularly near the Fano interference range, whereas the trapped particles appear to be relatively independent. Additionally, we computed the phase of each dipole moment; Figure 6.21c shows the phase differences relative to the particle for the horizontal and diagonal petals.

From the dipole moments' amplitudes and phase differences, as well as the scattering cross section of the entire structure (Figure 6.21a), we chose five different wavelengths, from which we computed the polarization charge distributions. These wavelengths are indicated by colored dots in Figures 6.21a–c, which were determined by analyzing the curves' maxima, minima, and inflection points. These wavelengths are respectively 890 (pink), 800 (yellow), 730 (violet), 690 (orange), and 660 nm (green).

When the driving frequency is lower than the resonance frequencies of all the oscillators, which is the case when $\lambda_{\text{inc}} = 890$ nm, the particle and horizontal petals are strongly excited, and they are in phase with each other (pink dots in Figure 6.21b and c) because both remains in phase with the external driving force. This behavior is also confirmed by the polarization charge distribution in the first pink box of Figure 6.21d.

Passing through the transition points colored in yellow toward shorter wavelengths, we arrive at the points in violet, where the scattering cross section nearly vanishes (Figure 6.21a). Interestingly, the maximum dipole moment of the particle occurs at this wavelength. The dipole

moments of the diagonal petals also exhibit a trend of rapid growth. The explanation behind this contradicting observation is that the dipole moments of the particle and the diagonal petals are out of phase (Figure 6.21c), and they effectively cancel out each other such that the total dipole moment also reaches its minimum (data not shown but very similar to the scattering cross section in **a**).

At this wavelength, we are in the middle of the Fano interference range, where the interaction represented by the newly added springs is most prominent. Thus, we shall investigate in detail the charge behaviors depicted in the violet box of Figure 6.21d. As quantified in the phase difference in **c**, the charge distributions of the particle and diagonal petals are opposite. However, due to the unique geometrical configurations of the particle–nanoflower coupled system, this opposite charge distribution forms a local “bonding” mode.

Typically, the spring constant for a bonding mode should be positive, similar to a real mechanical spring. When the electrons of an oscillator are pushed to one side, electrostatic repulsion causes them to push the electrons of a neighboring oscillator in the same direction, which exposes the fixed positive ions of the neighboring oscillator and induces additional attraction at the gap. In other words, they move in phase with each other when forming a bonding mode. This interaction is comparable to the motion of two masses connected by a spring. When one mass is pushed, the energy is transferred through the spring, and the other mass is pushed in the same direction. However, at this wavelength of 730 nm, the electrons in the nanoparticle and adjacent diagonal petals move in the opposite direction while forming a bonding mode. This counter-intuitive behavior explains the negative spring constant between the dark mode and the particle mode.

As indicated by the orange and green points, the out-of-phase relationship between the particle and the petals remains for shorter wavelengths. Meanwhile, the phase difference between the horizontal and diagonal petals approaches zero, and thus we recover the high level for the scattering cross section.

To summarize, the in-phase bonding mode between the particle and the horizontal petal can be modeled with a positive spring constant. In contrast, the out-of-phase bonding mode between the particle and the diagonal petals can be modeled with a negative spring constant. These arguments explain the positive and negative spring constants obtained from the curve fitting in Figure 6.20a, given that the horizontal petals are primarily responsible for the bright mode and the diagonal ones for the dark mode, as depicted in Figure 6.4.

The increasing damping constants in Figure 6.20b can also be understood by the bonding behaviors. Similar to two masses connected by a spring, when one mass drives the other, the movement of both masses encounters greater resistance than the uncoupled system. In the case of the particle–flower system, the flower is strongly excited by the external field ($A_B \gg A_P$) and induces the particle oscillation. As a result, the dipole moment of the particle in the coupled system greatly deviates from its resonant behavior as a single oscillator, as depicted by the blue solid line in Figure 6.21b compared to the one in Figure 6.13a. The other

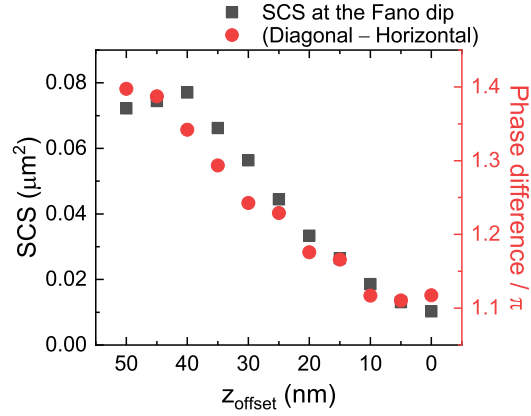


Figure 6.22 – Correlation between the total scattering cross section and the phase difference between the horizontal and diagonal petals as a function of z_{offset} .

evidence is that the phase of the particle moment lags slightly behind that of the horizontal petal (c) for wavelengths longer than 700 nm, meaning that the bright mode drives the particle mode overall (except for the Fano interference region). Therefore, based on these findings, the increasing damping constants for the bright and particle modes in Figure 6.20b can be understood as the result of their increasing bonding interaction with the particle approaching the nanoflower.

On the other hand, a plausible explanation for the decreasing damping constant for the dark mode (γ_D) is suppressed scattering at the Fano dip. In Figure 6.19d, we observed a gradual decrease in scattering in the Fano interference region. This evolution suggests that the radiative damping is more effectively suppressed as the particle approaches the nanoflower. From the dipole moment analysis in Figure 6.21, we have learned that the Fano dip occurs when the dipole moments of the horizontal and diagonal petals are out of phase and effectively cancel out each other. In fact, we discovered that when the particle is still away from the flower (i.e., $z_{\text{offset}} = 50$), the phase difference between the horizontal and diagonal petals is 1.4π at the Fano dip, indicating that they are halfway between in-phase and out-of-phase relationships and are still a long way from effective cancellation. This phase difference decreases gradually until it reaches approximately 1.1π when $z_{\text{offset}} = 10$. Figure 6.22 summarizes the phase difference and total dipole moment amplitude at the Fano dip as a function of z_{offset} . Their strong correlation suggests that the presence of the particle modifies the phase difference between the horizontal and diagonal petals and, consequently, the radiative damping of the system is suppressed, which can result in the decreasing damping constant for the dark mode.

Now, let us move on to the next scenario. We simulated the entire and partial responses while increasing the particle diameter (D) from 60 nm to 140 nm, and then we applied the three-coupled oscillator model again to fit these curves. Figure 6.23 illustrates the simulation and fitting results in this scenario. For all diameters, the particle's bottom surface was fixed to the x - y plane ($z_{\text{offset}} = 0$ nm). Compared to the first scenario, a notable difference in the second scenario is that the particle diameter is changing, and consequently, so are its resonant characteristics. Therefore, this scenario includes the effects of changing particle resonances as well as changing gap distances.

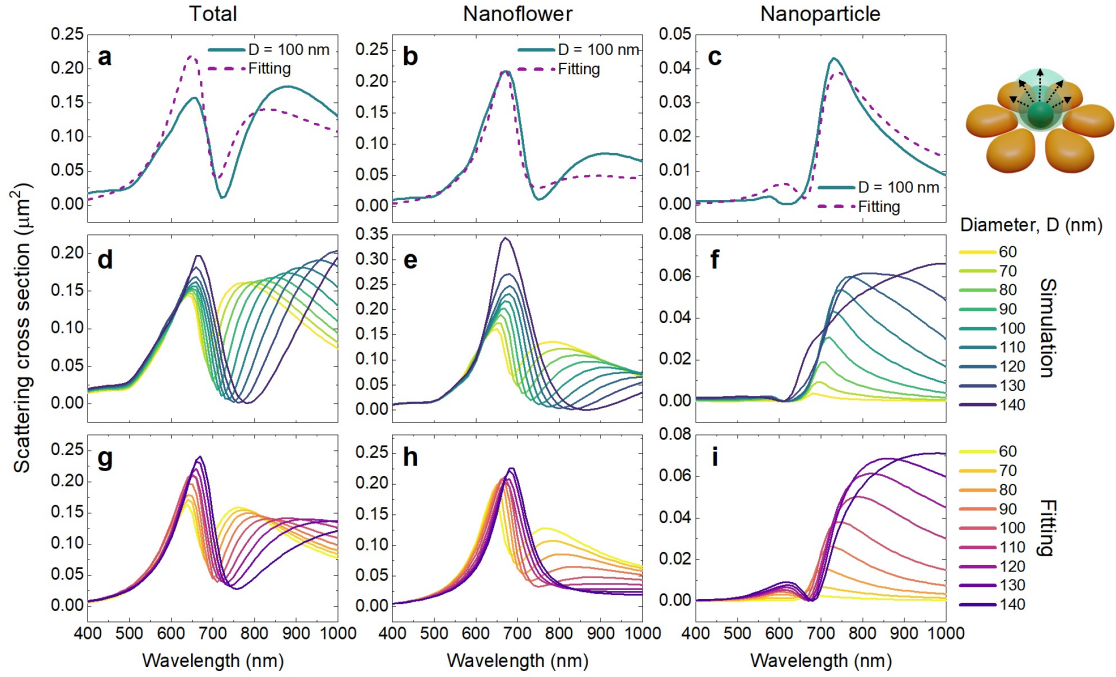


Figure 6.23 – Simulation fitting while changing the particle's diameter (D). The particle's z_{offset} was fixed as 0 nm.

- 1st row:** Numerically simulated spectra of the coupled system when $D = 100$ nm (a), as well as partial responses from the nanoflower and nanoparticle (b and c), respectively. The dashed lines show fitting results with the three-coupled oscillator model.
- 2nd row:** A collection of simulation spectra for the entire and partial systems while changing D from 60 nm (yellow) to 140 nm (deep blue).
- 3rd row:** The corresponding fitting curves for the results shown in d, e, and f.

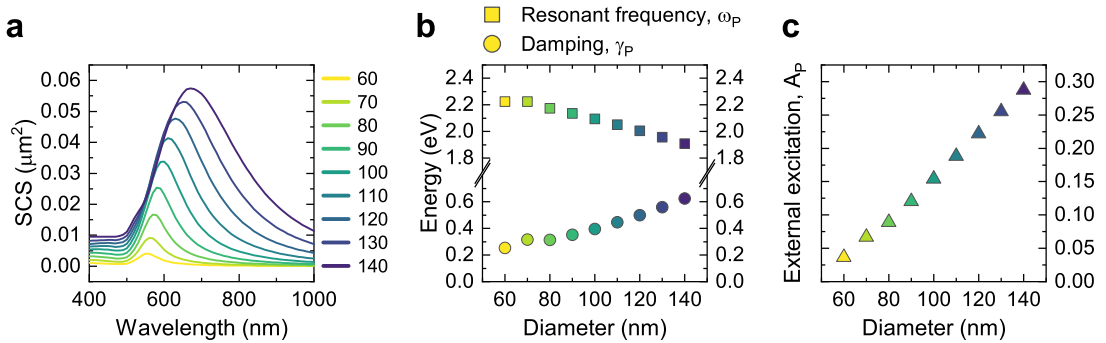


Figure 6.24 – Spectral responses of a particle with a varying diameter (60 – 140 nm, a) and parameters for the single oscillator model to represent these responses (b and c).

Table 6.4 – Fitting constraints for coupled system (varying particle diameter).

| Boundary constraints | | | | |
|---|---|-----------------------------------|-----------------------------------|-------------|
| Parameter name (unit) | Lower bound | Lower bound for initial points | Upper bound for initial points | Upper bound |
| $\omega_{BP}^2, \omega_{PB}^2, \omega_{DP}^2, \omega_{PD}^2$ (eV ²) | -3 | -1 | 0 | 3 |
| γ_B (eV) | γ_B (decoupled)* | 0.01 | 1 | 3 |
| γ_D (eV) | 0.01 | 0.01 | 1 | 3 |
| γ_P (eV) | γ_P (decoupled)** | 0.01 | 1 | 3 |
| * 0.57 eV | | | | |
| ** Variable between 0.25 – 0.62 eV depending on the particle size | | | | |
| Fixed parameters [†] | | | | |
| ω_B^2 | 3.22 eV ² | | | |
| ω_D^2 | 3.93 eV ² | | | |
| $\omega_{BD}^2, \omega_{DB}^2$ | -0.16 eV ² | | | |
| ω_P^2 | Variable between 3.65 – 4.95 eV ² depending on the particle size | | | |
| A_B | 0.47 | | | |
| A_D | 0 | | | |
| A_P | Variable between 0.04 – 0.29 depending on the particle size | | | |
| [†] The values are obtained from the decoupled nanoflower or nanoparticle responses. | | | | |
| Miscellaneous settings | | | | |
| a. Number of trials: | 32 | | | |
| b. Fitting range: | 500 nm < λ < 1000 nm | | | |
| c. Regularization: | L2-norm | | | |

We began by estimating parameters for nanoparticles detached from the nanoflower. We simulated the spectral responses of a particle whose diameter varies from 60 to 140 nm (Figure 6.24a). In the single oscillator model, the particle's response is represented by three parameters: the resonant frequency, the damping constant, and the amplitude constant. Using Equation 6.5, we estimated these three parameters (ω_P , γ_P , and A_P), and the results are summarized in Figures 6.24b and c. We utilized the fitted values for the resonant frequency (ω_P) and the amplitude constant (A_P) for the curve fitting with the coupled system. We excluded the damping constant (γ_P) from direct use in the fitting, based on our observation in the first scenario, where γ_P significantly differed from its value without coupling. Table 6.4 provides the details about fitting constraints and fixed parameters.

The values of the fitting parameters for varying particle diameters are shown in Figure 6.25. Compared to what we observed in the z_{offset} scenario, we find multiple similar attributes:

1. The sign of the spring constants between the bright and particle oscillators and those between the dark and particle oscillators remain unchanged (positive and negative, respectively).
2. The relative magnitude orders of the coupling constants also remain the same:
 - $\omega_{PB}^2 > \omega_{BP}^2$ (implying that $m_B > m_P$).

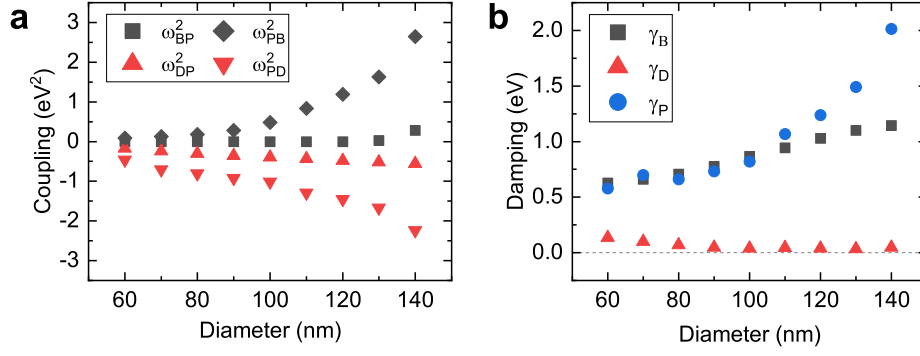


Figure 6.25 – Fitting parameter values as a function of the particle diameter. These parameters were used to produce the fitted curves in Figures 6.23g–i. **a**, Coupling constants in the unit of squared energy (eV^2). **b**, Damping constants in the unit of energy (eV).

- $|\omega_{PD}^2| > |\omega_{DP}^2|$ (implying that $m_D > m_P$).

3. The damping constants for the bright and particle oscillators (γ_B and γ_P) increase with coupling strength.
4. The damping constant for the dark mode (γ_D) decreases with coupling strength.

There are still some minute differences between the first and second scenarios. But more importantly, these shared characteristics serve as a reference for what to look for in various coupling strength regimes. The coupling parameters, in particular, can become a helpful guide for identifying coupling strengths among different measurement results.

6.3.4 Analysis of experimental results using the coupled oscillator model

So far, we have investigated the application of the well-known coupled oscillator model in our nanoflower–nanoparticle system using simulation data. In particular, we analyzed not only the complete response but also the partial responses of the coupled system using versatile numerical simulations. This strategy greatly reduced the uncertainty of curve fitting and produced consistent fitting results as we varied parameters such as the particle height or diameter. The coupling parameters connecting the two independent systems tended to increase in magnitude when we increased the particle size or narrowed down the distance to the nanoflower, which makes them the most obvious indicator in coupled system analysis. We will now examine the application of the three-coupled oscillator model to the measurement data, utilizing the knowledge gained thus far through simulation analysis.

Fitting constraints

We cannot use the same strategy with measurement data, from which we only obtain ensemble responses. Thus, we need a different approach to improve the reliability of parameter estimation. For example, the sign of the coupling constants between the dark (or bright) mode

Table 6.5 – Fitting constraints and settings for measured data.

| Boundary constraints | | | | |
|--|--|-----------------------------------|-----------------------------------|-------------|
| Parameter name (unit) | Lower bound | Lower bound for initial points | Upper bound for initial points | Upper bound |
| $\omega_{BP}^2, \omega_{PB}^2 (eV^2)$ | 0 | -1 | 1 | 3 |
| $\omega_{DP}^2, \omega_{PD}^2 (eV^2)$ | -3 | -1 | 1 | 3 |
| $\gamma_B, \gamma_D, \gamma_P (eV)$ | 0.01 | 0.2 | 1 | 3 |
| A_B, A_P | 0 | 0 | 1 | 5 |
| Fixed parameters | | | | |
| $\omega_B^2, \omega_D^2, \omega_{BD}^2, \omega_{DB}^2$ | Estimated values for the corresponding decoupled nanoflower. | | | |
| ω_P^2 | 4.48 eV ² † | | | |
| † Obtained from a random particle measurement stuck on a glass substrate (Figure 6.13b). | | | | |
| Miscellaneous settings | | | | |
| a. Number of trials: | 32 | | | |
| b. Fitting range: | 500 nm < λ < 920 nm or longer* | | | |
| c. Regularization: | L2-norm | | | |
| * The upper limit was adjusted as illustrated in Figure 6.29. | | | | |

and the particle mode can be predefined to be negative (or positive). Reducing the parameter space may increase the likelihood of locating values that adequately explain the coupling strength of the combined system. In order to justify this idea, we devised a simple test: We tried to reproduce the estimated parameters—that we obtained by simultaneously fitting the three curves—by fitting only the total response but with modified boundary constraints. Going through a process of trial and error, we determined the following constraints that can lead to a better match with the previously found estimates:

- $\omega_{BP}^2, \omega_{PB}^2 > 0$,
- $g_P > g_D$.

With these constraints, as well as utilizing the values from the decoupled systems as detailed in Table 6.5, we re-estimated the parameters for the z_{offset} scenario, and the results are presented in Figure 6.26. The left column shows the former estimates with all the available data for varying z_{offset} , while the right column displays the estimation with limited information. With the aforementioned constraints, we were able to reproduce the previous estimate to some extent. However, their differences become noticeable as the z_{offset} value approaches zero. The values of the coupling constants, particularly those associated with the particle, diverge. The damping constants for the particle and bright modes also increase rapidly compared to the former estimates. These differences result from overfitting, as illustrated in Figure 6.27. The parameters estimated solely from the total response fit even better than the previous estimate for the total response but fail for the nanoflower and nanoparticle responses, indicating that the exaggerated coupling constant values have no physical significance and are simply a result

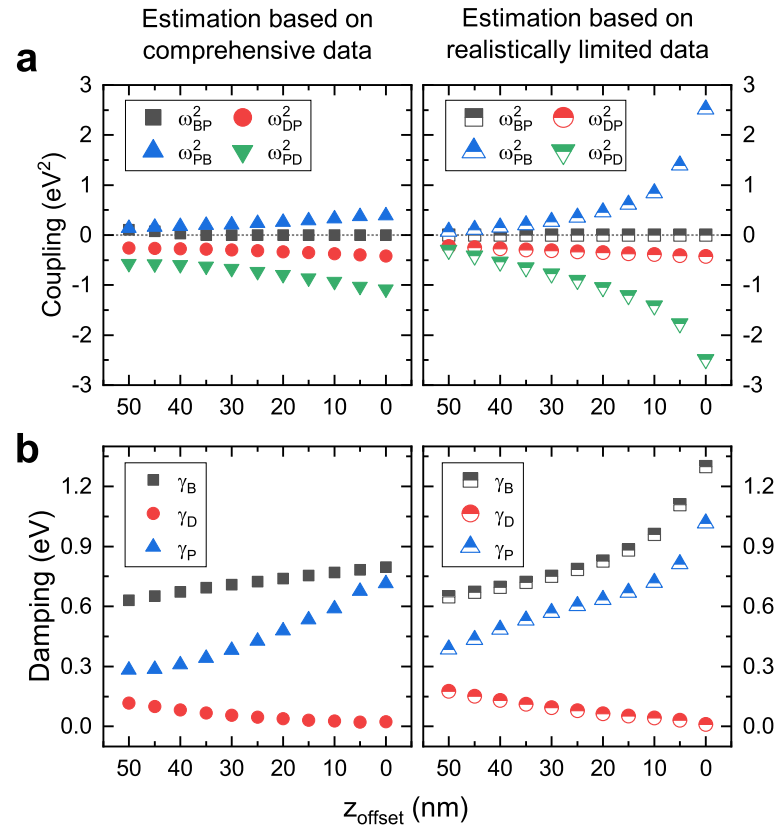


Figure 6.26 – Estimated parameters based on realistically limited data (only with the total response) for varying z_{offset} . Additional constraints were applied as detailed in Table 6.5. For comparison, the previous estimate based on the comprehensive data set is displayed in the left column. **a**, The four coupling constants (squared resonant frequencies). **b**, the three damping constants.

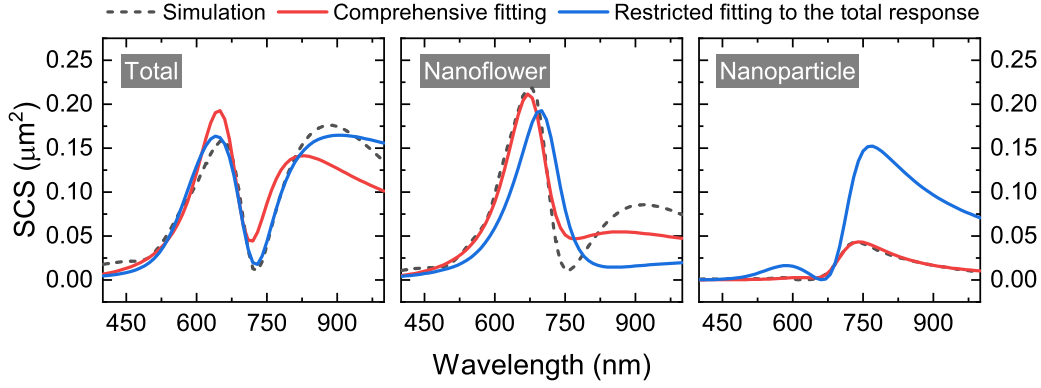


Figure 6.27 – Comparison of simulation responses, previous comprehensive fitting, and fitting with only the total response when $z_{\text{offset}} = 0$.

of being too closely aligned with the simulation result.

Similarly, we retried parameter estimation for the scenario involving varying particle sizes. Changes in particle size affect the peak and width of the resonance spectrum and thus the parameters describing them. In the previous fitting, the resonance frequency of the particle oscillator was altered according to its size. In reality, however, the true particle size is unknown, so there should be a modeling uncertainty if the particle's resonance is assumed to be a randomly measured value. We accounted for this error in this retrial by intentionally setting the particle's resonance frequency to that of a particle with a 100 nm diameter, even though the actual diameter varied from 60 to 140 nm.

Figure 6.28 compares new results with limited data (the right column) to the previous results with extensive data (the left column). The coupling and damping constants attributed to the particle oscillator deviate from the previous result, particularly for particles larger than 100 nm. In this retrial, the upper and lower limits were 3 and -3; both ω_{PB}^2 and ω_{PD}^2 reach their boundary values, which is an indicator of overfitting, as we have seen earlier. The other parameters still show a good agreement in their magnitudes and the overall trend. Therefore, if ω_{PB}^2 and ω_{PD}^2 are close to their respective boundary values, we can regard it as the case for particles being larger than 100 nm, and we must instead refer to ω_{BP}^2 and ω_{DP}^2 in order to analyze the coupling strength.

Experimental fitting using three coupled oscillators

With this understanding of which parameters are subject to overfitting errors, we performed the analysis with the experimental data, which was our ultimate goal. Similar to the simulation analysis, we utilized the parameters describing the measured nanoflowers before particle trapping and a randomly measured particle. These parameters were determined earlier (Figure 6.17 for nanoflowers and Figure 6.13b for the nanoparticle) when we introduced the single and two-coupled oscillator models. We fixed the values for the resonant frequencies

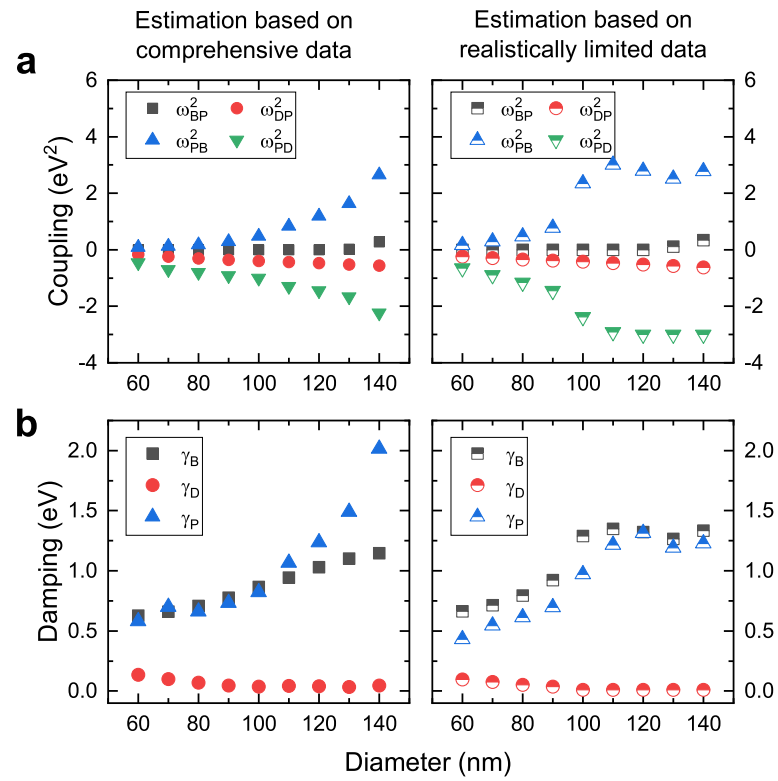


Figure 6.28 – Comparing parameters obtained with limited information (the right column) to the previous results with extensive information (the left column) while varying the particle diameter. **a**, The four coupling constants (squared resonant frequencies). **b**, the three damping constants.

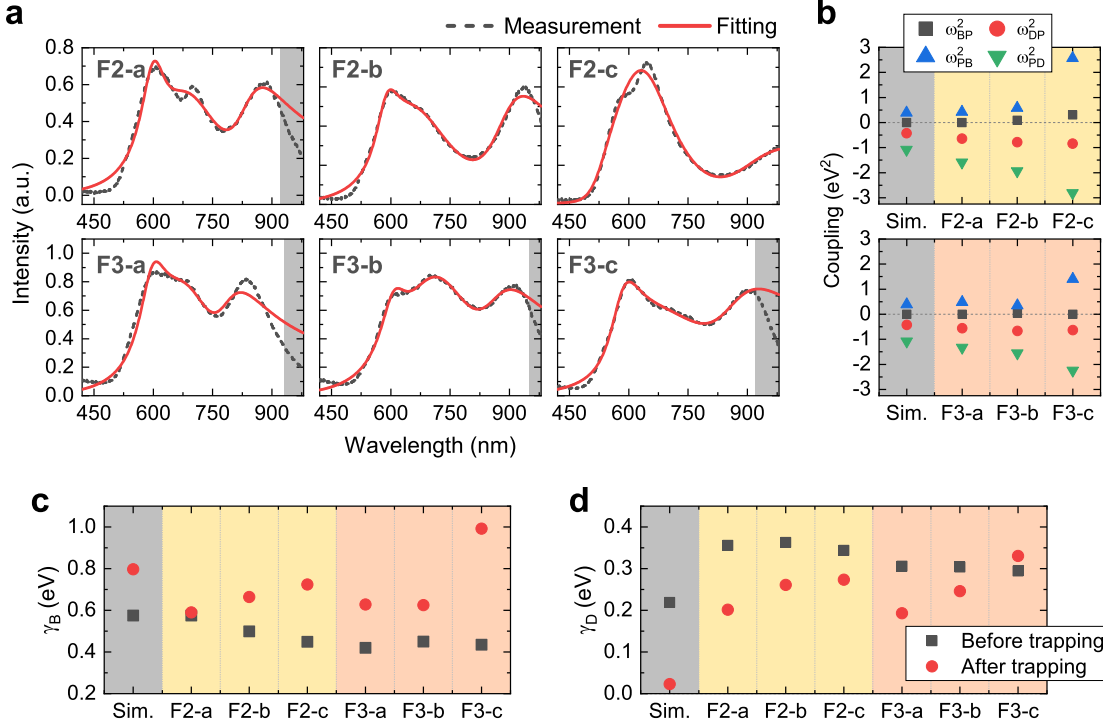


Figure 6.29 – Three-coupled oscillator model applied to measured spectra. **a**, Measured nanoflower spectra with the F2 and F3 designs (the grey dashed lines) and fitting results (the red solid lines). The shaded areas of the spectral regions were excluded from fitting due to overfitting issues. **b**, Fitting parameters used to construct the curves in **a**. The reference values for simulation were with a 100 nm nanoparticle at $z_{\text{offset}} = 0$. **c**, **d**, Damping constants for the bright and dark modes, respectively. The values before and after trapping are plotted together for comparison.

and estimated the remaining parameters. Constraints and boundary conditions were identical to those shown in Table 6.5.

Figure 6.29a shows the measured spectra in grey dashed lines and the fitted spectra in red solid lines. We arranged the spectra by the width of the Fano interference dips such that they get wider from left to right. Compared to the simulation data, the experimental spectra contain an additional peak near the peak on the shorter wavelength side. Surprisingly, the three-coupled oscillator model also accounts for the majority of these unexpected peaks.

Importantly, we can obtain quantitative insights into the spectra of the coupled system. From the spectra in Figure 6.29a, we expect that the coupling between the nanoflower and the particle becomes stronger as the spectral splitting becomes more pronounced both in the F2 and F3 designs (except for F3-a and F3-b, for which the splittings seem comparable). The estimated parameters in Figure 6.29b strongly support this idea. In the case of the F2 design, the magnitudes of all four coupling constants increase for the three example spectra. We should pay attention that ω_{PB}^2 and ω_{PD}^2 are close to their respective boundary values in F2-c,

but both ω_{BP}^2 and ω_{DP}^2 also show an increase. Therefore, F2-c could be the case for trapping a large particle (possibly larger than 100 nm).

In the case of the F3 design, the coupling parameters for F3-c are substantially more extensive than those of F3-a and F3-b, whereas the parameters between F3-a and F3-b appear comparable. This trend corresponds well with our spectral observations and interpretations. On top of that, the overall F3's coupling parameters have relatively smaller magnitudes compared to those with the F2 design. One possible explanation is that the large pocket size in the F3 design makes particles of the same size relatively small compared to the F2 design, causing the overall couplings to be weak.

The damping constants in Figures 6.29c and d, on the other hand, provide evidence from a different perspective. We previously explained the increase in γ_B as a result of bonding behaviors. The difference in γ_B before and after trapping increases in the F2 case, indicating that the coupling becomes stronger. In the case of F3, the difference abruptly increases at F3-c, in line with the spectral observations and estimated coupling constants. In other words, changes in γ_B provide the same interpretation of coupling strengths.

On the contrary, the damping constants for the dark mode, γ_D , behave quite differently than we would expect based on coupling constants. We would expect a smaller γ_D with a stronger coupling; however, we found the opposite behavior of γ_D in Figure 6.29d. We previously related the decreasing γ_D with reduced radiative damping. A prerequisite for successful radiation suppression was the effective cancellation of dipole moments among the petals as well as the particle. In contrast to the simulation meshes, the actual nanoflowers have random variations in their shapes. This randomness has the potential to prevent the effective cancellation of dipole moments observed in simulations. This practical issue may explain why we do not observe deep troughs in the measured spectra and why the estimated values of γ_D are larger than those of the simulation. As a result, it is difficult to draw a meaningful interpretation regarding coupling strengths from γ_D .

6.3.5 Possible mechanisms for particle immobilization

Aside from the coupling analysis in the tweezer-assembled structures, the question of how the particle is permanently immobilized while being trapped remains unanswered. From our previous study in Chapter 4, we discovered a unique fusion of bilayer membranes when particles approached close to the activated glass surfaces. Indeed, we often observed that the particles' lateral movement decreased as they stayed longer in the optical trap, and a part of them eventually became permanently stuck on the glass surfaces. This is the case when the bilayer membranes collapse and the particles are completely fixed to the substrate by the Van der Waals force. Since we did not observe such behaviors with bare glass substrates where the surfactants form spherical aggregates on glass surfaces (Chapter 4), we assumed that the formation of bilayer membranes on both the particle and glass surfaces is the necessary condition to observe membrane fusion. Furthermore, from the comparison between gold and

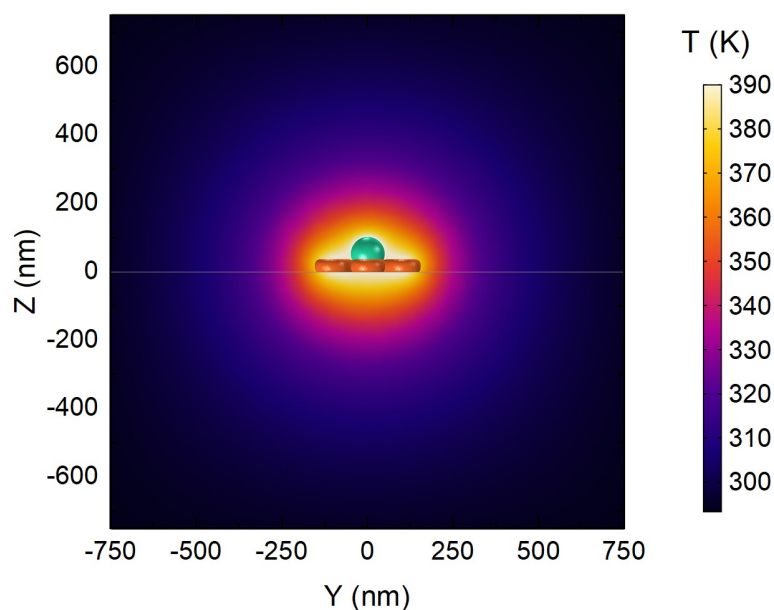


Figure 6.30 – Temperature distribution around the nanoflower with a 100 nm trapped particle. Details about the heating simulation can be found in Appendix 2.5.

polystyrene particles (Chapter 3), we concluded that the optical heating by the trapping laser can promote active rearrangements of surfactant molecules located in between the particle and glass surfaces.

Based on these previous experimental findings, we can speculate a possible mechanism of particle immobilization in our trapping experiments in the presence of nanoflowers. We know that CTAC surfactants form bilayers on gold surfaces [130, 135], which corresponds to both the particle surface and the nanoflower surfaces on glass substrates. In addition, when the trapping laser shines on both the particle and the nanoflower at the same time, we can expect a higher temperature rise than those with only a particle since the flower itself is an additional heat source. Figure 6.30 shows a temperature calculation with a nanoflower and a 100 nm particle. In comparison to the temperature rise of 73 K with just the particle (Figure 3.7 in Section 2.5 for more details), the temperature at the nanoflower-particle gap has risen by 102 K from the initial room temperature (293 K). This higher temperature increases the likelihood of particles colliding with the nanoflower with high energy, which can result in particle immobilization due to the collapse of electric double layers.

6.4 Conclusion

We studied the interaction between nanoflowers and nanoparticles by optically positioning the particles inside the pockets of the nanoflowers, analogous to creating plasmonic heptamers by introducing central particles to ringlike hexamers. We measured and analyzed the spectral changes caused by particle trapping, which can provide insights into their optical interactions.

To that end, we first investigated the force exerted on particles in the presence of nanoflowers. In contrast to the conventional understanding that plasmonic nanoantennas enhance the trapping efficiency and stiffness, the near-fields of nanoflowers generate forces that push the particle outward due to their unique hollow geometry. We were able to overcome this force in practice by employing a focused laser beam, which produced a gradient force strong enough to allow independent control over the particles. In addition, we used numerical simulation to investigate the probable spectral changes after particle trapping by varying the particle positions and sizes.

Although the simulation results were insightful, we discovered discrepancies between the simulated and measured outcomes. To better comprehend these differences, we introduced the well-known coupled oscillator model. Starting with the simplest single oscillator model to describe the response of a single nanoparticle, we progressively increased the model's complexity until we could describe the response of the entire system with three coupled oscillators. Utilizing model parameters such as spring constants and damping constants, we unveiled the relationship between numerical results and coupling strengths. Finally, we extended this understanding to measured data.

Assembling heterogeneous nanostructures in one place can become a breakthrough in the creation of new materials and three-dimensional systems. In this chapter, we demonstrated the possibility of assembling lithographically fabricated nanoscale structures with colloidal nanoparticles or, in a broader context, hierarchically bridging top-down and bottom-up processes. Furthermore, we demonstrated that the coupled oscillator model can provide valuable insights into the systematic identification and interpretation of the near-field coupling created by optical tweezers. With the help of such a simple and intuitive model, we can enhance our understanding of tweezer-organized structures that are otherwise difficult to quantify.

7 Conclusions and outlook

In summary, we have discussed the comprehensive applications of optical tweezers in two fields: surface chemistry and nano-optics. The primary objective of this study was to develop a method for assembling heterogeneous nanostructures into a complex optical system, a key technology for a future nanofactory. During the pursuit of this objective, interesting discoveries were made, all of which contributed to the final realization of the goal. This thesis is a compilation of several previously published articles reporting these discoveries, which we have expanded and modified to form a coherent text. In the following sections, we will walk through the overall summary, the limitations of the methodology used in this thesis, and finally, potential avenues for future research.

7.1 Summary

First, we discussed the interaction between a particle and a nearby surface in Chapter 3. On the movement of trapped particles, particular focus was given to the effect of surfactants, which are commonly added to colloidal solutions and adsorb on all surfaces. As one of the plausible interaction mechanisms between the particle and the adsorbed molecules, the thermal effect induced by optical heating of the particle was proposed. This thermal effect was investigated by comparing the movement of metallic and dielectric nanoparticles in an optical trap. This study concluded that optical heating of a trapped particle can induce rearrangement of neighboring molecules, thereby altering the particle's motion. The findings of Chapter 3 will aid in our comprehension of particle behaviors when metallic particles are trapped in a complex environment where surface effects are unavoidable.

In Chapter 4, inspired by the observation in Chapter 3 that the nanoparticle motion reflects interactions with surrounding molecules, we proposed the use of nanoparticles as optical probes in surface science. Surfactants in particular formed a double layer structure on the surface of gold nanoparticles, and particle motion analysis revealed that this double layer fused with the double layer present on a nearby glass surface. This evidence demonstrates that nanoparticles can become actively involved in the interactions of surrounding molecules

and monitor the process simultaneously.

The heating effect of optical tweezers on gold nanoparticles in Chapter 3 and the active participation of gold nanoparticles in molecular interactions in Chapter 4 suggest that an optically trapped metallic nanoparticle can serve as a nanoscale heating probe that can apply heat locally and simultaneously observe heat-induced phenomena. Due to the prevalence of thermally-induced effects, this will have applications in all fields of science, including, but not limited to, biology, chemistry, thermodynamics, microfluidics, and nano-optics. If such a thermal effect is undesirable, fluorescent dielectric particles can be substituted for metallic particles (Chapter 3), or the trapping laser's wavelength can be chosen to be far from the resonance wavelength of the target metallic particles, such as in the infrared region [191–194].

In the subsequent chapters, Chapter 5 and 6, we theoretically investigated optical forces and experimentally implemented complex optical assemblies using the optical tweezer. In Chapter 5, the theoretical foundation for the optical assembly was established. We investigated the optical forces modifications caused by the interaction of a metallic particle and a plasmonic dipole antenna. Surprisingly, the dipole approximation method that assumes no field perturbation by the particle performed comparably to the self-consistent Maxwell's stress tensor method, particularly for particles much smaller than the trapping wavelength ($< \lambda/40$). We also investigated the optical force in systems with larger particles whose dimensions exceeded the dipole approximation's range. Due to the interaction with the plasmonic antenna, the polarization of large particles became considerably more complex than a simple dipole, and intriguing coupling behaviors emerged.

Based on this theoretical understanding of optical force, in Chapter 6, we experimentally demonstrated the organization of a nanoparticle–nanoantenna assembly using the same optical tweezers described in Chapters 3 and 4, which was the overarching aim of this thesis. Initially, we struggled to achieve stable trapping of gold nanoparticles using the dipole antenna investigated in Chapter 5. We were able to circumvent this problem by employing a nanoflower design with a central cavity capable of accommodating a particle. We were eventually able to trap a particle inside, and as a result, a significant spectral change was observed. The numerical simulation as well as the comprehensive analysis based on the coupled oscillator model provided valuable insights into the nanoflower–nanoparticle coupling. Using in particular the coupled oscillator model, we gained a quantitative understanding of the optical response from tweezer-assembled structures and discussed the limitations of their real-world implementation.

7.2 Limitations

Video-based position detection

For the single-particle tracking (SPT) in Chapter 3 and 4, we used a CMOS camera to visualize and record the movement of trapped particles at the same time. In the case of video-based

position detection, the framerate of the camera determines the temporal resolution of the time-series trajectory. In our case, the framerate was typically about 350 frames per second, and the temporal resolution was therefore constrained to about 3 ms. This framerate is relatively higher than the typical frame rates of CCD cameras (25–120 Hz) [62], but still, the temporal resolution of about 3 ms could obscure numerous processes that occur on a shorter time scale [226].

High-speed CMOS cameras can be used to improve the temporal resolution [119, 120, 226]. Wu *et al.* [226], for instance, used a high-speed CMOS camera to record videos at 50 kHz, which corresponds to a temporal resolution of 20 μ s. A practical issue with this high-speed video microscopy is memory capacity as the data size can become excessively large at such a high framerate. Consequently, a typical recording duration is restricted to a few seconds due to the limited amount of on-board memory storage [119]. An alternative way for position detection is to use a quadrant photodiode (QPD) [24, 62, 227, 228]. Using a QPD enables displacement measurements in nanometer resolution at tens of kHz [228]. These alternative methods can be more appropriate for SPT; in our study, the SPT was not the primary focus of the project, so we used a standard imaging CMOS camera for position detection.

Nanofabrication

We used electron-beam lithography combined with a lift-off technique to fabricate nanoantennas. During this process, a gold film was deposited on top of the double-layer resist mask, forming nanoclusters that can impart a textured appearance to the final structures (Figure 7.1a). These metal atoms can also diffuse into the undercut structure of the double-layer resist, distorting the structure's outline and causing irregularities [229]. Furthermore, when the nanostructure contained a void, the lift-off process was sometimes unsuccessful, and the residual resist remained in the void (Figure 7.1b). These residues were invisible under an optical microscope. However, experiments revealed that certain batches of nanoflower arrays exhibited optical responses that deviated from the simulated response. This may have occurred when the lift-off was unsuccessful and the resist clogged the central void. With these nanoantennas, trapping nanoparticles failed as a natural consequence.

This issue can be avoided by employing a negative electron-beam resist followed by ion beam milling. Abasahl *et al.* [229] compared the fabrication results of lift-off and ion-beam etching and found that the etching approach created nanostructures with better definitions. When it comes to nanostructures that support Fano resonances, the benefit of having uniform shapes can be more pronounced. Unfortunately, due to time constraints, the etching technique was not tested in this thesis.

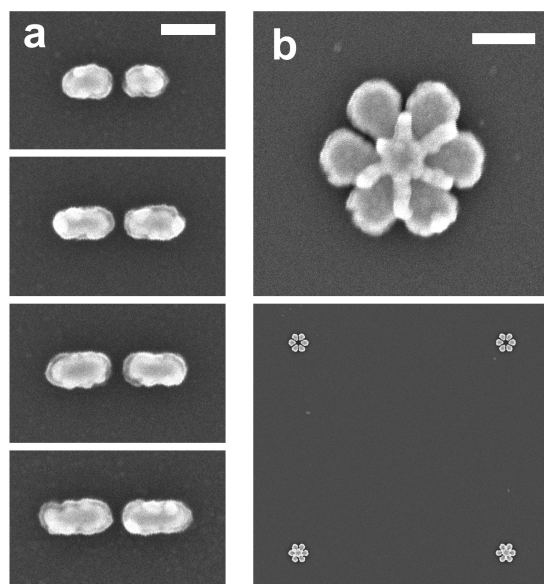


Figure 7.1 – Scanning electron microscope images of nanostructures defined by electron-beam lithography and lift-off process. **a**, Dipole nanoantenna examples with different lengths. Scale bar, 100 nm. **b**, (top) Nanoflower example with a resist residue at the central void. Scale bar, 100 nm. (bottom) Low magnification image of nanoflower array. The two nanoflowers on the bottom row have residual resists.

7.3 Future research

Since the initial discovery of optical gradient and scattering forces in 1970, optical tweezers have contributed to numerous scientific fields as a powerful tool for unraveling mysteries and advancing our understanding of the microscopic world [230]. The new opportunities demonstrated in this dissertation, particularly with the gold nanoparticles, are still in their infancy. Here, we propose several avenues for future research to develop the presented ideas further.

3D single particle tracking

We have examined the particle's trajectories in two dimensions parallel to the solid-liquid interface, which is the most basic way to observe and analyze its motion. For interfacial analysis, a three-dimensional (3D) trajectory can offer exciting opportunities to grasp more complex dynamics at an interface. There exist numerous 3D imaging techniques and axial position detection techniques that can be readily implemented [231–238]. Using a quadrant photodiode, for instance, could be one of the straightforward methods with an optical tweezer setup: measuring the ratio of scattered intensity to total intensity can simply provide the axial information of trapped particles [24, 227].

Photo-polymerization

The heat caused by the absorption of gold nanoparticles can be utilized in photo-polymerization processes [239, 240]. Two-photon polymerization has proven to be successful in microfabrication for rapid prototyping of three-dimensional structures [241]. With this method, gold nanoparticles and other metallic particles can also be assembled and permanently bonded

using an optical tweezer [242]. Due to their sensitivity to environmental changes, plasmonic resonances can also be finely tuned through the regulation of polymer growth [239, 243]. If we can control this growth with a trapping laser (e.g., by adjusting the power or duration of the illumination), we can obtain three processes in one place with a single laser: trapping, assembling (including fixation), and controlling the coupling by adjusting the gap distance between particles via polymer growth.

Hybrid nanoantenna

Hybrid metal-dielectric nanostructures have recently gained interest due to their ability to leverage the complementary benefits of both materials, namely the strong field enhancement of plasmonic nanostructures and the low loss and high directivity of dielectric resonators [244–246]. For instance, a sandwich structure consisting of an aluminum disk and silicon cylinder was investigated in our group [246], which was fabricated through a series of lithographic and chemical processing steps. If large-area fabrication is not a concern, then an optical tweezer can provide an alternative way to realize such a hybrid nanoantenna by hierarchically organizing metallic and dielectric nanostructures.

Highly integrated optical manufacturing

With the emerging possibilities associated with optical tweezers, including photo-chemistry and hierarchical assembly, one could imagine an optical nanofactory built on a microfluidic channel acting like a conveyor belt. While microfluidics provides a flow, optical tweezers can synthesize [247], sort [248], trap [62], and assemble [13] all in one place with a single instrument. This could be a scene for building future nano-robots or nano-machines [249, 250].

A Interaction force between admicelles and trapped particles

The DLVO theory [251–253] predicts an interaction force between charged colloidal particles in a liquid medium. It assumes that the force is the sum of the van der Waals force and the electrostatic force. In most cases, the van der Waals force is attractive, and for liked charged objects, the electrostatic force is repulsive. We estimated the interaction force between a trapped gold nanoparticle and a micelle adsorbed on the glass wall using the DLVO theory.

Estimating the van der Waals interaction between gold nanoparticles and micelles on the glass surface is not a trivial problem. The system consists of a gold nanoparticle with a CTAC layer and a silica surface with adsorbed micelles, mediated with water. The surfactant layers on both surfaces prevent the particle from coming close to the glass surface. Biggs & Mulvaney [254] observed that the force is always repulsive between a gold plate and a 3.3 μm gold-coated silica sphere in the presence of 1.5 mM CTAB at all separations from 0 to 35 nm. They described that the gold surfaces do not come into contact at the pressures of their experiment due to the adsorbed CTAB layers. Giesbers *et al.* Giesbers *et al.* also reported similar repulsive interactions between a gold film and a 6 μm gold-coated silica sphere with no indication of attractive van der Waals forces. They explained that the hydration and surface roughness effect may have obscured van der Waals forces.

Although it seems that the actual van der Waals force can be smaller in real systems, we estimate the van der Waals force, F_{vdW} , using the simplest expression within Derjaguin approximation [256],

$$F_{\text{vdW}} = -\frac{A}{12h^2} R_{\text{eff}}, \quad (\text{S1})$$

where

- A is the Hamaker constant, defining the strength of the van der Waals interaction,
- h is the separation distance between the gold nanoparticle and the micelle,

- R_{eff} is the effective radius, which is given by

$$R_{\text{eff}} = \frac{R_{\text{Au}} R_m}{R_{\text{Au}} + R_m} \approx 2.88[\text{nm}],$$

where R_{NP} is the radius of the gold nanoparticle (75 nm), and R_m the radius of the admicelle (3 nm, measured by dynamic light scattering).

We use the value for the Hamaker constant, $A = 5.7 \times 10^{-20}$ J for a gold-water-silica system [257]. The actual Hamaker constant, however, can be smaller due to the reasons mentioned above.

On the other hand, the electrostatic force (F_{dl}) owing to the electrical double layers can be approximated to have the following form:

$$F_{\text{dl}} = -2\pi\epsilon_0\epsilon\psi_{\text{dl}}^2 R_{\text{eff}} e^{-\kappa_D h}, \quad (\text{S2})$$

where

- ϵ_0 is the vacuum permittivity,
- ϵ is the dielectric constant of water at room temperature (78.4 at 25 °C),
- ψ_{dl} is the electric potential of the diffuse double layer,
- κ_D is the Debye screening wavevector, whose inverse is the Debye length ($\lambda_D = \kappa_D^{-1}$).

The Debye length (κ_D^{-1}) for a monovalent electrolyte at room temperature can be approximated as

$$\kappa_D^{-1} [\text{nm}] = \frac{0.304}{\sqrt{I[\text{M}]}} = \frac{0.304}{\sqrt{0.001}} \approx 9.6[\text{nm}],$$

where

- κ_D^{-1} is expressed in nanometers (nm),
- I is the ionic strength in molar concentration (M or mol/L), and we put 1 mM for CTAC concentration at which the interaction between the gold nanoparticle and the admicelles seems most significant from Figure 2b.

The electric potentials of the double layer for the gold nanoparticles and the micelles are required to calculate the double layer force, F_{dl} . The electrophoretic mobility of the gold colloids at 1.0 mM CTAC and the micelles at 5.0 mM CTAC were measured with dynamic light scattering as described in the Methods section in the main manuscript. The admicelle properties were assumed to be the same as the bulk micelle properties. The CTAC concentration of 5 mM above the CMC was used for micelle measurements to ensure micelle formation in the bulk

Table A.1 – Measured electrophoretic mobility and double layer potential

| | Gold nanoparticles at 1 mM CTAC | Bulk micelles at 5 mM CTAC |
|--|------------------------------------|-------------------------------|
| Electrophoretic mobility ($\mu\text{m}\cdot\text{cm}/\text{V}\cdot\text{s}$) | 3.42 ± 0.5 | 4.89 ± 0.55 |
| Apparent ζ potentials (mV) | 43.7 ± 6.3 | 62.4 ± 7.0 |
| Double layer potential, ψ_{dl} (mV) | 16.08 | 22.96 |

and high signal count rates. The apparent zeta potentials were inferred from the measured electrophoretic mobility using the Smoluchowski approximation. [105] At the diffuse electrical double layer boundary, the electric potential decreases in magnitude by $1/e$ by electrical screening. Table A.1 shows the measured values and inferred double layer potentials used for force calculation.

By combining the van der Waals force in Equation S1 and the double layer force in Equation S2, we can compute the net force acting on the particle and the admicelle:

$$\mathbf{F}_{\text{DLVO}} = \mathbf{F}_{\text{vdW}} + \mathbf{F}_{\text{dl}} \quad (\text{S3})$$

Figure 3.9 shows these forces calculated as a function of separation distance, h . The force remains repulsive down to $h = 2$ nm. Since the CTAC bilayer thickness is about 4 nm [159], the separation h should be larger than 4 nm, which implies that the force is always repulsive. The maximum repulsive force also occurs at this distance (~ 4.4 nm).

Bibliography

1. Feynman, R. P. There's plenty of room at the bottom. *Eng. Sci.* **23**, 22–36 (1960).
2. Dietrich, J. S. Tiny Tale Gets Grand. *Eng. Sci.* **49**, 25–26 (1986).
3. Binnig, G., Rohrer, H., Gerber, C. & Weibel, E. Surface Studies by Scanning Tunneling Microscopy. *Phys. Rev. Lett.* **49**, 57–61 (1982).
4. Binnig, G., Rohrer, H., Gerber, C. & Weibel, E. Tunneling through a controllable vacuum gap. *Appl. Phys. Lett.* **40**, 178–180 (1982).
5. Binnig, G. & Rohrer, H. Scanning tunneling microscopy. *Surf. Sci.* **126**, 236–244 (1983).
6. Becker, R. S., Golovchenko, J. A. & Swartzentruber, B. S. Atomic-scale surface modifications using a tunnelling microscope. *Nature* **325**, 419–421 (1987).
7. Foster, J. S., Frommer, J. E. & Arnett, P. C. Molecular manipulation using a tunnelling microscope. *Nature* **331**, 324–326 (1988).
8. Eigler, D. M. & Schweizer, E. K. Positioning single atoms with a scanning tunnelling microscope. *Nature* **344**, 524–526 (1990).
9. Ashkin, A. Acceleration and Trapping of Particles by Radiation Pressure. *Phys. Rev. Lett.* **24**, 156–159 (1970).
10. Won, R. How it all began. *Nat. Photon.* **5**, 316–317 (2011).
11. Ashkin, A., Dziedzic, J. M., Bjorkholm, J. E. & Chu, S. Observation of a Single-Beam Gradient Force Optical Trap for Dielectric Particles. *Opt. Lett.* **11**, 288–290 (1986).
12. Chu, S., Bjorkholm, J. E., Ashkin, A. & Cable, A. Experimental Observation of Optically Trapped Atoms. *Phys. Rev. Lett.* **57**, 314–317 (1986).
13. Grier, D. G. A Revolution in Optical Manipulation. *Nature* **424**, 810–816 (2003).
14. Bowman, R. W. & Padgett, M. J. Optical Trapping and Binding. *Rep. Prog. Phys.* **76**, 026401 (2013).
15. Maragò, O. M., Jones, P. H., Gucciardi, P. G., Volpe, G. & Ferrari, A. C. Optical Trapping and Manipulation of Nanostructures. *Nat. Nanotechnol.* **8**, 807 (2013).
16. Ashkin, A. & Dziedzic, J. M. Optical Trapping and Manipulation of Viruses and Bacteria. *Science* **235**, 1517–1520 (1987).

17. Min, T. L. *et al.* High-Resolution, Long-Term Characterization of Bacterial Motility Using Optical Tweezers. *Nat. Methods* **6**, 831–835 (2009).
18. Pang, Y., Song, H., Kim, J. H., Hou, X. & Cheng, W. Optical Trapping of Individual Human Immunodeficiency Viruses in Culture Fluid Reveals Heterogeneity With Single-Molecule Resolution. *Nat. Nanotechnol.* **9**, 624–630 (2014).
19. Svoboda, K., Schmidt, C. F., Schnapp, B. J. & Block, S. M. Direct Observation of Kinesin Stepping by Optical Trapping Interferometry. *Nature* **365**, 721–727 (1993).
20. Molloy, J. E., Burns, J. E., Kendrick-Jones, J., Tregear, R. T. & White, D. C. S. Movement and Force Produced by a Single Myosin Head. *Nature* **378**, 209–212 (1995).
21. Wang, M., Yin, H., Landick, R., Gelles, J. & Block, S. Stretching DNA with Optical Tweezers. *Biophys. J.* **72**, 1335–1346 (1997).
22. Grier, D. G. Optical Tweezers in Colloid and Interface Science. *Curr. Opin. Colloid Interface Sci.* **2**, 264–270 (1997).
23. Polin, M., Grier, D. G. & Quake, S. R. Anomalous Vibrational Dispersion in Holographically Trapped Colloidal Arrays. *Phys. Rev. Lett.* **96**, 088101 (2006).
24. Franosch, T. *et al.* Resonances Arising From Hydrodynamic Memory in Brownian Motion. *Nature* **478**, 85–88 (2011).
25. McCann, L. I., Dykman, M. & Golding, B. Thermally Activated Transitions in a Bistable Three-Dimensional Optical Trap. *Nature* **402**, 785–787 (1999).
26. Carberry, D. M. *et al.* Fluctuations and Irreversibility: An Experimental Demonstration of a Second-Law-Like Theorem Using a Colloidal Particle Held in an Optical Trap. *Phys. Rev. Lett.* **92**, 140601 (2004).
27. Bérut, A. *et al.* Experimental verification of Landauer's principle linking information and thermodynamics. *Nature* **483**, 187–189 (2012).
28. Saxton, M. J. & Jacobson, K. SINGLE-PARTICLE TRACKING: Applications to Membrane Dynamics. *Annu. Rev. Biophys. Biomol. Struct.* **26**, 373–399 (1997).
29. Kukura, P. *et al.* High-speed nanoscopic tracking of the position and orientation of a single virus. *Nat. Methods* **6**, 923–927 (2009).
30. Shen, H. *et al.* Single Particle Tracking: From Theory to Biophysical Applications. *Chem. Rev.* **117**, 7331–7376 (2017).
31. Gahlmann, A. & Moerner, W. E. Exploring Bacterial Cell Biology with Single-Molecule Tracking and Super-Resolution Imaging. *Nat. Rev. Microbiol.* **12**, 9 (2014).
32. Ruthardt, N., Lamb, D. C. & Bräuchle, C. Single-particle Tracking as a Quantitative Microscopy-based Approach to Unravel Cell Entry Mechanisms of Viruses and Pharmaceutical Nanoparticles. *Mol. Ther.* **19**, 1199–1211 (2011).
33. Manzo, C. & Garcia-Parajo, M. F. A review of progress in single particle tracking: from methods to biophysical insights. *Rep. Prog. Phys.* **78**, 124601 (2015).

BIBLIOGRAPHY

34. Taylor, R. W. *et al.* Interferometric scattering microscopy reveals microsecond nanoscopic protein motion on a live cell membrane. *Nat. Photon.* **13**, 480–487 (2019).
35. Lang, M. J., Fordyce, P. M., Engh, A. M., Neuman, K. C. & Block, S. M. Simultaneous, coincident optical trapping and single-molecule fluorescence. *Nat. Methods* **1**, 133–139 (2004).
36. Bustamante, C. J., Chemla, Y. R., Liu, S. & Wang, M. D. Optical tweezers in single-molecule biophysics. *Nat. Rev. Methods Primers* **1**, 25 (2021).
37. Yao, A., Tassieri, M., Padgett, M. & Cooper, J. Microrheology with Optical Tweezers. *Lab Chip* **9**, 2568–2575 (17 2009).
38. Walder, R., Nelson, N. & Schwartz, D. K. Single Molecule Observations of Desorption-Mediated Diffusion at the Solid-Liquid Interface. *Phys. Rev. Lett.* **107**, 156102 (2011).
39. Skaug, M. J., Mabry, J. N. & Schwartz, D. K. Single-Molecule Tracking of Polymer Surface Diffusion. *J. Am. Chem. Soc.* **136**, 1327–1332 (2014).
40. Higgins, D. A., Park, S. C., Tran-Ba, K.-H. & Ito, T. Single-Molecule Investigations of Morphology and Mass Transport Dynamics in Nanostructured Materials. *Annu. Rev. Anal. Chem.* **8**, 193–216 (2015).
41. Dong, B. *et al.* In situ quantitative single-molecule study of dynamic catalytic processes in nanoconfinement. *Nat. Catal.* **1**, 135–140 (2018).
42. Zhong, Y. & Wang, G. Three-Dimensional Single Particle Tracking and Its Applications in Confined Environments. *Annu. Rev. Anal. Chem.* **13**, 381–403 (2020).
43. Novotny, L. & Hecht, B. *Principles of Nano-Optics* 2nd ed. (Cambridge University, Cambridge, 2012).
44. Sandoghdar, V. Nano-Optics in 2020 \pm 20. *Nano Lett.* **20**, 4721–4723 (2020).
45. Maier, S. *Plasmonics: Fundamentals and Applications* (Springer, New York, NY, 2007).
46. Barrow, S. J., Funston, A. M., Gómez, D. E., Davis, T. J. & Mulvaney, P. Surface Plasmon Resonances in Strongly Coupled Gold Nanosphere Chains from Monomer to Hexamer. *Nano Lett.* **11**, 4180–4187 (2011).
47. Luk'yanchuk, B. *et al.* The Fano resonance in plasmonic nanostructures and metamaterials. *Nat. Mater.* **9**, 707–715 (2010).
48. Gallinet, B. & Martin, O. J. F. Influence of Electromagnetic Interactions on the Line Shape of Plasmonic Fano Resonances. *ACS Nano* **5**, 8999–9008 (2011).
49. Lovera, A., Gallinet, B., Nordlander, P. & Martin, O. J. F. Mechanisms of Fano Resonances in Coupled Plasmonic Systems. *ACS Nano* **7**, 4527–4536 (2013).
50. Davis, T. J. & Hendry, E. Superchiral electromagnetic fields created by surface plasmons in nonchiral metallic nanostructures. *Phys. Rev. B* **87**, 085405 (2013).
51. Yoo, S. & Park, Q.-H. Chiral Light-Matter Interaction in Optical Resonators. *Phys. Rev. Lett.* **114**, 203003 (2015).

52. Hentschel, M., Schäferling, M., Duan, X., Giessen, H. & Liu, N. Chiral plasmonics. *Sci. Adv.* **3**, e1602735 (2017).
53. Yoo, S. & Park, Q.-H. Metamaterials and chiral sensing: a review of fundamentals and applications. *Nanophotonics* **8**, 249–261 (2019).
54. Butet, J., Brevet, P.-F. & Martin, O. J. F. Optical Second Harmonic Generation in Plasmonic Nanostructures: From Fundamental Principles to Advanced Applications. *ACS Nano* **9**, 10545–10562 (2015).
55. Terray, A., Oakey, J. & Marr, D. W. M. Fabrication of linear colloidal structures for microfluidic applications. *Appl. Phys. Lett.* **81**, 1555–1557 (2002).
56. Roichman, Y. & Grier, D. G. Holographic assembly of quasicrystalline photonic heterostructures. *Opt. Express* **13**, 5434–5439 (2005).
57. Agarwal, R. *et al.* Manipulation and assembly of nanowires with holographic optical traps. *Opt. Express* **13**, 8906–8912 (2005).
58. Urban, A. S., Lutich, A. A., Stefani, F. D. & Feldmann, J. Laser Printing Single Gold Nanoparticles. *Nano Lett.* **10**, 4794–4798 (2010).
59. Guffey, M. J. & Scherer, N. F. All-Optical Patterning of Au Nanoparticles on Surfaces Using Optical Traps. *Nano Lett.* **10**, 4302–4308 (2010).
60. Gargiulo, J., Cerrota, S., Cortés, E., Violi, I. L. & Stefani, F. D. Connecting Metallic Nanoparticles by Optical Printing. *Nano Lett.* **16**, 1224–1229 (2016).
61. Do, J. *et al.* Photonic Crystal Nanocavities Containing Plasmonic Nanoparticles Assembled Using a Laser-Printing Technique. *Adv. Opt. Mater.* **1**, 946–951 (2013).
62. Neuman, K. C. & Block, S. M. Optical Trapping. *Rev. Sci. Instrum.* **75**, 2787–2809 (2004).
63. Constable, A., Kim, J., Mervis, J., Zarinetchi, F. & Prentiss, M. Demonstration of a fiber-optical light-force trap. *Opt. Lett.* **18**, 1867–1869 (1993).
64. Grier, D. G. & Roichman, Y. Holographic optical trapping. *Appl. Opt.* **45**, 880–887 (2006).
65. Gordon, J. P. Radiation Forces and Momenta in Dielectric Media. *Phys. Rev. A* **8**, 14–21 (1973).
66. Chaumet, P. C. & Nieto-Vesperinas, M. Time-averaged total force on a dipolar sphere in an electromagnetic field. *Opt. Lett.* **25**, 1065–1067 (2000).
67. Arias-Gonzalez, J. R. & Nieto-Vesperinas, M. Optical forces on small particles: attractive and repulsive nature and plasmon-resonance conditions. *J. Opt. Soc. Am. A: Opt. Image Sci. Vis.* **20**, 1201–1209 (2003).
68. Nieto-Vesperinas, M., Chaumet, P. C. & Rahmani, A. Near-field photonic forces. *Philos. Trans. Royal Soc. A* **362**, 719–737 (2004).
69. Nieto-Vesperinas, M., Sáenz, J. J., Gómez-Medina, R. & Chantada, L. Optical forces on small magnetodielectric particles. *Opt. Express* **18**, 11428–11443 (2010).

BIBLIOGRAPHY

70. Kim, J. & Martin, O. J. F. Studying the different coupling regimes for a plasmonic particle in a plasmonic trap. *Opt. Express* **27**, 38670–38682 (2019).
71. Kiselev, A., Achouri, K. & Martin, O. J. F. Electromagnetic forces in the time domain. *Opt. Express* **30**, 32215–32229 (2022).
72. Riccardi, M., Kiselev, A., Achouri, K. & Martin, O. J. F. Multipolar expansions for scattering and optical force calculations beyond the long wavelength approximation. *Phys. Rev. B* **106**, 115428 (2022).
73. Bradac, C. Nanoscale Optical Trapping: A Review. *Adv. Opt. Mater.* **6**, 1800005 (2018).
74. Bohren, C. F. & Huffman, D. R. *Absorption and Scattering of Light by Small Particles* (Wiley Interscience, 1983).
75. Barnes, W. L., Dereux, A. & Ebbesen, T. W. Surface plasmon subwavelength optics. *Nature* **424**, 824–830 (2003).
76. Schuller, J. A. *et al.* Plasmonics for extreme light concentration and manipulation. *Nat. Mater.* **9**, 193–204 (2010).
77. Eustis, S. & El-Sayed, M. A. Why gold nanoparticles are more precious than pretty gold: Noble metal surface plasmon resonance and its enhancement of the radiative and nonradiative properties of nanocrystals of different shapes. *Chem. Soc. Rev.* **35**, 209–217 (3 2006).
78. Atwater, H. A. & Polman, A. Plasmonics for improved photovoltaic devices. *Nat. Mater.* **9**, 205–213 (2010).
79. Hägglund, C. & Apell, S. P. Plasmonic Near-Field Absorbers for Ultrathin Solar Cells. *J. Phys. Chem. Lett.* **3**, 1275–1285 (2012).
80. Kühn, S., Håkanson, U., Rogobete, L. & Sandoghdar, V. Enhancement of Single-Molecule Fluorescence Using a Gold Nanoparticle as an Optical Nanoantenna. *Phys. Rev. Lett.* **97**, 017402 (2006).
81. Willets, K. A. & Van Duyne, R. P. Localized Surface Plasmon Resonance Spectroscopy and Sensing. *Annu. Rev. Phys. Chem.* **58**, 267–297 (2007).
82. Altug, H., Oh, S.-H., Maier, S. A. & Homola, J. Advances and applications of nanophotonic biosensors. *Nat. Nanotechnol.* **17**, 5–16 (2022).
83. Krenn, J. R. *et al.* Squeezing the Optical Near-Field Zone by Plasmon Coupling of Metallic Nanoparticles. *Phys. Rev. Lett.* **82**, 2590–2593 (1999).
84. Fischer, H. & Martin, O. J. F. Engineering the optical response of plasmonic nanoantennas. *Opt. Express* **16**, 9144–9154 (2008).
85. Kang, J. H., Kim, D. S. & Park, Q.-H. Local Capacitor Model for Plasmonic Electric Field Enhancement. *Phys. Rev. Lett.* **102**, 093906 (2009).
86. Mühlischlegel, P., Eisler, H.-J., Martin, O. J. F., Hecht, B. & Pohl, D. W. Resonant Optical Antennas. *Science* **308**, 1607–1609 (2005).

87. Park, Q.-H. Optical antennas and plasmonics. *Contemp. Phys.* **50**, 407–423 (2009).
88. Grigorenko, A. N., Roberts, N. W., Dickinson, M. R. & Zhang, Y. Nanometric optical tweezers based on nanostructured substrates. *Nat. Photonics* **2**, 365–370 (2008).
89. Quidant, R. Plasmonic tweezers—The strength of surface plasmons. *MRS Bull.* **37**, 739–744 (2012).
90. Baffou, G., Girard, C. & Quidant, R. Mapping Heat Origin in Plasmonic Structures. *Phys. Rev. Lett.* **104**, 136805 (2010).
91. Baffou, G. & Quidant, R. Thermo-Plasmonics: Using Metallic Nanostructures as Nano-Sources of Heat. *Laser Photonics Rev.* **7**, 171–187 (2013).
92. Hirsch, L. R. *et al.* Nanoshell-mediated near-infrared thermal therapy of tumors under magnetic resonance guidance. *Proc. Natl. Acad. Sci* **100**, 13549–13554 (2003).
93. Huang, X., El-Sayed, I. H., Qian, W. & El-Sayed, M. A. Cancer Cell Imaging and Photothermal Therapy in the Near-Infrared Region by Using Gold Nanorods. *J. Am. Chem. Soc.* **128**, 2115–2120 (2006).
94. Ali, M. R., Ibrahim, I. M., Ali, H. R., Selim, S. A. & El-Sayed, M. A. Treatment of natural mammary gland tumors in canines and felines using gold nanorods-assisted plasmonic photothermal therapy to induce tumor apoptosis. *Int. J. Nanomedicine* **11**, 4849–4863 (2016).
95. Adleman, J. R., Boyd, D. A., Goodwin, D. G. & Psaltis, D. Heterogenous Catalysis Mediated by Plasmon Heating. *Nano Lett.* **9**, 4417–4423 (2009).
96. Qiu, J. & Wei, W. D. Surface Plasmon-Mediated Photothermal Chemistry. *J. Phys. Chem. C* **118**, 20735–20749 (2014).
97. Robert, H. M. L. *et al.* Light-Assisted Solvothermal Chemistry Using Plasmonic Nanoparticles. *ACS Omega* **1**, 2–8 (2016).
98. Wu, C. *et al.* Metamaterial-based integrated plasmonic absorber/emitter for solar thermo-photovoltaic systems. *Journal of Optics* **14**, 024005 (2012).
99. Tagliabue, G., Eghlidi, H. & Poulidakos, D. Facile multifunctional plasmonic sunlight harvesting with tapered triangle nanopatterning of thin films. *Nanoscale* **5**, 9957–9962 (2013).
100. Taylor, R. W. & Sandoghdar, V. Interferometric Scattering Microscopy: Seeing Single Nanoparticles and Molecules via Rayleigh Scattering. *Nano Lett.* **19**, 4827–4835 (2019).
101. Martin, O. *Building Tomorrow's nanofactory* 2022.
102. Murray, W. A. & Barnes, W. L. Plasmonic Materials. *Adv. Mater.* **19**, 3771–3782 (2007).
103. Graedel, T. E. Corrosion Mechanisms for Silver Exposed to the Atmosphere. *Journal of The Electrochemical Society* **139**, 1963 (1992).
104. Wang, X., Santschi, C. & Martin, O. J. F. Strong Improvement of Long-Term Chemical and Thermal Stability of Plasmonic Silver Nanoantennas and Films. *Small* **13**, 1700044 (2017).

BIBLIOGRAPHY

105. Lowry, G. V. *et al.* Guidance to Improve the Scientific Value of Zeta-Potential Measurements in NanoEHS. *Environ. Sci.: Nano* **3**, 953–965 (5 2016).
106. Kern, A. M. & Martin, O. J. F. Surface integral formulation for 3D simulations of plasmonic and high permittivity nanostructures. *J. Opt. Soc. Am. A* **26**, 732–740 (2009).
107. Raziman, T. V., Somerville, W. R. C., Martin, O. J. F. & Ru, E. C. L. Accuracy of surface integral equation matrix elements in plasmonic calculations. *J. Opt. Soc. Am. B* **32**, 485–492 (2015).
108. Harrington, R. *Field Computation by Moment Methods* (Macmillan, 1968).
109. Ji, A., Raziman, T. V., Butet, J., Sharma, R. P. & Martin, O. J. F. Optical forces and torques on realistic plasmonic nanostructures: a surface integral approach. *Opt. Lett.* **39**, 4699–4702 (2014).
110. Raziman, T. V. & Martin, O. J. F. Does the real part contain all the physical information? *Journal of Optics* **18**, 095002 (2016).
111. Rakić, A. D., Djurišić, A. B., Elazar, J. M. & Majewski, M. L. Optical Properties of Metallic Films for Vertical-Cavity Optoelectronic Devices. *Appl. Opt.* **37**, 5271–5283 (1998).
112. Kim, J. & Martin, O. J. F. Surfactants Control Optical Trapping near a Glass Wall. *J. Phys. Chem. C* **126**, 378–386 (2022).
113. Tadros, T. in *Colloid Stability* 1–22 (John Wiley & Sons, Ltd, 2010).
114. Shrestha, S., Wang, B. & Dutta, P. Nanoparticle Processing: Understanding and Controlling Aggregation. *Adv. Colloid Interface Sci.* **279**, 102162 (2020).
115. Lin, L. *et al.* Opto-Thermoelectric Nanotweezers. *Nat. Photonics* **12**, 195–201 (2018).
116. Liu, Y. *et al.* Nanoradiator-Mediated Deterministic Opto-Thermoelectric Manipulation. *ACS Nano* **12**, 10383–10392 (2018).
117. Jiang, Q., Rogez, B., Claude, J.-B., Baffou, G. & Wenger, J. Quantifying the Role of the Surfactant and the Thermophoretic Force in Plasmonic Nano-optical Trapping. *Nano Lett.* **20**, 8811–8817 (2020).
118. Crocker, J. C. & Grier, D. G. Methods of Digital Video Microscopy for Colloidal Studies. *J. Colloid Interface Sci.* **179**, 298–310 (1996).
119. Gibson, G. M., Leach, J., Keen, S., Wright, A. J. & Padgett, M. J. Measuring the Accuracy of Particle Position and Force in Optical Tweezers Using High-Speed Video Microscopy. *Opt. Express* **16**, 14561–14570 (2008).
120. Otto, O. *et al.* High-Speed Video-Based Tracking of Optically Trapped Colloids. *J. Opt.* **13**, 044011 (2011).
121. Jain, P. K., Lee, K. S., El-Sayed, I. H. & El-Sayed, M. A. Calculated Absorption and Scattering Properties of Gold Nanoparticles of Different Size, Shape, and Composition: Applications in Biological Imaging and Biomedicine. *J. Phys. Chem. B* **110**, 7238–7248 (2006).

122. Baffou, G., Cichos, F. & Quidant, R. Applications and Challenges of Thermoplasmonics. *Nat. Mater.* **19**, 946–958 (2020).
123. Allan, D. B., Caswell, T., Keim, N. C., van der Wel, C. M. & Verweij, R. W. *soft-matter/trackpy: Trackpy v0.5.0* version v0.5.0. 2021.
124. Kim, J. & Martin, J. F. O. *Dataset for the Manuscript: Surfactants Control Optical Trapping Near a Glass Wall* <https://doi.org/10.5281/zenodo.5557074>. 2021.
125. Nørrelykke, S. F. & Flyvbjerg, H. Harmonic Oscillator in Heat Bath: Exact Simulation of Time-Lapse-Recorded Data and Exact Analytical Benchmark Statistics. *Phys. Rev. E* **83**, 041103 (2011).
126. Bendix, P. M., Reihani, S. N. S. & Oddershede, L. B. Direct Measurements of Heating by Electromagnetically Trapped Gold Nanoparticles on Supported Lipid Bilayers. *ACS Nano* **4**, 2256–2262 (2010).
127. Kyrsting, A., Bendix, P. M., Stamou, D. G. & Oddershede, L. B. Heat Profiling of Three-Dimensionally Optically Trapped Gold Nanoparticles using Vesicle Cargo Release. *Nano Lett.* **11**, 888–892 (2011).
128. Lemons, D. S. & Gythiel, A. Paul Langevin's 1908 paper "On the Theory of Brownian Motion" ["Sur la théorie du mouvement brownien," C. R. Acad. Sci. (Paris) 146, 530–533 (1908)]. *Am. J. Phys.* **65**, 1079–1081 (1997).
129. Purcell, E. M. Life at low Reynolds number. *Am. J. Phys.* **45**, 3–11 (1977).
130. Nikoobakht, B. & El-Sayed, M. A. Evidence for Bilayer Assembly of Cationic Surfactants on the Surface of Gold Nanorods. *Langmuir* **17**, 6368–6374 (2001).
131. Liu, J.-F., Min, G. & Ducker, W. A. AFM Study of Adsorption of Cationic Surfactants and Cationic Polyelectrolytes at the Silica-Water Interface. *Langmuir* **17**, 4895–4903 (2001).
132. Atkin, R., Craig, V., Wanless, E. & Biggs, S. Mechanism of cationic surfactant adsorption at the solid–aqueous interface. *Adv. Colloid Interface Sci.* **103**, 219–304 (2003).
133. Gao, Y., Du, J. & Gu, T. Hemimicelle formation of cationic surfactants at the silica gel–water interface. *J. Chem. Soc., Faraday Trans. 1* **83**, 2671–2679 (8 1987).
134. Tyrode, E., Rutland, M. W. & Bain, C. D. Adsorption of CTAB on Hydrophilic Silica Studied by Linear and Nonlinear Optical Spectroscopy. *J. Am. Chem. Soc.* **130**, 17434–17445 (2008).
135. Li, R. *et al.* Study on the Assembly Structure Variation of Cetyltrimethylammonium Bromide on the Surface of Gold Nanoparticles. *ACS Omega* **5**, 4943–4952 (2020).
136. Reiss-Husson, F. & Luzzati, V. The Structure of the Micellar Solutions of Some Amphiphilic Compounds in Pure Water as Determined by Absolute Small-Angle X-Ray Scattering Techniques. *J. Phys. Chem.* **68**, 3504–3511 (1964).
137. Williams, R. J., Phillips, J. N. & Mysels, K. J. The Critical Micelle Concentration of Sodium Lauryl Sulphate at 25 °C. *Trans. Faraday Soc.* **51**, 728–737 (1955).

BIBLIOGRAPHY

138. Pérez-Rodríguez, M. *et al.* A Comparative Study of the Determination of the Critical Micelle Concentration by Conductivity and Dielectric Constant Measurements. *Langmuir* **14**, 4422–4426 (1998).
139. Tofani, L. *et al.* Spectroscopic and Interfacial Properties of Myoglobin/Surfactant Complexes. *Biophys. J.* **87**, 1186–1195 (2004).
140. Bijsterbosch, B. Characterization of Silica Surfaces by Adsorption From Solution. Investigations Into the Mechanism of Adsorption of Cationic Surfactants. *J. Colloid Interface Sci.* **47**, 186–198 (1974).
141. Schäffer, E., Nørrelykke, S. F. & Howard, J. Surface Forces and Drag Coefficients of Microspheres near a Plane Surface Measured with Optical Tweezers. *Langmuir* **23**, 3654–3665 (2007).
142. Happel, J. & Brenner, H. *Low Reynolds number hydrodynamics: with special applications to particulate media* (Springer, Dordrecht, 2012).
143. Seol, Y., Carpenter, A. E. & Perkins, T. T. Gold Nanoparticles: Enhanced Optical Trapping and Sensitivity Coupled With Significant Heating. *Opt. Lett.* **31**, 2429–2431 (2006).
144. Atkins, P. & De Paula, J. *Atkins' Physical Chemistry* 628–629 (Oxford University Press, Oxford, UK, 2014).
145. Krishnan, M., Mojarad, N., Kukura, P. & Sandoghdar, V. Geometry-Induced Electrostatic Trapping of Nanometric Objects in a Fluid. *Nature* **467**, 692–695 (2010).
146. Kim, J. & Martin, O. J. F. Probing surfactant bilayer interactions by tracking optically trapped single nanoparticles. *Adv. Mater. Interfaces* (2022).
147. Qian, H., Sheetz, M. & Elson, E. Single particle tracking. Analysis of diffusion and flow in two-dimensional systems. *Biophys. J.* **60**, 910–921 (1991).
148. Araque, J. C., Yadav, S. K., Shadeck, M., Maroncelli, M. & Margulis, C. J. How Is Diffusion of Neutral and Charged Tracers Related to the Structure and Dynamics of a Room-Temperature Ionic Liquid? Large Deviations from Stokes–Einstein Behavior Explained. *J. Phys. Chem. B* **119**, 7015–7029 (2015).
149. Kirstein, J. *et al.* Exploration of nanostructured channel systems with single-molecule probes. *Nat. Mater.* **6**, 303–310 (2007).
150. Comstock, M. J., Ha, T. & Chemla, Y. R. Ultrahigh-resolution optical trap with single-fluorophore sensitivity. *Nat. Methods* **8**, 335–340 (2011).
151. Atkins, P. & De Paula, J. *Atkins' Physical Chemistry* (Oxford University Press, Oxford, UK, 2014).
152. Yuan, Y. *et al.* Optical trapping-assisted SERS platform for chemical and biosensing applications: Design perspectives. *Coord. Chem. Rev.* **339**, 138–152 (2017).
153. Oyamada, N., Minamimoto, H. & Murakoshi, K. Room-Temperature Molecular Manipulation via Plasmonic Trapping at Electrified Interfaces. *J. Am. Chem. Soc.* (2022).

154. Tsuboi, Y. *et al.* Optical Trapping of Nanocrystals at Oil/Water Interfaces: Implications for Photocatalysis. *ACS Appl. Nano Mater.* **4**, 11743–11752 (2021).
155. Kim, J. & Martin, O. J. F. *Dataset for the manuscript: Probing surfactant bilayer interactions by tracking optically trapped single nanoparticles* <https://doi.org/10.5281/zenodo.6015007>. 2022.
156. Alam, A. U., Howlader, M. M. R. & Deen, M. J. The effects of oxygen plasma and humidity on surface roughness, water contact angle and hardness of silicon, silicon dioxide and glass. *J. Micromech. Microeng.* **24**, 035010 (2014).
157. Goloub, T. P., Koopal, L. K., Bijsterbosch, B. H. & Sidorova, M. P. Adsorption of Cationic Surfactants on Silica. Surface Charge Effects. *Langmuir* **12**, 3188–3194 (1996).
158. Goloub, T. P. & Koopal, L. K. Adsorption of Cationic Surfactants on Silica. Comparison of Experiment and Theory. *Langmuir* **13**, 673–681 (1997).
159. Lamont, R. E. & Ducker, W. A. Surface-Induced Transformations for Surfactant Aggregates. *J. Am. Chem. Soc.* **120**, 7602–7607 (1998).
160. Chorro, M., Chorro, C., Dolladille, O., Partyka, S. & Zana, R. Adsorption Mechanism of Conventional and Dimeric Cationic Surfactants on Silica Surface: Effect of the State of the Surface. *J. Colloid Interface Sci.* **210**, 134–143 (1999).
161. Grant, L. M., Ederth, T. & Tiberg, F. Influence of Surface Hydrophobicity on the Layer Properties of Adsorbed Nonionic Surfactants. *Langmuir* **16**, 2285–2291 (2000).
162. Behrens, S. H. & Grier, D. G. The Charge of Glass and Silica Surfaces. *J. Chem. Phys.* **115**, 6716–6721 (2001).
163. Ducker, W. A. & Wanless, E. J. Adsorption of Hexadecyltrimethylammonium Bromide to Mica: Nanometer-Scale Study of Binding-Site Competition Effects. *Langmuir* **15**, 160–168 (1999).
164. Helm, C. A., Israelachvili, J. N. & McGuiggan, P. M. Role of hydrophobic forces in bilayer adhesion and fusion. *Biochem.* **31**, 1794–1805 (1992).
165. Petrache, H. I. *et al.* Interbilayer interactions from high-resolution x-ray scattering. *Phys. Rev. E* **57**, 7014–7024 (1998).
166. Svoboda, K. & Block, S. M. Biological Applications of Optical Forces. *Annu. Rev. Biophys. Biomol. Struct.* **23**, 247–285 (1994).
167. Neusius, T., Sokolov, I. M. & Smith, J. C. Subdiffusion in time-averaged, confined random walks. *Phys. Rev. E* **80**, 011109 (2009).
168. Jeon, J.-H. & Metzler, R. Fractional Brownian motion and motion governed by the fractional Langevin equation in confined geometries. *Phys. Rev. E* **81**, 021103 (2010).
169. Tolić-Nørrelykke, I. M., Munteanu, E.-L., Thon, G., Oddershede, L. & Berg-Sørensen, K. Anomalous Diffusion in Living Yeast Cells. *Phys. Rev. Lett.* **93**, 078102 (2004).

BIBLIOGRAPHY

170. Wachsmuth, M., Waldeck, W. & Langowski, J. Anomalous diffusion of fluorescent probes inside living cell nuclei investigated by spatially-resolved fluorescence correlation spectroscopy. *J. Mol. Biol.* **298**, 677–689 (2000).
171. Jeon, J.-H., Leijnse, N., Oddershede, L. B. & Metzler, R. Anomalous diffusion and power-law relaxation of the time averaged mean squared displacement in worm-like micellar solutions. *New J. Phys.* **15**, 045011 (2013).
172. Morimoto, K. *et al.* Megapixel time-gated SPAD image sensor for 2D and 3D imaging applications. *Optica* **7**, 346–354 (2020).
173. Dienerowitz, M., Mazilu, M. & Dholakia, K. Optical Manipulation of Nanoparticles: A Review. *J. Nanophotonics* **2**, 1–32, 32 (2008).
174. Zemánek, P., Jonáš, A., Šrámek, L. & Liška, M. Optical trapping of nanoparticles and microparticles by a Gaussian standing wave. *Opt. Lett.* **24**, 1448–1450 (1999).
175. Novotny, L., Bian, R. X. & Xie, X. S. Theory of Nanometric Optical Tweezers. *Phys. Rev. Lett.* **79**, 645–648 (1997).
176. Righini, M., Zelenina, A. S., Girard, C. & Quidant, R. Parallel and selective trapping in a patterned plasmonic landscape. *Nat. Phys.* **3**, 477–480 (2007).
177. Righini, M., Volpe, G., Girard, C., Petrov, D. & Quidant, R. Surface Plasmon Optical Tweezers: Tunable Optical Manipulation in the Femtonewton Range. *Phys. Rev. Lett.* **100**, 186804 (2008).
178. Righini, M. *et al.* Nano-optical Trapping of Rayleigh Particles and Escherichia coli Bacteria with Resonant Optical Antennas. *Nano Lett.* **9**, 3387–3391 (2009).
179. Juan, M. L., Gordon, R., Pang, Y., Eftekhari, F. & Quidant, R. Self-induced back-action optical trapping of dielectric nanoparticles. *Nat. Phys.* **5**, 915–919 (2009).
180. Juan, M. L., Righini, M. & Quidant, R. Plasmon nano-optical tweezers. *Nat. Photonics* **5**, 349 (2011).
181. Padhy, P., Zaman, M. A. & Hesselink, L. In-plane near-field optical barrier on a chip. *Opt. Lett.* **44**, 2061–2064 (2019).
182. Giannini, V., Fernández-Domínguez, A. I., Heck, S. C. & Maier, S. A. Plasmonic Nanoantennas: Fundamentals and Their Use in Controlling the Radiative Properties of Nanoemitters. *Chem. Rev.* **111**, 3888–3912 (2011).
183. Grober, R. D., Schoelkopf, R. J. & Prober, D. E. Optical antenna: Towards a unity efficiency near-field optical probe. *Appl. Phys. Lett.* **70**, 1354–1356 (1997).
184. Zhang, W., Huang, L., Santschi, C. & Martin, O. J. F. Trapping and Sensing 10 nm Metal Nanoparticles Using Plasmonic Dipole Antennas. *Nano Lett.* **10**, 1006–1011 (2010).
185. Crozier, K. B., Sundaramurthy, A., Kino, G. S. & Quate, C. F. Optical antennas: Resonators for local field enhancement. *J. Appl. Phys.* **94**, 4632–4642 (2003).
186. Ashkin, A. Applications of Laser Radiation Pressure. *Science* **210**, 1081–1088 (1980).

187. Ke, P. C. & Gu, M. Characterization of trapping force on metallic Mie particles. *Appl. Opt.* **36**, 160–167 (1999).
188. Pelton, M. & Bryant, G. W. *Introduction to metal-nanoparticle plasmonics* (John Wiley & Sons, 2013).
189. Prodan, E., Radloff, C., Halas, N. J. & Nordlander, P. A hybridization model for the plasmon response of complex nanostructures. *Science* **302**, 419–422 (2003).
190. Pelton, M. *et al.* Optical trapping and alignment of single gold nanorods by using plasmon resonances. *Opt. Lett.* **31**, 2075–2077 (2006).
191. Svoboda, K. & Block, S. Optical trapping of metallic Rayleigh particles. *Opt. Lett.* **19**, 930–932 (1994).
192. Hansen, P. M., Bhatia, V. K., Harrit, N. & Oddershede, L. Expanding the Optical Trapping Range of Gold Nanoparticles. *Nano Lett.* **5**, 1937–1942 (2005).
193. Bosanac, L., Aabo, T., Bendix, P. M. & Oddershede, L. B. Efficient Optical Trapping and Visualization of Silver Nanoparticles. *Nano Lett.* **8**, 1486–1491 (2008).
194. Hajizadeh, F. & S.Reihani, S. N. Optimized optical trapping of gold nanoparticles. *Opt. Express* **18**, 551–559 (2010).
195. Johnson, P. B. & Christy, R. W. Optical Constants of the Noble Metals. *Phys. Rev. B* **6**, 4370–4379 (1972).
196. Gay-Balmaz, P. & Martin, O. J. F. Electromagnetic scattering of high-permittivity particles on a substrate. *Appl. Opt.* **40**, 4562–9 (2001).
197. Vernon, K. C. *et al.* Influence of Particle–Substrate Interaction on Localized Plasmon Resonances. *Nano Lett.* **10**, 2080–2086 (2010).
198. Kim, J. & Martin, O. J. *Data set for the manuscript: The different coupling regimes for a plasmonic particle in a plasmonic trap* <https://doi.org/10.5281/zenodo.3525240>. Version 1.0.0. 2019.
199. Neumeier, L., Quidant, R. & Chang, D. E. Self-induced back-action optical trapping in nanophotonic systems. *New J. Phys.* **17**, 123008 (2015).
200. Huang, L. & Martin, O. J. F. Reversal of the optical force in a plasmonic trap. *Opt. Lett.* **33**, 3001–3003 (2008).
201. Burns, M. M., Fournier, J.-M. & Golovchenko, J. A. Optical binding. *Phys. Rev. Lett.* **63**, 1233 (1989).
202. Dapasse, F. & Vigoureux, J. M. Optical binding force between two Rayleigh particles. *J. Phys. D: Appl. Phys.* **27**, 914–919 (1994).
203. Ashkin, A., Dziedzic, J. M. & Yamane, T. Optical trapping and manipulation of single cells using infrared laser beams. *Nature* **330**, 769–771 (1987).
204. Philip H. Jones Onofrio M. Maragò, G. V. *Optical tweezers : principles and applications* eng (Cambridge University Press, Cambridge, 2015).

BIBLIOGRAPHY

205. Le Ru, E. & Etchegoin, P. *Principles of Surface-Enhanced Raman Spectroscopy: and related plasmonic effects* (Elsevier, 2008).
206. Wang, X., Huang, S.-C., Hu, S., Yan, S. & Ren, B. Fundamental understanding and applications of plasmon-enhanced Raman spectroscopy. *Nature Reviews Physics* **2**, 253–271 (2020).
207. Koya, A. N. *et al.* Novel Plasmonic Nanocavities for Optical Trapping-Assisted Biosensing Applications. *Adv. Opt. Mater.* **8**, 1901481 (2020).
208. Liu, D. & Xue, C. Plasmonic Coupling Architectures for Enhanced Photocatalysis. *Adv. Mater.* **33**, 2005738 (2021).
209. Kumar, A., Choudhary, P., Kumar, A., Camargo, P. H. C. & Krishnan, V. Recent Advances in Plasmonic Photocatalysis Based on TiO₂ and Noble Metal Nanoparticles for Energy Conversion, Environmental Remediation, and Organic Synthesis. *Small* **18**, 2101638 (2022).
210. Jain, P. K. & El-Sayed, M. A. Plasmonic coupling in noble metal nanostructures. *Chemical Physics Letters* **487**, 153–164 (2010).
211. Fan, J. A. *et al.* Self-Assembled Plasmonic Nanoparticle Clusters. *Science* **328**, 1135–1138 (2010).
212. Cao, W. *et al.* Plasmon-induced transparency in metamaterials: Active near field coupling between bright superconducting and dark metallic mode resonators. *Appl. Phys. Lett.* **103**, 101106 (2013).
213. Hentschel, M. *et al.* Transition from Isolated to Collective Modes in Plasmonic Oligomers. *Nano Lett.* **10**, 2721–2726 (2010).
214. Hentschel, M., Dregely, D., Vogelgesang, R., Giessen, H. & Liu, N. Plasmonic Oligomers: The Role of Individual Particles in Collective Behavior. *ACS Nano* **5**, 2042–2050 (2011).
215. Greybush, N. J. *et al.* Plasmon Resonances in Self-Assembled Two-Dimensional Au Nanocrystal Metamolecules. *ACS Nano* **11**, 2917–2927 (2017).
216. Thomas, J. C. The determination of log normal particle size distributions by dynamic light scattering. *Journal of Colloid and Interface Science* **117**, 187–192 (1987).
217. Flauraud, V. *et al.* Mode Coupling in Plasmonic Heterodimers Probed with Electron Energy Loss Spectroscopy. *ACS Nano* **11**, 3485–3495 (2017).
218. Schoenlein, R. W., Lin, W. Z., Fujimoto, J. G. & Eesley, G. L. Femtosecond studies of nonequilibrium electronic processes in metals. *Phys. Rev. Lett.* **58**, 1680–1683 (1987).
219. Fano, U. Effects of Configuration Interaction on Intensities and Phase Shifts. *Phys. Rev.* **124**, 1866–1878 (1961).
220. Joe, Y. S., Satanin, A. M. & Kim, C. S. Classical analogy of Fano resonances. *Physica Scripta* **74**, 259 (2006).
221. Gallinet, B. & Martin, O. J. F. Ab initio theory of Fano resonances in plasmonic nanostructures and metamaterials. *Phys. Rev. B* **83**, 235427 (2011).

-
222. Byrd, R. H., Hribar, M. E. & Nocedal, J. An interior point algorithm for large-scale nonlinear programming. *SIAM J. Optim.* **9**, 877–900 (1999).
223. Bishop, C. M. & Nasrabadi, N. M. *Pattern recognition and machine learning* **4** (Springer, 2006).
224. Limonov, M. F. Fano resonance for applications. *Adv. Opt. Photon.* **13**, 703–771 (2021).
225. Raziman, T. V. & Martin, O. J. F. Polarisation charges and scattering behaviour of realistically rounded plasmonic nanostructures. *Opt. Express* **21**, 21500–21507 (2013).
226. Wu, H.-M., Lin, Y.-H., Yen, T.-C. & Hsieh, C.-L. Nanoscopic substructures of raft-mimetic liquid-ordered membrane domains revealed by high-speed single-particle tracking. *Sci. Rep.* **6**, 20542 (2016).
227. Pralle, A., Prummer, M., Florin, E.-L., Stelzer, E. & Hörber, J. Three-Dimensional High-Resolution Particle Tracking for Optical Tweezers by Forward Scattered Light. *Microsc. Res. Tech.* **44**, 378–386 (1999).
228. Keen, S., Leach, J., Gibson, G. & Padgett, M. J. Comparison of a high-speed camera and a quadrant detector for measuring displacements in optical tweezers. *J. Opt. A-Pure Appl. Opt.* **9**, S264 (2007).
229. Abasahl, B., Santschi, C., Raziman, T. V. & Martin, O. J. F. Fabrication of plasmonic structures with well-controlled nanometric features: a comparison between lift-off and ion beam etching. *Nanotechnology* **32**, 475202 (2021).
230. Killian, J. L., Ye, F. & Wang, M. D. Optical Tweezers: A Force to Be Reckoned With. *Cell* **175**, 1445–1448 (2018).
231. Lessard, G. A., Goodwin, P. M. & Werner, J. H. Three-Dimensional Tracking of Individual Quantum Dots. *Appl. Phys. Lett.* **91**, 224106 (2007).
232. Katayama, Y. *et al.* Real-Time Nanomicroscopy Via Three-Dimensional Single-Particle Tracking. *ChemPhysChem* **10**, 2458 (2009).
233. Lew, M. D., Thompson, M. A., Badieirostami, M. & Moerner, W. E. In Vivo Three-Dimensional Superresolution Fluorescence Tracking Using a Double-Helix Point Spread Function. *Proc. SPIE* **7571**, 75710Z (2010).
234. Spille, J. H., Kaminski, T., Königshoven, H. P. & Kubitscheck, U. Dynamic Three-Dimensional Tracking of Single Fluorescent Nanoparticles Deep inside Living Tissue. *Opt. Express* **20**, 19697 (2012).
235. Dupont, A. *et al.* Three-Dimensional Single-Particle Tracking in Live Cells: News from the Third Dimension. *New J. Phys.* **15**, 075008 (2013).
236. Germann, J. A. & Davis, L. M. Three-Dimensional Tracking of a Single Fluorescent Nanoparticle Using Four-Focus Excitation in a Confocal Microscope. *Opt. Express* **22**, 5641 (2014).
237. Perillo, E. P. *et al.* Deep and High-Resolution Three-Dimensional Tracking of Single Particles Using Nonlinear and Multiplexed Illumination. *Nat. Commun.* **6**, 7874 (2015).

BIBLIOGRAPHY

238. Yu, B. *et al.* Nanoscale Three-Dimensional Single Particle Tracking by Light-Sheet-Based Double-Helix Point Spread Function Microscopy. *Appl. Opt.* **55**, 449 (2016).
239. Wang, Y. *et al.* Plasmon-directed polymerization: Regulating polymer growth with light. *Nano Res.* **11**, 6384–6390 (2018).
240. Kameche, F. *et al.* Probing Plasmon-Induced Chemical Mechanisms by Free-Radical Nanophotopolymerization. *J. Phys. Chem. C* **125**, 8719–8731 (2021).
241. Baldacchini, T. *Three-dimensional microfabrication using two-photon polymerization: fundamentals, technology, and applications* (William Andrew, 2015).
242. Ueno, K. *et al.* Nanoparticle Plasmon-Assisted Two-Photon Polymerization Induced by Incoherent Excitation Source. *J. Am. Chem. Soc.* **130**, 6928–6929 (2008).
243. Ding, T., Mertens, J., Lombardi, A., Scherman, O. A. & Baumberg, J. J. Light-Directed Tuning of Plasmon Resonances via Plasmon-Induced Polymerization Using Hot Electrons. *ACS Photonics* **4**, 1453–1458 (2017).
244. Rusak, E. *et al.* Hybrid nanoantennas for directional emission enhancement. *Appl. Phys. Lett.* **105**, 221109 (2014).
245. Lepeshov, S. I., Krasnok, A. E., Belov, P. A. & Miroshnichenko, A. E. Hybrid nanophotonics. *Physics-Uspekhi* **61**, 1035 (2019).
246. Ray, D. *et al.* Hybrid Metal-Dielectric Metasurfaces for Refractive Index Sensing. *Nano Lett.* **20**, 8752–8759 (2020).
247. Violi, I. L., Gargiulo, J., von Bilderling, C., Cortés, E. & Stefani, F. D. Light-Induced Polarization-Directed Growth of Optically Printed Gold Nanoparticles. *Nano Lett.* **16**, 6529–6533 (2016).
248. Chapin, S. C., Germain, V. & Dufresne, E. R. Automated trapping, assembly, and sorting with holographic optical tweezers. *Opt. Express* **14**, 13095–13100 (2006).
249. Patel, G. M., Patel, G. C., Patel, R. B., Patel, J. K. & Patel, M. Nanorobot: A versatile tool in nanomedicine. *J. Drug Target.* **14**, 63–67 (2006).
250. Whitesides, G. M. The Once and Future Nanomachine. *Sci. Am.* **285**, 78–83 (2001).
251. Derjaguin, B. A Theory of Interaction of Particles in Presence of Electric Double Layers and the Stability of Lyophobic Colloids and Disperse Systems. *Prog. Surf. Sci.* **43**, 1–14 (1993).
252. Derjaguin, B. & Landau, L. Theory of the Stability of Strongly Charged Lyophobic Sols and of the Adhesion of Strongly Charged Particles in Solutions of Electrolytes. *Prog. Surf. Sci.* **43**, 30–59 (1993).
253. Verwey, E., Overbeek, J. & van Nes, K. *Theory of the Stability of Lyophobic Colloids: The Interaction of Sol Particles Having an Electric Double Layer* (Elsevier Publishing Company, 1948).
254. Biggs, S. & Mulvaney, P. Measurement of the Forces Between Gold Surfaces in Water by Atomic Force Microscopy. *J. Chem. Phys.* **100**, 8501–8505 (1994).

- 255. Giesbers, M., Kleijn, J. & Cohen Stuart, M. A. The Electrical Double Layer on Gold Probed by Electrokinetic and Surface Force Measurements. *J. Colloid Interface Sci.* **248**, 88–95 (2002).
- 256. Russel, W. B., Russel, W., Saville, D. A. & Schowalter, W. R. *Colloidal Dispersions* (Cambridge University Press, Cambridge, UK, 1989).
- 257. Lyklema, J. *Fundamentals of Interface and Colloid Science. Volume I: Fundamentals.* chap. 4.6 and 4.7 (Academic Press, London, UK, 1991).

Jeonghyeon (Jenna) Kim

Address

Nanophotonics and Metrology Laboratory
ELG 236, Station 11, EPFL
Lausanne 1015, Switzerland

Phone

+41 78 252 6784

E-mail

jeonghyeon.kim@epfl.ch
cassette.kim@gmail.com

Education

2017 – 2023 **École polytechnique fédérale de Lausanne, Ph.D. in science, Switzerland**

Thesis title: Optical manipulation of plasmonic nanoparticles:
Applications in surface chemistry and nano-optics

Advisor: Prof. Olivier J. F. Martin

2012 – 2015 **Yonsei University, M.S. in Engineering, Seoul, Korea**

Thesis in plasmonics and its application in optoelectronics.

Advisor: Prof. Jong-Souk Yeo

2008 – 2012 **Yonsei University, B.S. in Engineering, Seoul, Korea**

Major in Electrical & Electronic Engineering

Research interests

Nanophotonics, optical manipulation, statistical physics, interface science.

Selected peer-reviewed publications

- [J1] **Jeonghyeon Kim** and Olivier J. F. Martin, "Probing Surfactant Bilayer Interactions by Tracking Optically Trapped Single Nanoparticles", *Adv. Mater. Interfaces*, 2022, 2201793.
- [J2] **Jeonghyeon Kim** and Olivier J. F. Martin, "Surfactants Control Optical Trapping near a Glass Wall", *J. Phys. Chem. C* 2022, 126, 1, 378–386.
- [J3] **Jeonghyeon Kim** and Olivier J. F. Martin, "Studying the different coupling regimes for a plasmonic particle in a plasmonic trap," *Opt. Express* 2019, 27, 38670–38682.
- [J4] **Jeonghyeon Kim** and Jong-Souk Yeo, "Enhanced Detection of Broadband Incoherent Light with Nanoridge Plasmonics", *Nano Lett.* 2015, 15, 4, 2291–2297.

Honors and awards

- 2015 **Best Research Thesis Award, Yonsei University**
Ranked 3rd of all dissertations from Engineering and Science Departments.
- 2012 – 2014 **Korean Government Graduate Fellowship, Republic of Korea**
Received full support from Korean government, including tuition, stipend, housing, and research grant.
- 2009 – 2012 **National Science and Engineering Undergraduate Scholarship, Republic of Korea**
Received full scholarship from the Korean government by the excellence in academic work.

Teaching experience

| | |
|-----------|--|
| 2017-2021 | Teaching assistant for Optical Engineering (2017 – 2020 Fall) Teaching assistant for Mise en oeuvre des matériaux II (2019 – 2021 Spring) |
| 2016 | Teaching volunteer for underprivileged students in middle school |
| 2013 | Teaching assistant for Applied Physics and Technology Management Mentoring high school students |

Skills and qualifications

| | |
|------------------|--|
| Nanofabrication | Electron-beam lithography Focused ion beam (FIB) milling Microfluidics Other semiconductor fabrication processes (thin-film processes, photolithography, and surface treatments) |
| Characterization | Scanning electron microscope (SEM) Atomic force microscope (AFM) Dynamic light scattering (DLS) Optical spectroscopy Optical microscopy Semiconductor characterization system |
| Modeling | COMSOL multiphysics |
| Programming | Matlab, Python |
| Illustration | Blender |
| Language | English (Fluent), Korean (Native), French (Basic) |